Proof of principle measurements of a MEMS accelerometer design including anti-spring technology

with application in seismic noise measurement for advanced gravitational waves detectors

HBO Bachelor thesis

20-12-2012

Dave van Wees

10085459

The Hague University of applied sciences, Bachelor Applied Physics

Internship coordinator: dhr. C.A. Swarts

1st Internship coach: dhr. R.A. Mantel

2nd Internship coach: dhr. dr. L.H. Arntzen

Internship supervisor: dhr. E. Hennes

Approval internship supervisor: date: 19-12-2012

THE HAGUE UNIVERSITY OF APPLIED SCIENCES

NIKHEF National Institute for subatomic physics

Abstract

A gravitational wave detector sensitivity is limited by Newtonian noise at low frequencies. This can be predicted by measuring the seismic noise around the detector test masses, using an accelerometer grid. The accelerometer requires a high sensitivity in the 0,1 – 10 Hz bandwidth, which is achieved by a low resonance frequency device. A possible way of achieving a low frequency, low cost accelerometer is by using a MEMS accelerometer including anti-spring technology.

During this graduation, proof-of-principle measurements were done on a first set of MEMS accelerometers, designed at the mechanical department of Nikhef (National Institute for Subatomic Physics). The design is based on a mass-spring oscillator, in which the mass is suspended by four curved cantilever springs. By compressing the springs in one direction, the resonance frequency of the oscillator is lowered in the perpendicular direction. This is the anti-spring effect. The spring compression is applied by Electro-thermal actuators (ETA beams). Mass oscillation is enforced and sensed by actuator combs and sensing combs respectively. Analysis include modeling and measuring of the anti-springs, ETA beams and actuator and sensing combs behavior.

Measurements result in a resonance frequency of a typical MEMS accelerometer of $f_0 = 200 \pm 2$ Hz. Reduction to $f_0 = 96 \pm 2$ Hz is achieved by 10 μm compression. Further compression is limited by the ETA beam performance range. The resonance quality factor varies from $Q = 5$ at atmospheric pressure to $Q = 10^5$ below 10^{-3} mbar. Most measurements are in agreement with the modeling results.

Table of Contents

1 Introduction

1.1 Detecting gravitational waves

The theory of general relativity predicts the existence of so called gravitational waves. These waves are best described as fluctuations in space time, originating from heavy objects in the universe. Although never achieved, it is predicted that it is possible to detect these waves using a gravitational wave detector. This would open new doors for astronomy, creating the possibility to sense previously undetectable objects, sense deeper into the early universe and verify new fundamental gravitational waves theories.

The Virgo detector is one of such gravitational wave detectors, sited in Italy, near Pisa, Figure 1a. It is a Michelson laser interferometer, consisting of two, three kilometer long, orthogonal Fabry-Perot cavities, Figure 1b. Multiple reflections between the mirrors on both ends of the cavities extend the effective optical arm length up to 150 km. This optical extension amplifies the distance variation caused by a gravitational wave. Advanced Virgo (the next detector upgrade) is designed to measure length differences $\Delta L = L_1 - L_2$ in the range of 10 Hz – 10 kHz, with its maximum sensitivity at 200 Hz which corresponds to $\Delta L = 10^{-20}$ m. This sensitivity can only be achieved by isolating all optical components from seismic vibration from earth, thus lowering the seismic noise. At Virgo, mechanical oscillators of low natural frequency are used to passively attenuate all vibrations above their resonance frequency. This low natural frequency is achieved by using anti-spring technology, including Geometric anti-springs (GAS springs) or magnetic anti-springs, and pendulums, including inverted pendulums.

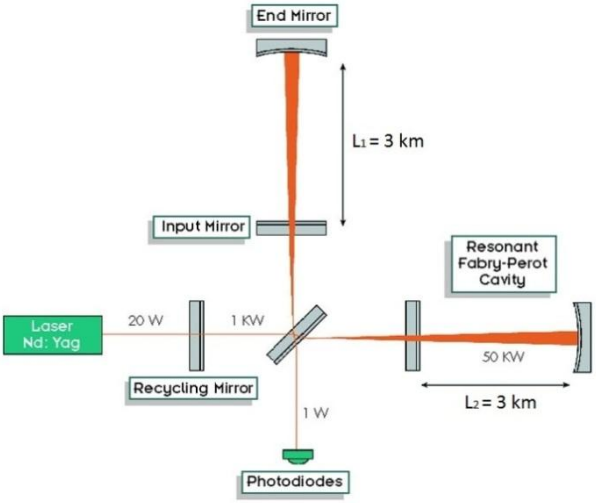

Figure 1: a) Aerial view of the Virgo interferometer, sited near Pisa, Italy [1]. b) schematic layout of the detector [2].

1.2 Seismic and Newtonian noise

Seismic noise is caused by the vibration of the earth. The vibration amplitude is in the order of microns, in a frequency range of 0,1 – 1 Hz, see Figure 2. This vibration amplitude in the order of 10^{-6}, mainly caused by sea swell waves ('ocean peak'), is a factor 10^{14} larger than the order of expected gravitational waves. At 10 Hz the seismic noise is still roughly a factor 10^{10} larger than the expected gravitational waves. The mechanical filters used for seismic noise attenuation have resonance frequencies below 1 Hz, which attenuates most of the seismic noise.

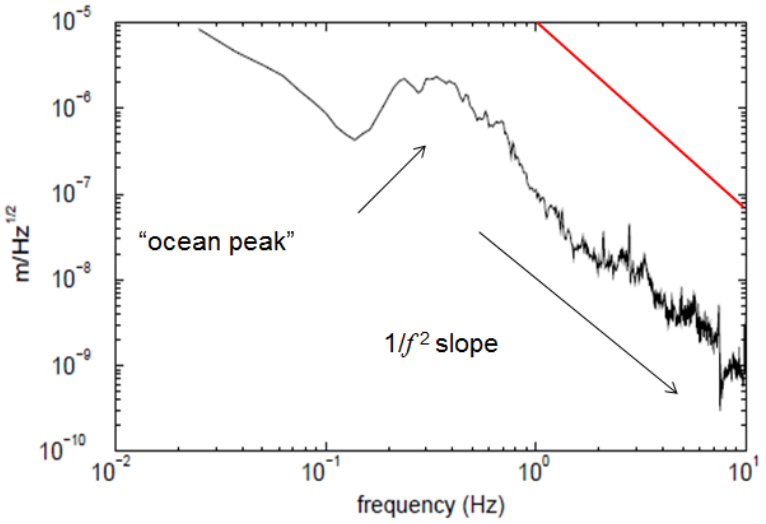

Figure 2: Seismic noise spectrum for the Virgo detector. The curve shows the root of the distribution of mean square noise displacements.

Seismic noise also creates a second type of vibration/noise called Newtonian noise. This noise type is created by the gravitational attraction between masses, also described as a time-dependent variation in the gravitational field. The vibration amplitude of the Newtonian noise is in the same order as the expected gravitational waves. When the Virgo sensitivity is sufficient to measure gravitational waves, it will also measure Newtonian noise. The only way to raise sensitivity beyond these disruptions is to know them by prediction from the seismic noise, and subtract them from the measured signal. As seen in the following equation, Newtonian noise can be predicted from the seismic noise by Newton's law of universal gravitation:

$$F_{Newtonian} = \frac{G m_{seismic} m_{mirror}}{|\vec{x}_{seismic} - \vec{x}_{mirror}|^2}, \quad (1)$$

where:
$F_{newtonian}$ = Newtonian noise [N]
G = gravitational constant [$\mathrm{Nm^2kg^{-2}}$]
$m_{seismic}$ = mass seismic particle [kg]
m_{mirror} = mass Virgo mirror [kg]
$\vec{x}_{seismic}$ = seismic coordinate [m]
$\vec{x}_{mirror}$ = mirror coordinate [m] .

When a seismic particle of mass $m_{seismic}$ displaces it will cause, for example a Virgo mirror (of mass m_{mirror}) displacement. The change of distance between the coordinates (change of $\vec{x}_{seismic} - \vec{x}_{mirror}$), results in a Newtonian force. This predicts the Newtonian force on the mirror, caused by the mass movement.

1.3 MEMS accelerometer project

For Virgo, and its successor the Einstein Telescope (ET), it is planned to measure the seismic noise of the surroundings by placing a grid of accelerometers around the interferometer. This measurement will enable the prediction of the Newtonian noise. For measuring the seismic noise the accelerometers must be sensitive at low frequencies of 0,1 – 10 Hz, thus having a low resonance frequency. Furthermore, because of the quantity of accelerometers needed, production costs should be low, without losing sensitivity at low frequency.

A possible solution is using a MEMS (Micro-Electro Mechanical System) accelerometer, which is a mechanical accelerometer on a chip/silicon wafer. MEMS technology is the name for all mechanical devices made on chip level, in the order of microns. To reach a low resonance frequency on chip dimensions, anti-spring technology is implemented on the accelerometer chip.

The MEMS project on Nikhef (National Institute for Subatomic Physics), sited in Amsterdam, is a R&D project of the gravitational waves group. The idea is to develop MEMS accelerometers suitable for detection of low frequent seismic noise in the surroundings of Virgo and ET optical mirrors. Currently the project is in proof of principle phase, and the goal is to test the new combination of MEMS with implemented anti-spring technology. The proof of principle measurements are carried out using the first set of MEMS chips produced at MESA+ (Institute for Nanotechnology), part of the University of Twente.

Four different MEMS designs are produced, including three anti-spring designs and one inverted pendulum design. The three anti-spring MEMS differ in ways of regulating and locking compression by using different structures, including guiding springs, bi-stable beams and anti-reverse structures.

The proof of principle measurements consists of functionality testing and mainly measurement of the accelerometer resonance frequency drop under anti-spring compression. Furthermore side structures are measured like Electro-thermal beams, for spring compression, and actuation and sensing capacitors, for mass displacement and sensing.

The actuation and sensing electronics and the used vacuum system are designed and built at the VU University, sited in Amsterdam.

2 Theory

The basic working principle of accelerometers is based on the inertia of matter. A proof mass is suspended to a frame by a spring or set of springs. Acceleration of the frame results in delayed acceleration of the proof mass due to its inertia. The relative movement between mass and frame is a direct measure for the acceleration of the frame, given the spring constant and the weight of the proof mass.

The designed MEMS accelerometer consists of a square mass suspended by four springs, one attached to each corner. Proof mass actuation and displacement sensing relative to the frame is performed by actuating and sensing combs respectively. Compression of the springs is done by electro-thermal actuators (ETA's) or manually, using micro-probes.

Modeling of the MEMS accelerometer consists of mass-spring oscillator behavior modeling, bending beam modeling of anti-springs and ETA's, and capacitance modeling of the combs.

2.1 Mass-spring oscillation

When a mass-spring system is brought in undamped harmonic motion, it will oscillate in its own characteristic frequency, dependent on its mass and spring stiffness:

$$\omega_0 = 2\pi f_0 = \sqrt{\frac{k}{m}}, \tag{2}$$

where:
$\omega_0 =$ natural angular frequency [rad/s]
$f_0 =$ natural frequency [s^{-1}]
$k =$ spring constant [N/m]
$m =$ mass [kg].

When the mass-spring system is driven by its natural frequency, it will resonate in this frequency, gaining in amplitude. Eq. (2) shows that lowering the natural frequency of an oscillator is possible by lowering the spring constant, or raising the mass. In case of a MEMS accelerometer, raising the mass is limited, because of the chip size, which is preferably as small as possible. This makes an as low as possible spring constant the main design feature of a MEMS accelerometer. This is possible by using anti-spring technology, explained in chapter 2.2.

2.1.1 Forced harmonic motion

The oscillation behavior of a MEMS accelerometer can be characterized by considering forced harmonic motion. Consider a proof mass *m* attached to a frame by a spring with spring constant k. The proof mass can be accelerated relative to the frame by applying a force *F* on the proof mass, or by a displacement x_0 of the frame, see Figure 3. The relative displacement is given by $y = x_1 - x_0$, which is the displacement to be measured. Here x_1 is the displacement of the proof mass.

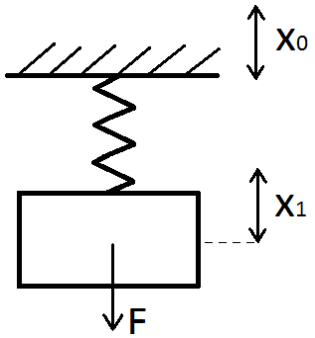

Figure 3: Sketch of a mass-spring system.

In case of harmonic excitation $x_0 = |x_0|e^{i(\omega t - i\varphi)} = \hat{x}_0 e^{i\omega t}$, the following solution follows for the complex amplitude ratio of x_1 and x_0:

$$\left|\frac{\hat{y}}{\hat{x}_0}\right| = \frac{\omega^2}{\omega_0^2}\frac{1}{\sqrt{\left(1-\frac{\omega^2}{\omega_0^2}\right)^2 + \left(2\gamma\frac{\omega}{\omega_0}\right)^2}}. \tag{3}$$

A similar result is obtained for an harmonic force $F = F_0 e^{i(\omega t - i\varphi)} = \hat{F}_0 e^{i\omega t}$

$$\left|\frac{\hat{y}}{\hat{F}_0}\right| = \frac{1}{k}\frac{1}{\sqrt{\left(1-\frac{\omega^2}{\omega_0^2}\right)^2 + \left(2\gamma\frac{\omega}{\omega_0}\right)^2}}, \tag{4}$$

where:
$\hat{x}_1 = \text{complex amplitude of mass oscillation [m]}$,
$\hat{x}_0 = \text{complex amplitude of anchor oscillation [m]}$
$\hat{F}_0 = \text{complex force amplitude [N]}$
$\gamma = \text{decay rate} = D/2\omega_0 m$
$D = \text{damping factor [N/m/s]}$.

Derivation of Eqs. (3) and (4) is found in Appendix 7.2.

As seen in Eqs. (3) and (4), the amplitude of the forced harmonic motion depends on the ratio of applied frequency ω and natural frequency ω_0. Eq. (3) shows that for lowering the resonance frequency ω_0, the fracture $\left|\frac{\hat{y}}{\hat{x}_0}\right|$ increases, thus sensitivity is increased and that the relation between y and ω^2 is directly proportional. This relation motivates why a low resonance frequency accelerometer is necessary for measuring seismic noise. In Eq. (4) Hooke's law is found in the relation of $\hat{y}$, $\hat{F}_0$ and k.

Plotting the amplitude relative to the maximum applied force F_0, as a function of the applied frequency, using Eq. (4), gives the curves shown in Figure 4 for different damping factors D.

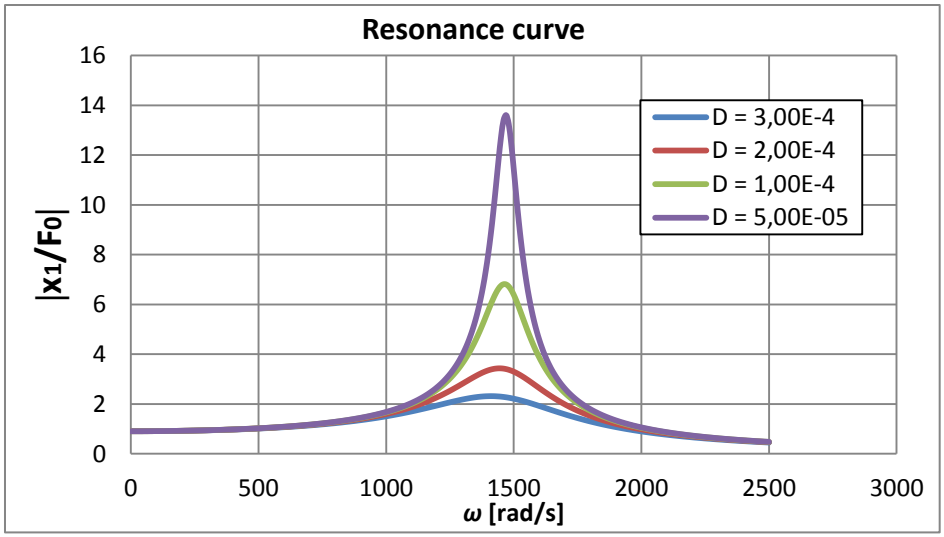

Figure 4: Relative amplitude as a function of the applied frequency.

The frequency ω at which maximum transfer occurs, can be found by equaling the derivative of Eq. (4) to zero:

$$\frac{d\hat{x}_1}{d\omega} = 2m^2\omega^2 - 2km + D^2 = 0\,,$$

giving:

$$\omega_{real} = \sqrt{\frac{k}{m} - \frac{D^2}{2m^2}} = \omega_0\sqrt{1 - \frac{1}{2{Q_0}^2}}\,, \tag{5}$$

The frequency ω_0 is the resonance frequency in the ideal case of no damping. The frequency ω_{real} is the resonance frequency in case of damping. The latter will be named ω_{real} from now on, because this is the actual occurring resonance frequency in practice.

Analogous to ω_{real} there is a corresponding Q-value in case of damping, Q_{real}, which is can be found by substituting Eq. (5) into:

$$Q_{real} = \frac{\frac{A}{F_0}(\omega = \omega_{real})}{\frac{A}{F_0}(\omega = 0)} = \frac{m\omega_0}{D}\frac{1}{\sqrt{1 - \frac{1}{4\left(\frac{m\omega_0}{D}\right)^2}}} = Q_0\frac{1}{\sqrt{1 - \frac{1}{4Q_0^2}}}\,, \tag{6}$$

where:
ω_{real} = angular resonance frequency in case of damping [rad/s]
Q_{real} = quality factor in case of damping [−] .
Q_0 = quality factor in case of no damping (read: low damping)[−] ,

and where $\frac{m\omega_0}{D}$ is defined as Q_0, the quality factor in the ideal case of no damping, which in practice means low damping. The Q-value is related to the bandwidth of the resonance peak as follows:

$$\frac{\omega}{\Delta\omega} = Q \tag{7}$$

Eqs. (5) and (6) show that in case of large damping ($Q \gg 1$), $Q_{real} \approx Q_0$ and consequently $\omega_{real} \approx \omega_0$. In that case it is allowed to consider one value for Q and ω.

2.2 Anti-springs

Anti-spring technology is used in the MEMS accelerometer design to lower the resonance frequency. This technology is also used in some of the mechanical filters for seismic attenuation at Virgo, called GAS filters (Geometric anti-spring) in that case. The principle of an anti-spring is shown in Figure 5 below.

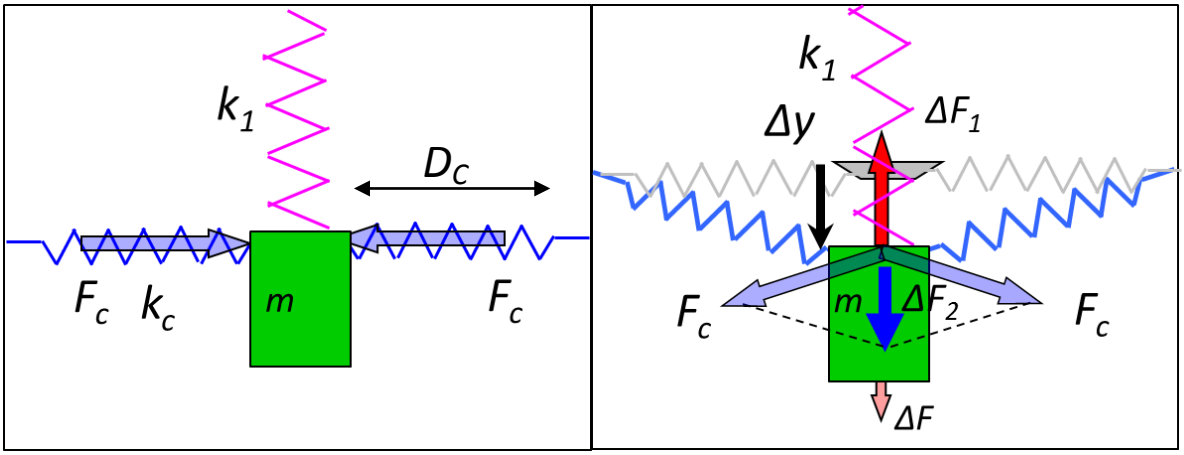

Figure 5: a) Initial state: mass-spring system with spring constant k_1, located between two compression springs with spring constant k_c and compression force F_c each. b) Displaced stage: For a displacement Δy off the proof mass, the upward vertical spring force ΔF_1 is compensated by a downward counteract force ΔF_2, formed by the vertical components of the compression forces F_c. The resulting force ΔF is left, thus the spring constant k_1 in vertical direction is lowered.

By horizontal compression from both sides of the mass of a mass-spring system, the vertical spring constant is lowered when the mass is displaced out of its center position. Less force is needed to displace the mass because of the compression forces F_c compensating the spring counterforce ΔF_1 of the spring with spring constant k_1. The total vertical spring constant is given by:

$$k_{tot} = k_1 - 2\frac{F_c}{D_c}. \tag{8}$$

Derivation of Eq. (8) is found in Appendix 7.3.

This equation shows that the spring constant k_1 is lowered by the horizontal compression force F_c, which is the antispring working principle. The horizontal compression force compensates part of the force needed to displace the mass by having a vertical component opposite to ΔF_1.

In the MEMS design the springs and anti-springs are integrated in a single elastic element: a curved cantilever beam, connecting frame and proof mass. By compressing beam tip and base to each other by a force F_x, the vertical stiffness of the tip ($k_y = \frac{dF_y}{dy}$) tends to decrease, as shown below. Mathematical modeling of the beam is done by considering the moment acting on the beam of initial shape $\theta_i(l)$, see Figure 6.

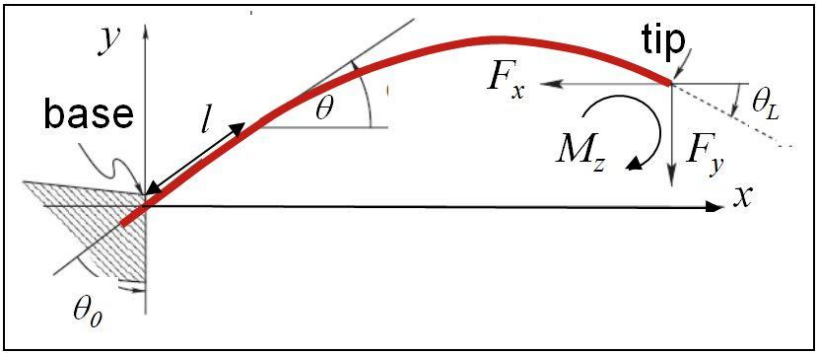

Figure 6: Bending cantilever model sketch.

The sum of moments acting on the beam at each point l, caused by the external forces F_x, F_y and the moment M_L is given by:

$$M(l) = F_y\big(x_L - x(l)\big) - F_x\big(y_L - y(l)\big) + M_L\,, \tag{9}$$

In equilibrium the external moment is balanced by the internal moment, generated when the beam is bend:

$$M = EI\frac{d(\theta - \theta_i)}{dl} \tag{10}$$

Eliminating M from Eqs. (9) and (10), results after differentiating into a second order differential equation in θ:

$$EI\frac{d^2(\theta - \theta_i)}{dl^2} = F_x \sin(\theta) - F_y \cos(\theta)\,, \tag{11}$$

This differential equation can be solved numerical for any given beam shape, x_l and y_l, in particular the tip displacement, x_L and y_L, using boundary conditions: F_x and F_y, with boundary conditions:

$$\theta(0) = \theta_0 \quad , \quad \theta(L) = \theta_L \tag{12}$$

From the resulting θ, the applied forces, F_x and F_y, can be calculated.

l = length parameter along the curved beam shape [m]
$M(l)$ = moment along the beam [Nm]
M_L = moment at the tip of the beam [Nm]
F_y, F_x = static force in oscillation direction and compression direction resp. [N]
$x(l)$ = horizontal coordinate, for values 0 to x_L [m]
$y(l)$ = vertical coordinate, for values 0 to y_L [m]
θ = angle between the horizontal axis x and the beam tangent l [rad]
I = second moment of area [m^4]

The derivation of second moment of area I and general strain and stress in a beam is given in Appendix 7.4. Beam dimensions of the spring present in the MEMS anti-spring design are found in Appendix 7.1.

By calculating F_y for two different beam shapes, the vertical stiffness k_y can be predicted.

Also several FEM models have been made to predict spring behavior (in particular k_x and k_y). 3D and shell models were evaluated using FEM software Abaqus. Moreover FEM software Msc Marc was used to evaluate another shell model for verification of the two FEM simulations. In Figure 7, the FEM Abaqus 3D model is pictured, showing the stress profile in the beam under 20 µm compression.

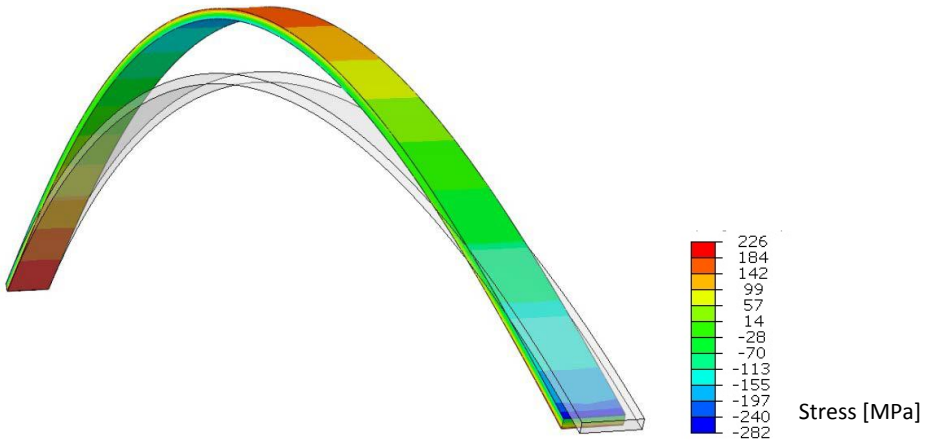

Figure 7: FEM spring model. initial state (see-through) and 20 µm compression state (colored).

The force F_x needed to compress the spring over a certain distance is given in Figure 8, calculated for different modeling methods.

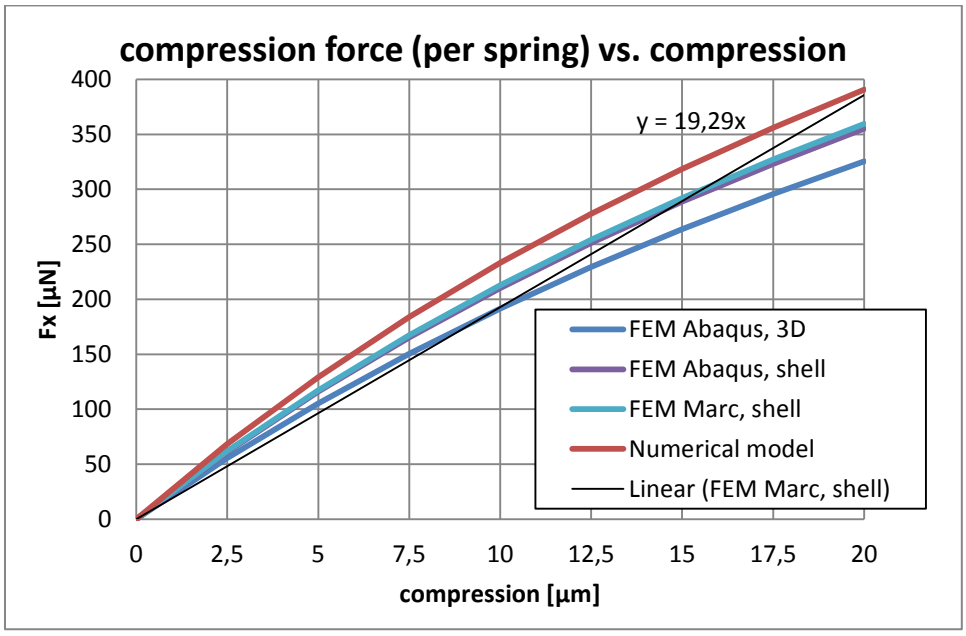

Figure 8: Compression force vs. spring compression. Three FEM models and the numerical model are plotted.

Corresponding behavior of the different FEM evaluations and numerical model is found. The stiffness in the x-direction is approximately constant $k_x = 19{,}3\ \mathrm{N/m}$, as calculated by a linear fit on the average FEM result (FEM Marc shell). The stiffness ranges from $k_x = 27\ \mathrm{N/m}$ at no compression, to $k_x = 12\ \mathrm{N/m}$ at 20 µm compression.

Compressing the beam in the x-direction is expected to reduce the spring constant in the y-direction. The resulting spring constant k_y is given in Figure 9 for different amounts of compression.

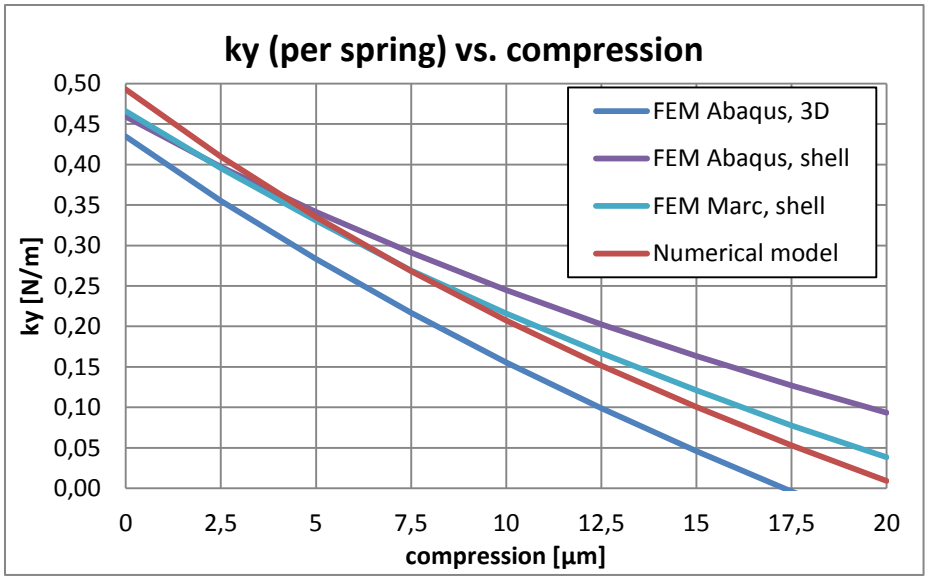

Figure 9: Modeled spring constant vs. spring compression. Three FEM models and the numerical model are plotted.

All model results roughly corresponds to each other. A spring constant $k_y = 0{,}46 \pm 0{,}04$ N/m is expected without compression. Around 20 µm, k_y is expected to reach zero, meaning the spring will become unstable in the y-direction. The maximum required compression is reached around 20 µm. The spring constant directly gives the resonance frequency of the system, considering the used MEMS accelerometer anti-spring design as described in section 3.1.1. The resulting resonance frequency versus compression of the four springs attached to the proof mass is shown in Figure 10.

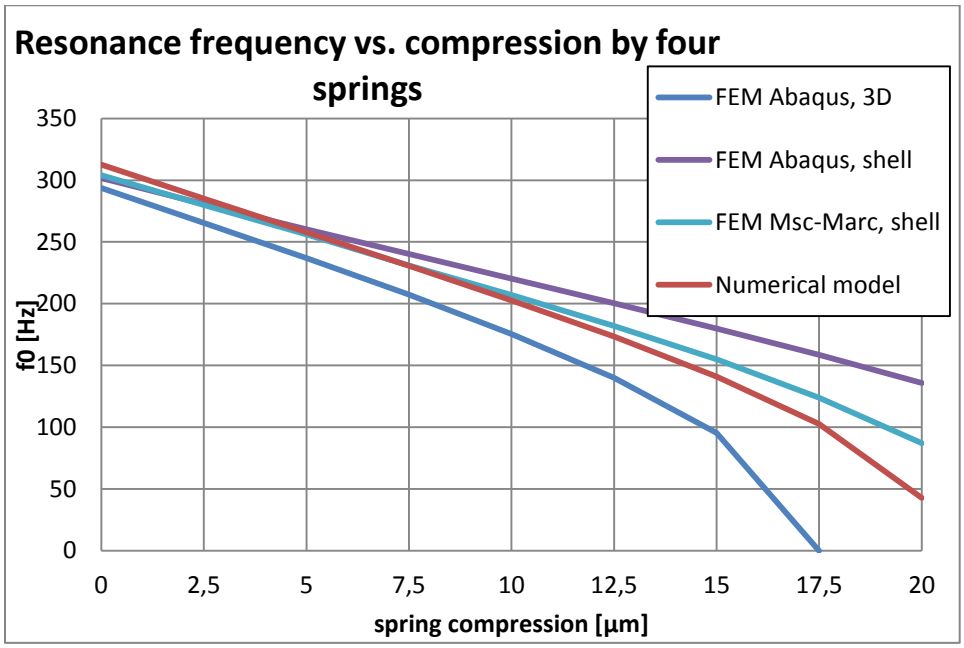

Figure 10: Resonance frequency versus four spring compression. Three FEM models and the numerical model are plotted.

A resonance frequency of $f_0 = 303 \pm 9$ Hz is expected without compression. Linear resonance frequency reduction is expected, at least for compressions up to 15 µm, causing reduction to around 150 Hz. In the most positive case, it is possible to reduce the resonance frequency to values in the order of 10 Hz just by compressing the springs enough. However this is not expected because of the electro-thermal actuator compression range limit, as treated in section 2.4.

2.3 Inverted pendulum

An inverted pendulum is an upright pendulum with its center of mass above its pivot point, see Figure 11. The mass is kept upright by a flexure of stiffness k_L. The effective spring constant is reduced by the gravitational force working on the proof mass. This force is opposite to the spring force, i.e. it acts as anti-spring. See Eq. (13):

$$k_{IP} = k_L - \frac{m g_{grav}}{L_{leg}}, \tag{13}$$

where:
k_{IP} = resulting inverted pendulum spring constant [N/m]
k_L = stiff beam spring constant [N/m]
m = mass [kg]
g_{grav} = gravitational acceleration [m/s^2]
L_{leg} = length of leg [m] .

The derivation of this equation is left unconsidered, because the inverted pendulum MEMS design is not treated in this paper.

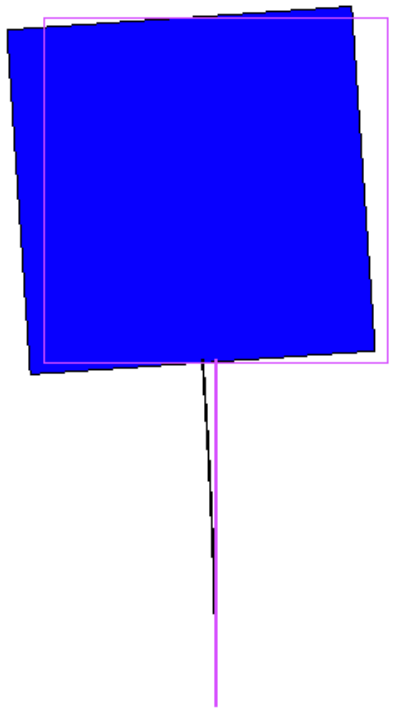

Figure 11: FEM Msc Marc inverted pendulum model.

2.4 Electro-thermal actuators

In the MEMS design, compression of the anti-springs is performed by V-shaped electro-thermal actuators, see Figure 12. These beams are designed to compress the springs by a distance of 20 µm. By applying a voltage over the beam, a current I is generated, dependent on the resistance R of the beam. Joule heating in the beam, which is anchored at both ends, creates an internal stress. Because of the light initial V-shape of the beam, its apex will be pushed outwards. The beam looses most of its heat to the substrate, at a distance of $g = 2$ µm below the beam.

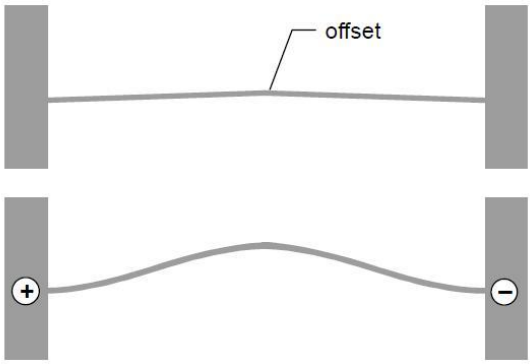

Figure 12: Electro-thermal actuator principle sketch. Top: Lightly v-shaped between fixed between rigid walls. Bottom: Joule heating causes the beam apex to be pushed outwards. [3]

The electro-thermal beams are modeled using Maloney, J.M. [3] and Enikov, E.T. [4] and the Finite Element Method (FEM) software Abaqus. Modeling can be separated in two parts, namely an electro-thermal part and a thermo-mechanical part. The electro-thermal part is only described by Maloney, while the thermo-mechanical part is described by both Maloney and Enikov. ETA beam dimensions present in the MEMS anti-spring design are found in Appendix 7.1.

2.4.1 Electro-thermal model

In the theoretical model of Maloney the temperature of a beam conducting a current is modeled by considering three properties:

1. Beam conduction
2. Heat generation
3. Air gap circulation

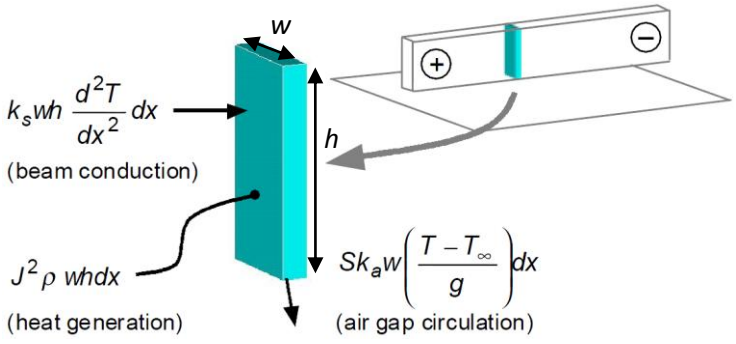

Figure 13: Maloney modeling situation. [3]

Combination of these properties results in the following differential equation:

$$k_s \frac{d^2T(x)}{dx^2} + J^2\rho - Sk_a \frac{T(x) - T_\infty}{gh} = 0\,, \tag{14}$$

where:

$T(x) =$ beam temperature at place x [K]
$T_\infty =$ ambient temperature [K]
$k_s =$ thermal conductivity silicon [$\mathrm{Wm^{-1}K^{-1}}$]
$k_a =$ thermal conductivity air [$\mathrm{Wm^{-1}K^{-1}}$]
$J =$ current density [$\mathrm{Am^{-2}}$]
$\rho =$ resistivity silicon [Ωm]
$S =$ geometry factor [$-$]
$g =$ gap between device layer and substrate [m]
$h =$ height device layer $=$ thickness beam [m] .

The geometry factor S takes into account thermal conduction from the sides of the beam, through the surrounding air, to the substrate, see Figure 14. This factor is the ratio of heat loss from the sides and bottom of the beam to heat loss from the bottom of the beam only. S is given by:

$$S = \frac{4}{w_V^*}(10^{-6}\,\mathrm{m} + g)\,, \tag{15}$$

where:
$w_V^* =$ effective beam width [m] .

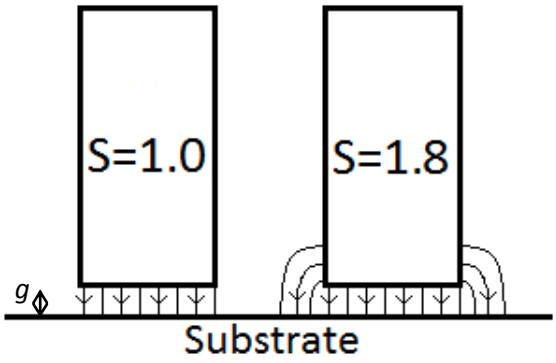

Figure 14: S factor sketch. Additional heat loss from the sides of the ETA beam enlarges the total heat loss to the substrate.

The MEMS design ETA beam has perforated structure, as shown in 2.4.2, Figure 19. This geometry causes larger joule heating compared to a solid beam, when applying an equal current through the beam. Furthermore stiffness in the actuation direction is lowered by perforation, increasing beam deflection. The effective beam width is the width of a solid beam, having the same electrical and thermal resistivity as a wider perforated beam. The effective beam width is found to be 14 µm by matching the solid beam electrical resistivity to the value for a perforated beam having a beam width of 18 µm, using FEM modeling.

Eq. (14) can be solved analytical, assuming constant silicon resistivity and constant thermal conductivity of silicon and air, with temperature and pressure. The analytical solution is given in Eq. (16).

$$T(x) = T_\infty + \frac{J^2\rho}{k_s m^2}\left(1 + \frac{1 - e^{-mL_V}}{e^{-mL_V} - e^{mL_V}}e^{mx} + \frac{1 - e^{mL_V}}{e^{mL_V} - e^{-mL_V}}e^{-mx}\right), \tag{16}$$

where:
$L_V =$ ETA beam length [m] .

The derivation is given in Appendix 7.5.

In the model of Maloney, heat loss by surface radiation is neglected compared to air gap circulation. However in case of low air pressure, heat loss by air gap circulation is reduced because of lowering thermal conductivity of air k_a, and heat loss by surface radiation becomes substantial. Surface radiation is added to the differential equation of Maloney, resulting in:

$$k_s \frac{d^2T(x)}{dx^2} + J^2\rho - Sk_a \frac{T(x) - T_\infty}{gh} - 2\sigma\varepsilon \frac{w_V^* + h}{w_V^* h}(T^4 - T_\infty^4) = 0\,, \tag{17}$$

where:
$\sigma = \text{Stefan} - \text{Boltzmann constant}\ [\mathrm{Wm^{-2}K^{-4}}]$
$\varepsilon = \text{emissivity}\ [-]$.

Furthermore, in our case silicon resistivity and thermal conductivity of silicon are considered dependent on temperature. Thermal conductivity of air is, besides temperature, also considered dependent on pressure. Eq. (17) cannot be solved analytically, so it is solved numerically, including all dependencies named. Thermal conductivity of silicon and air versus temperature are given in Appendix 0, Figure 71 and Figure 72 respectively. Also pressure dependency of thermal conductivity of air for gap geometry is given in Appendix 0, Figure 73.

Silicon resistivity is solved for dependency of temperature:

$$\rho = \rho_0\big(1 + \beta(T(x) - T_\infty)\big)\,, \tag{18}$$

where:
$\rho_0 = \text{resisivity silicon at ambient temperature}\ [\Omega\mathrm{m}]$
$\beta = \text{linear constant}\ [\mathrm{K^{-1}}]$.

Both parameters ρ_0 and β have been fitted to measurements of the beam resistance R versus the current I, assuming an average beam temperature $\bar{T}$, estimated from Eq. (19). The R vs. I measurements are shown in section 0, Figure 56.

$$P = I^2R = (\bar{T} - T_\infty)\frac{Sk_aL_Vw_V^*}{g}\,, \tag{19}$$

where:
$P = power\ [W]$
$I = current\ through\ beam\ [A]$
$R = beam\ resistance\ [\Omega]$
$\bar{T} = average\ beam\ temperature\ [K]$.

The relation between voltage and current is modeled using the average silicon resistivity ρ_{gem} for a given beam temperature in the formula for beam resistance $R = \rho\frac{l}{A}$.

$$U = IR = I\frac{L_V}{w_V^* h}\,\rho_{gem}\,. \tag{20}$$

Correspondence of model and measurements for current versus voltage for the ETA beam is shown in 0, Figure 55.

Moreover the ETA beam is modeled using FEM Abaqus. The evaluated beam temperature profile is shown in 2.4.2, Figure 19.

Eq. (17) is solved numerically including all temperature and pressure dependencies noted. Solved maximum and average beam temperature versus current applied through the beam are shown in Figure 15 below. Also maximum beam temperature FEM results are plotted.

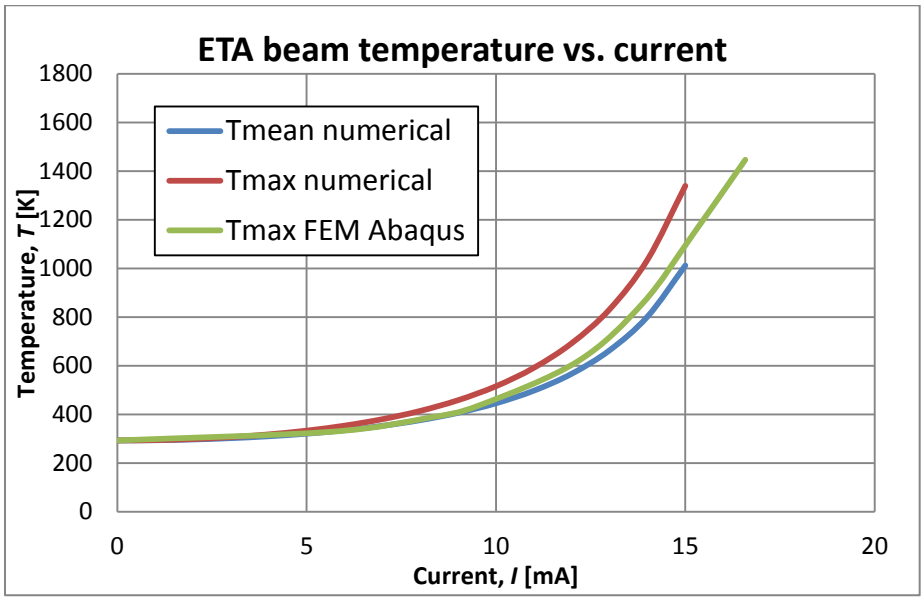

Figure 15: Modeled maximum and average beam temperature vs. applied current through the beam, numerical model and FEM Abaqus simulation.

The FEM model predicts lower beam temperatures, of up to $70\ \mathrm{K}$ difference with the numerical results at a current of $15\ \mathrm{mA}$. Silicon has a melting point of $T = 1683\ \mathrm{K}$, predicting meltdown of the ETA beam around $I = \ 15 - 17\ \mathrm{mA}$.

Average beam temperature is also modeled for air thermal conductivity of $k_a = 2{,}3 \cdot 10^{-6}\ \mathrm{Wm^{-1}K^{-1}}$, shown in Figure 16, corresponding to a pressure of $p = 1 \cdot 10^{-2}$ mbar. Beam temperature is chosen to be calculated for this pressure of $p = 1 \cdot 10^{-2}$ mbar, because at this pressure dominant damping factors are predicted to be canceled, as treated in sections 2.6 and 3.6.

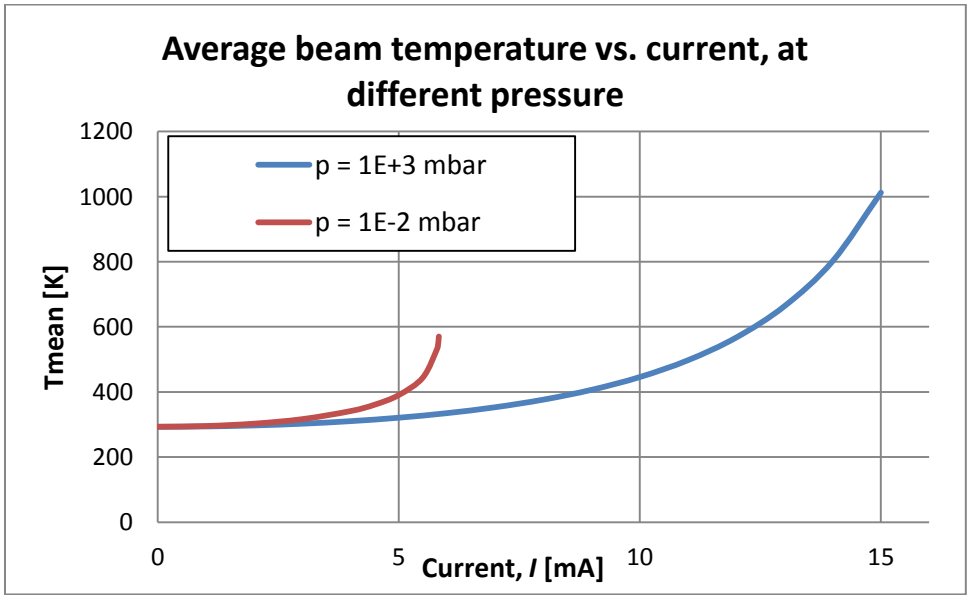

Figure 16: Modeled mean beam temperature versus applied current through the beam. For standard pressure and evacuation to a pressure of 0,01 mbar.

Thermal conduction to the substrate is the dominant heat loss factor. The 2 µm gap between beam and substrate causes major heat transfer. (See Appendix 0, Figure 73). Lowering pressure, lowers thermal conductivity k_a, thus linearly lowering thermal conduction to the substrate (air gap circulation, Eq. (14)). This means evacuation causes beam temperature to rise much faster. For a pressure of $p = 1 \cdot 10^{-2}$ mbar, the beam is expected to melt already around $I = 6$ mA.

2.4.2 Thermal-mechanical model

The thermal-mechanical part of the Electro-thermal beam model is based on Enikov, E.T. [3]. When a V-shaped beam, anchored at its ends, expands because of thermal excitation, its apex will be pushed outwards. In this way a certain force can be exerted on an object, for example to compress springs. The deformation which takes place in the beam can be divided into stretching in longitudinal direction and bending in transverse direction. In Figure 17 the modeling situation is shown. Because of symmetry only half of the beam is modeled.

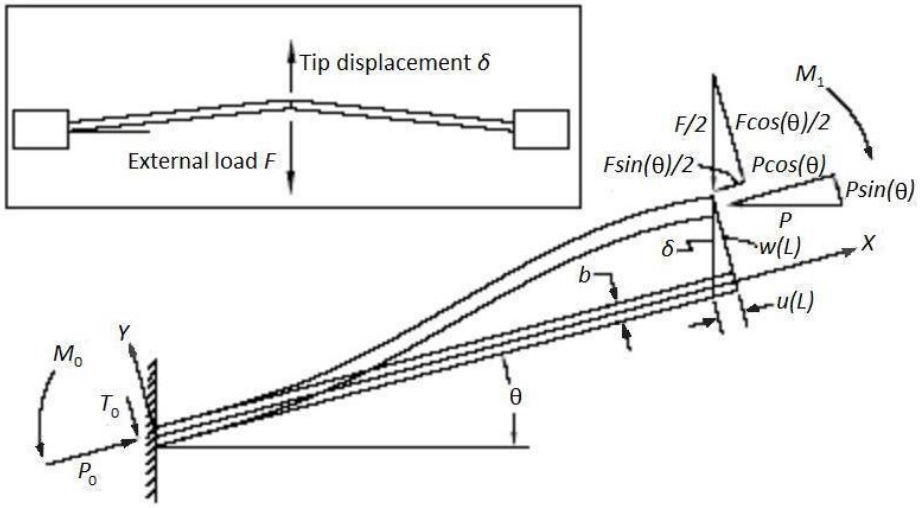

Figure 17: ETA beam, shape deformation and loads. [4, improved symbol resolution]

The bending behavior can be described as the bending of a beam into another radius of curvature, as seen in Appendix 7.4. In this case the neutral axis of the beam stays the same length, while the upper half stretches and the lower half compresses. The strain by bending of the beam is described by:

$$\varepsilon = \frac{d\theta(R_0 + y) - d\theta R_0}{d\theta R_0} = \frac{y}{R_0} = yw'' \ , \tag{21}$$

where:
$\varepsilon =$ transversal strain $[-]$
$\theta =$ initial angle of V $-$ shaped beam [rad]
$R_0 =$ radius of curvature of the natural axis [m]
$y =$ maximum transversal distance from natural axis [m]
$w =$ transverse displacement of the beam [m] .

Because of joule heating the beam expands. This expansion mainly has effect on the beam length, stretching the beam. Strain by stretching of the beam is described by:

$$\varepsilon_x^0 = 1 + \frac{1}{2}\left[2u' + u'^2 + w'^2\right] - 1 = u' + \frac{1}{2}\left[u'^2 + w'^2\right] \ , \tag{22}$$

where:
$\varepsilon_x^0 =$ longitudinal strain $[-]$
$u(x) =$ longitudal displacement of the beam [m]
$w(x) =$ transverse displacement of the beam [m] .

Adding bending and stretching strain results in the total strain of the beam, given by:

$$\varepsilon_x = \varepsilon_x^0 - \varepsilon = u' + \frac{1}{2}\left[u'^2 + w'^2\right] - yw'' , \tag{23}$$

where:
$e_x =$ total strain $[-]$.

The derivation of Eqs. (21) and (22) can be found in Appendix 7.6.

The ETA beams are fixed between two rigid walls. When the beam is heated stress is built in the beam material, instead of actual lengthening of the beam.

The total virtual thermal strain equation is given by:

$$\varepsilon_x^0 - \alpha\Delta T = -\frac{P_0}{EA} . \tag{24}$$

The total moment equation is given by:

$$EIw'' + P_0 w = -T_0 x - M_0 , \tag{25}$$

where:
$\alpha =$ thermal expansion coefficient $[-]$
$E =$ Young's modulus [Pa]
$I =$ second moment of area $[\mathrm{m}^4]$
$P_0 =$ longitudinal force on beam fixed end [N]
$T_0 =$ tranversal force on beam fixed end [N]
$M_0 = m$oment on beam fixed end [Nm] .

Derivation of Eqs. (24) and (25) is found Appendix 7.6.

The set of differential equations, Eqs. (24) and (25), is solved for $w(x)$, resulting in:

$$w(x) = \left(\tan\theta - \frac{F}{2k^2 EI\cos\theta}\right)\left(\frac{\sin kx}{k} + \frac{(\cos kL - 1)(\cos kx - 1)}{k\sin kL} - x\right), \tag{26}$$

where $k = \sqrt{\frac{P_0}{EI}}$ is found by solving the transcendental equation $c(k, F, \bar{T})$.

Solving k results in the tip displacement:

$$\delta = \frac{w(L)}{\cos\theta} = \left(\frac{2k^2 EI\sin\theta - F}{2k^2 EI(\cos\theta)^2}\right)\left(\frac{2\tan\frac{kL}{2} - kL}{k}\right) . \tag{27}$$

Derivation of Eq. (27) is found in Appendix 7.6.

Tip displacement, without external load F, is calculated numerically for $p = 1 \cdot 10^{3}$ mbar and $p = 1 \cdot 10^{-2}$ mbar and with FEM Abaqus for $p = 1 \cdot 10^{3}$ mbar. The results are shown in Figure 18.

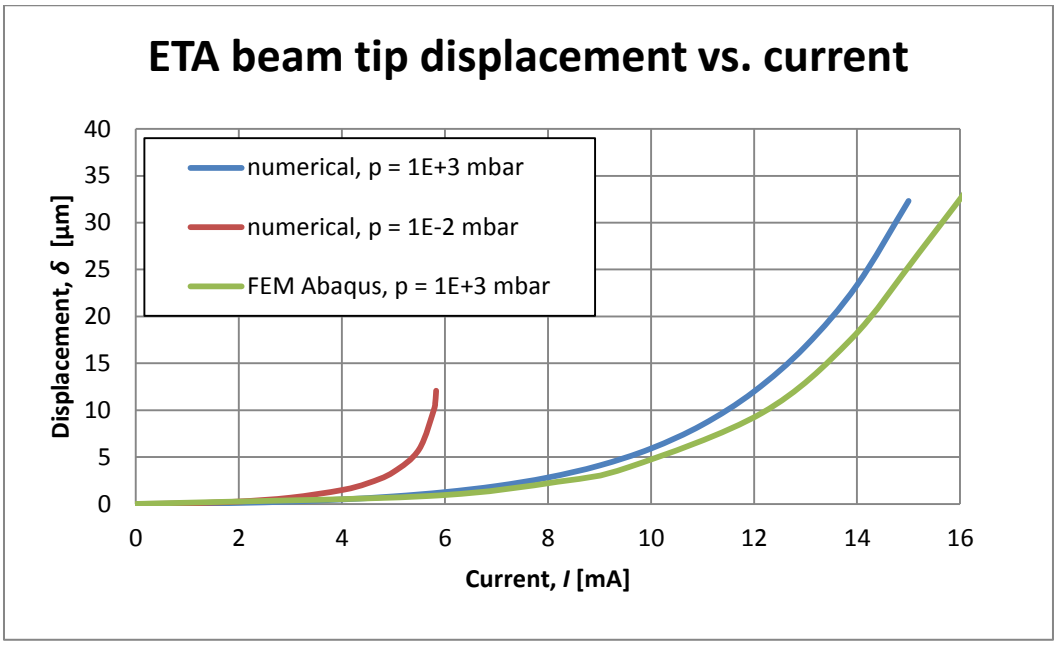

Figure 18: ETA beam tip displacement versus current applied through beam, numerical and FEM Abaqus results. Numerical result for standard pressure and evacuation to a pressure of 0,01 mbar. No external load applied.

In case of standard pressure and no external load, a maximum tip displacement of 25-35 µm is expected from modeling. At this point ($I = 15$ mA) the beam temperature maximum comes near the melting point of silicon at $T = 1683$ K, weakening the beam structure. For evacuation to a pressure of $p = 1 \cdot 10^{-2}$ mbar, much less displacement is predicted. Taking into account spring compression of around 20 µm is demanded for substantial resonance frequency reduction, it is predicted that the ETA beams won't be able to compress the anti-springs sufficient in vacuum.

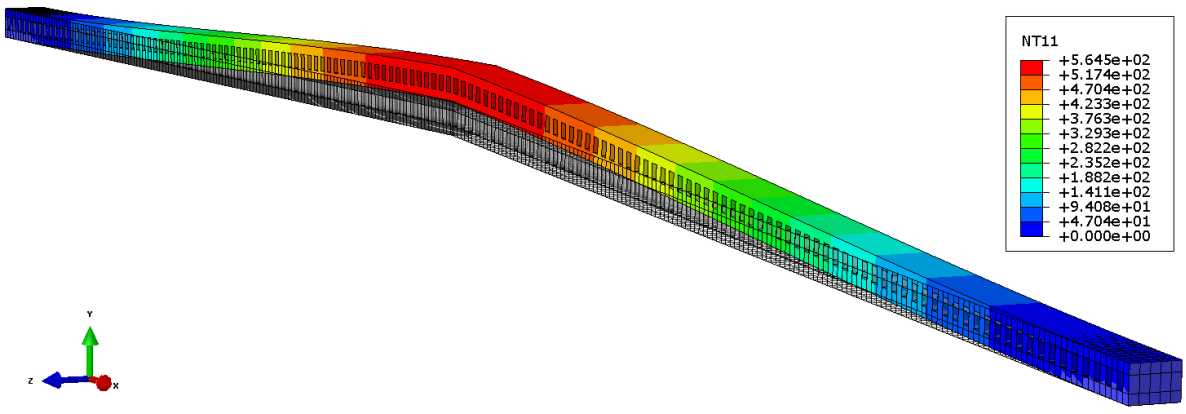

Figure 19: ETA beam FEM model, temperature distribution ($T - T_{\infty}$) and displacement of 17,54 µm for a voltage of $U = 20$ V applied over the beam.

In case of an external load applied to the ETA beam tip, in the shape of a structure that needs to be compressed, the tip displacement will be less for the same temperature profile. In Figure 20 beam tip

displacement is plotted for no tip load and for added counter force F_x of the anti-spring for standard pressure modeled in section 2.2. Also FEM Abaqus results for no tip load and anti-spring load are plotted.

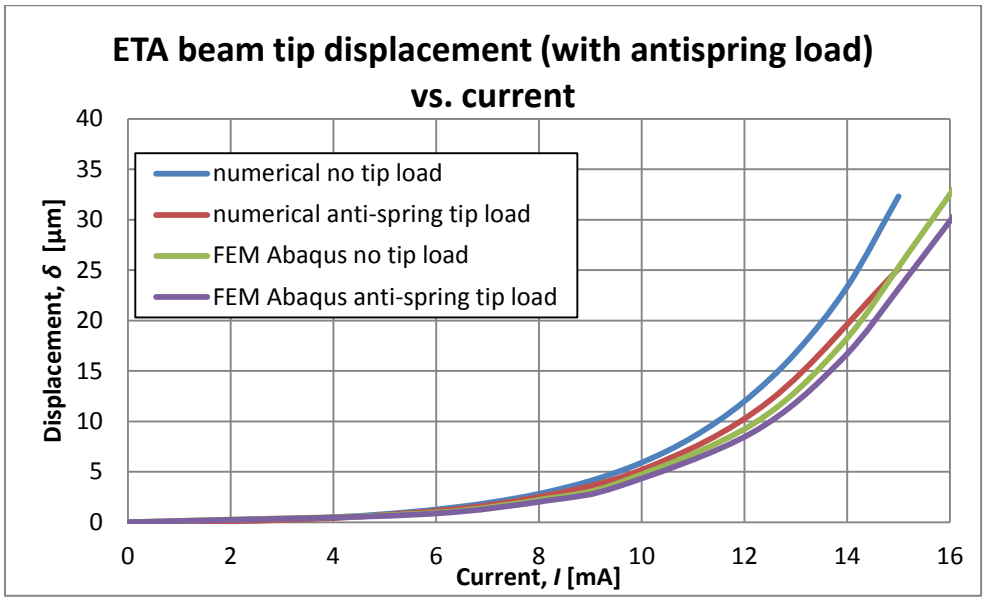

Figure 20: numerically modeled tip displacement versus current in case of no tip load and antispring tip load.

In practice, in the MEMS design not only the anti-spring has to be compressed, but also an intermediate structure between ETA beam and anti-spring. In this case the tip load is modeled as a spring load with a certain spring constant k_{tot} which is the sum of the spring constant $_x$ of the anti-spring and the spring constant $k_s$of the intermediate structure. In Figure 21 FEM Abaqus results of tip displacement for no tip load is repeated, combined with spring tip load cases, having spring constant k_{tot}.

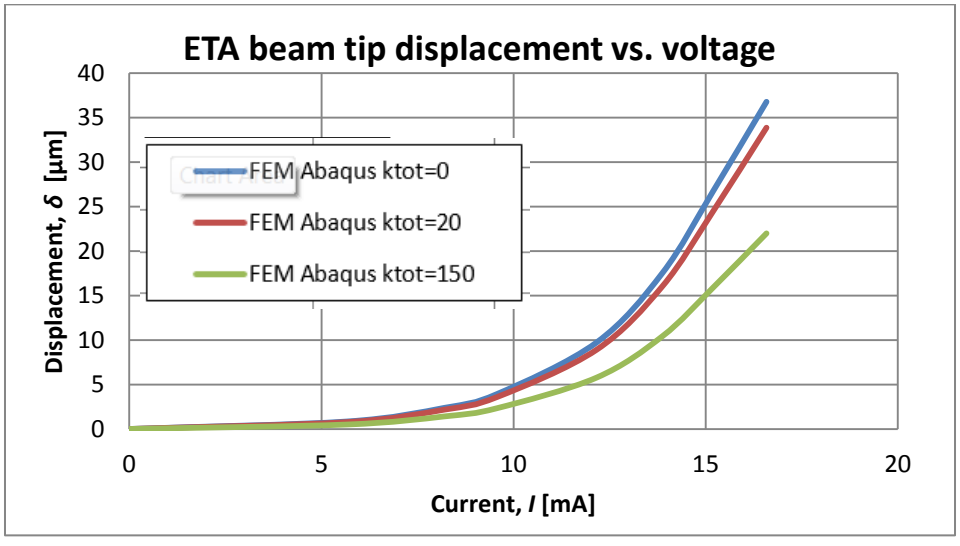

Figure 21: FEM Abaqus evaluated tip displacement versus current in case of several spring tip loads with different spring constant k_s.

The different intermediate structures are modeled using FEM and the spring constant k_s is calculated per structure. This analysis is treated in section 3.1.1.

2.5 Capacitive actuating and sensing

Rows of capacitive 'fingers' are attached to the mass of the MEMS chip, called combs. There are two actuation comb rows, one on top and one on the bottom. There are also two sensing comb rows, one on the left and one on the right. Applying a voltage over the actuating comb pair actuates the mass. Conversely the movement of the mass can be sensed using a second comb pair.

2.5.1 Actuation combs

Actuation combs are situated above and below the proof mass. In Figure 22 part of a comb actuator row is shown.

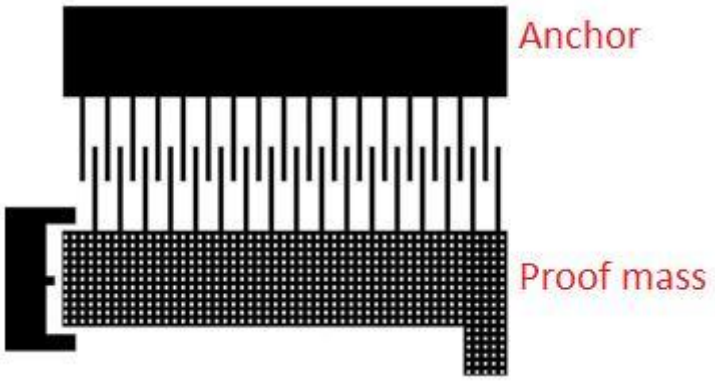

Figure 22: Left: Left part of top actuator comb.

Applying a DC voltage U over one comb actuator, results in a pulling force F on the mass, whereupon a displacement in y-direction of the mass occurs. The displacement changes capacitor plate area and thus the pulling force:

$$F = \frac{dE_{pot}}{dL_A} = \frac{N_A h \varepsilon_0}{2d} {U_A}^2 C_C \,, \tag{28}$$

where:
E_{pot} = potential energy [J]
L_A = actuation comb finger overlap [m]
N_A = number of finger pairs per actuation comb [−]
h = height device layer [m]
d = distance between actuation fingers [m]
ε_0 = permittivity of air [Fm^{-1}]
U_A = applied voltage [V]
C_C = capacitance geometry factor [−] .

The capacitance geometry factor corrects for the geometry with respect to the ideal parallel plate model, described in 2.5.3. Results of Eq. (28) for applied voltage U_A are shown in Figure 23.

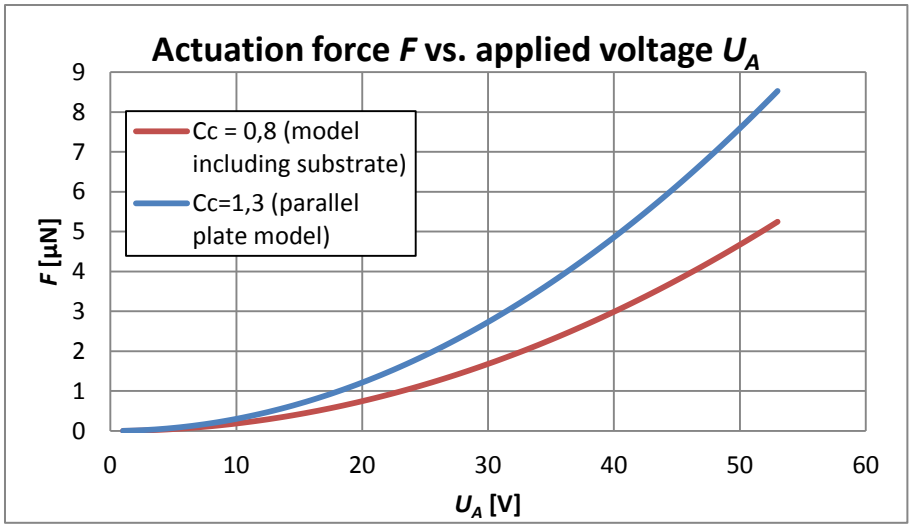

Figure 23: modeled displacement of actuation force F versus voltage U_A applied over one actuator comb row, for two possible capacitance geometry factors.

The pulling force is related to the displacement in y-direction by the spring constant of the system:

$$\Delta y = \frac{F}{4k_{spring}}, \tag{29}$$

where:
$\Delta y =$ displacement out of center distance d [m]
$F =$ force exerted by actuation comb [N]
$k_{spring} =$ spring constant per spring [N/m] .

Modeling results of Δy versus U_A, combined with measurement results, are shown in section 4.1.1, Figure 54.

In practice, the anchor is given a positive potential, while the proof mass is connected to ground. It is only possible to exert a pulling force on the mass. A negative applied potential to the outside comb wouldn't create a pushing force, but also a pulling force. Thus an equal DC voltage applied over both actuator comb rows would result in zero displacement of the mass, even if both voltages have opposite sign. Therefore, in case of DC voltage for actuation, always one comb row is used.

By applying an AC voltage over an actuator comb, the mass can be brought in harmonic motion. In case of AC voltage application, both actuator combs are used in anti-phase combined with an offset. See Figure 24.

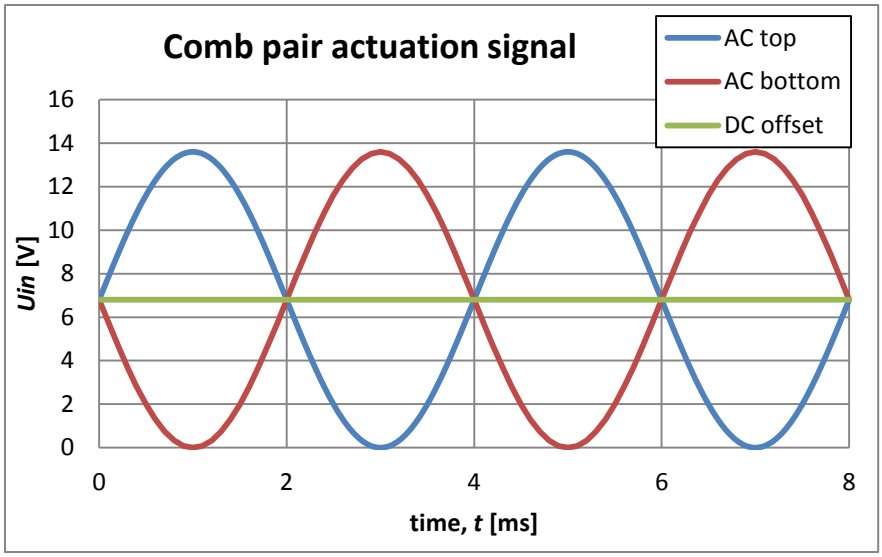

Figure 24: Comb pair actuation input voltage for top and bottom, pulling in anti-phase.

The top actuator comb pulls in anti-phase compared to the bottom actuator comb, creating an AC motion of the mass. The DC offset brings the whole signal above zero, creating maximal force. Furthermore the DC voltage won't offset the mass, because both comb actuators pull equally DC wise.

2.5.2 Sensing combs

Sensing combs are situated left and right of the proof mass, consisting of capacitance fingers separated by two different distances. Furthermore sensing comb are mirrored over the center, see Figure 25. This mirrored structure prevents proof mass actuation by the read-out voltage applied to the sensing combs. Furthermore non-linear sensing behavior is reduced.

Displacement of the mass in y-direction results in change of distance between the sensing comb capacitor plates. We distinguish the plate distance d_S for the 10 µm gap and d_{Sbig} for the 30 µm gap. When the mass moves upwards this results in a top part distance reduction of d_S and increase of d_{Sbig}. On the bottom part, the distance d_S increases and d_{Sbig}decreases.

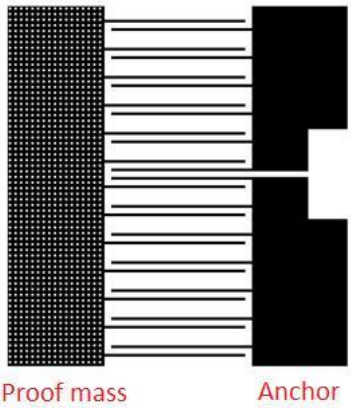

Figure 25: Middle part of left sensing Comb. The top and bottom part of the sensing Combs are reversed, removing non-linear behavior.

The capacitance change for one part of the comb is given by

$$C_{S\pm} = \frac{\varepsilon_0 h L_S}{d_S \pm \Delta y} \,, \tag{30}$$

$$C_{Sbig\pm} = \frac{\varepsilon_0 h L_S}{d_{Sbig} \pm \Delta y} \,, \tag{31}$$

where:
$C_S =$ sensing capacitance small gap [F]
$C_{Sbig} =$ sensing capacitance big gap [F]
$L_S =$ sensing comb finger overlap [m]
$d_S =$ distance between sensing fingers small gap [m]
$d_{Sbig} =$ distance between sensing fingers big gap [m] .

The total capacitance of a comb row is the sum of C_S and C_{Sbig} with opposite sign, times the number of capacitors. Both top part and bottom part have to be added:

$$C_{tot} = C_{S\pm} + C_{Sbig\mp} + C_{S\mp} + C_{Sbig\pm} \,. \tag{32}$$

For example, for upward displacement of the mass, the total capacitance of the comb row is given by:

$$C_{tot} = C_{S-} + C_{Sbig+} + C_{S+} + C_{Sbig-}$$

For both combs summed, the total capacitance is given versus vertical displacement in Figure 26.

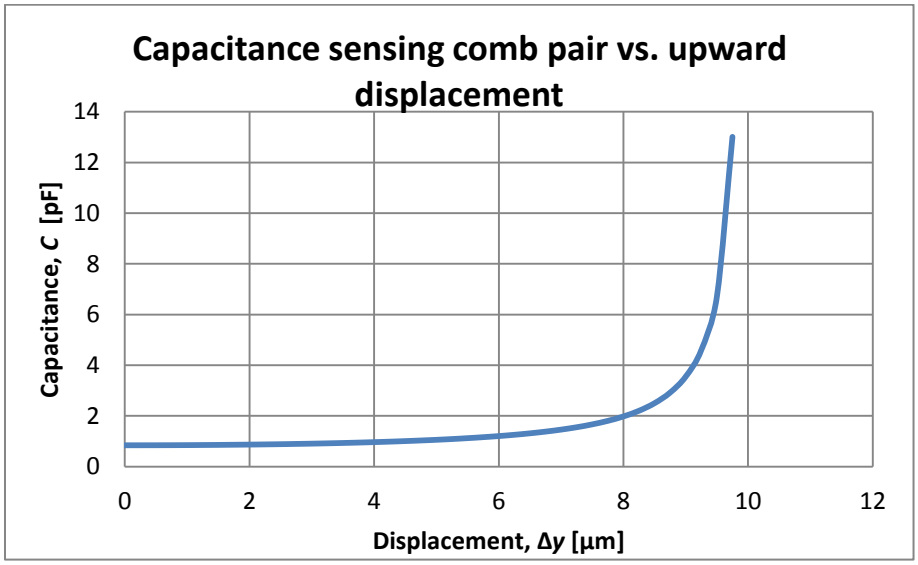

Figure 26: total capacitance sensing comb pair versus vertical displacement Δy.

Up to $\Delta y = 6$ µm, the relation between capacitance and displacement is expected to be linear. The total capacitance goes up to infinity for large vertical displacement, because the capacitance plate distance d_S approaches zero.

2.5.3 Capacitance geometry factor

The capacitance geometry factor C_C corrects for the geometry with respect to the ideal parallel plate model. When looking at a actuator comb row, a single parallel plate capacitor consists of two adjacent comb fingers. The fingers partly overlap, having an overlap length L_A. The finger fixed to the anchor has applied potential U_A. The finger attached to the proof mass has ground potential. Second feature of the geometry is the substrate laying 2 µm below the comb row and also having ground potential. The unit cell of such a capacitor is shown in Figure 27, in FEM software Msc Marc, consisting of two adjacent fingers of half the finger thickness and the underlying substrate.

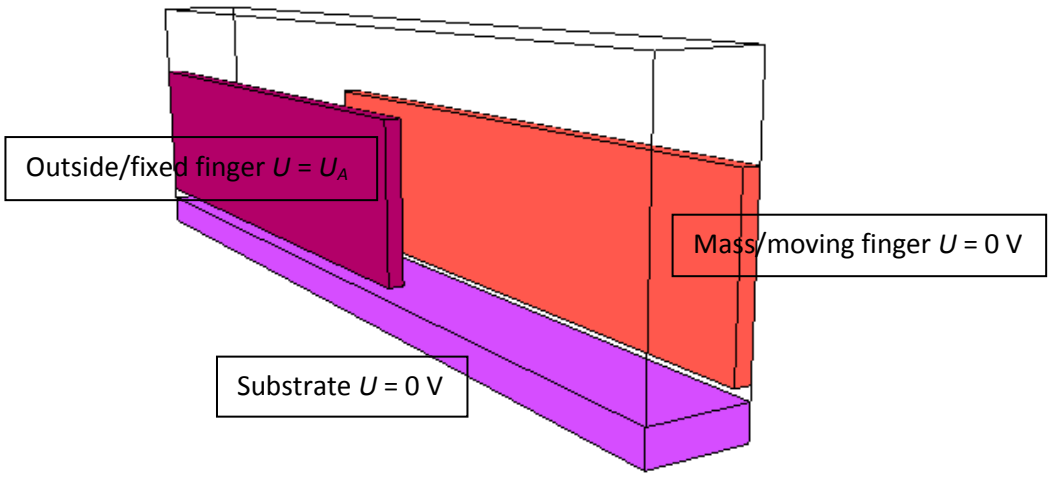

Figure 27: 3D geometry FEM Msc Marc unit cell. Single parallel plate capacitor, consisting of two adjacent comb fingers

The capacitance of the ideal parallel plate capacitor would be:

$$C = \frac{\varepsilon_0 h L_A}{d}. \tag{33}$$

This capacitance is expected to be larger in case of two plates overlapping, creating a larger plate area. According to the FEM simulation, the capacitance factor should be $C_C = 1{,}3$ in this case. However in case of an added substrate at gap distance $g = 2$ µm, the factor is evaluated to be $C_C = 0{,}8$. This $C_C < 1$ is explained by the fact that part of the electric field lines end up at the substrate instead of going to the adjacent finger surface, lowering capacitance of the plate capacitor. compare Figure 28 left and right.

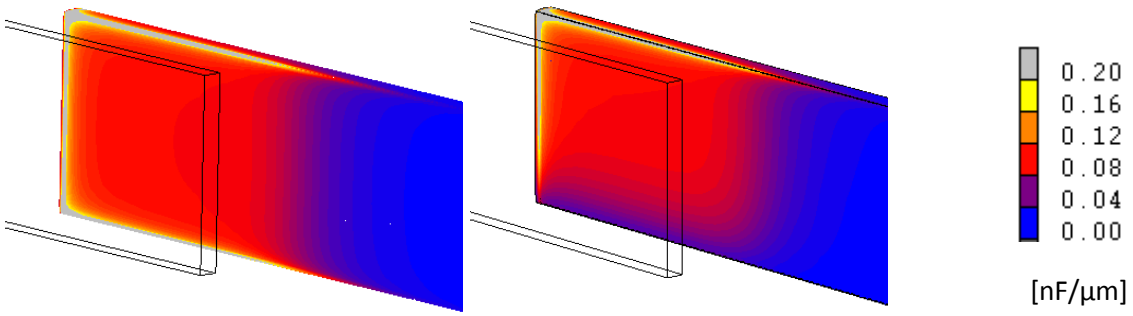

Figure 28: Electric field strength on the mass/moving finger surface for situation [left] without substrate and [right] with substrate.

2.6 Damping

The damping factor D, as introduced in 2.1.1, is defined as force per velocity. In case of the MEMS accelerometer, damping mainly consists of drag force and squeeze film damping. Drag force is dominated by drag force between substrate and proof mass, given by:

$$D_{drag} = \mu_{air} \frac{A}{g}, \tag{34}$$

where:
$D_{drag} =$ damping factor for drag between sliding surfaces $[\mathrm{N/(m/s)}]$
$\mu_{air} =$ viscosity of air $[\mathrm{kg/(m/s)}]$
$A =$ area of sliding surfaces $[\mathrm{m}^2]$
$g =$ gap between sliding surfaces $[\mathrm{m}]$.

Squeeze film damping is caused by the compression and decompression of air between two close by moving surfaces. This damping type is dominated by distance change between the sensing comb fingers, calculated using Hermann, A. [5]:

$$D_{squeeze} = \frac{96}{\pi^4} \mu_{air} \frac{L^3 h^3}{L^2 + h^2} \left(\frac{1}{d^3}\right), \tag{35}$$

where:
$D_{squeeze} =$ squeeze film damping factor $[\mathrm{N/(m/s)}]$
$L =$ overlap length of capacitance fingers $[\mathrm{m}]$
$h =$ width capacitance fingers $=$ heigth device layer $[\mathrm{m}]$
$d =$ distance between capacitance fingers $[\mathrm{m}]$.

The total squeeze film damping caused by the sensing combs is found by summing the damping for all small and big sensing gaps:

$$D_{squeeze}(d = d_S) * N_S + D_{squeeze}(d = d_{Sbig}) * N_{Sbig}\ , \tag{36}$$

where:
$N_S =$ number of small sensing gaps for comb pair $[-]$
$N_{Sbig} =$ number of big sensing gaps for comb pair $[-]$.

The total drag damping factor is calculated to be $D_{drag} = 1{,}06 \cdot 10^{-4}\ \mathrm{N/(m/s)}$ and the total squeeze damping by the sensing combs is calculated $D_{squeeze} = 8{,}31 \cdot 10^{-6}\ \mathrm{N/(m/s)}$. This predicts that the drag force between substrate and proof mass is the dominant damping component of the MEMS design, by a factor more than 10. The total damping is thus predicted to be $D = 1{,}15 \cdot 10^{-4}\ \mathrm{N/(m/s)}$.

Eqs. (34) and (35) show that the dominant damping types are dependent on μ_{air}. Evacuation of the MEMS is predicted to result in negligible damping, and consequently a high Q-value of the MEMS accelerometer, see section 2.1.1, Eq. (6).

3 Measurement setup and methods

Four different proof of principle MEMS accelerometer designs are tested. Three designs include anti-springs, the fourth design is based on the inverted pendulum. The main design feature is high sensitivity at low frequencies, which requires a low resonance frequency of the oscillator. As shown in Eq. (2) this is achieved by a low spring constant k and a large mass m. With the anti-spring design this is achieved by compression of the circular beams which function as springs. For the inverted pendulum this is achieved by a large mass on top of a long stiff leg. The MEMS designs are etched out of a silicon on insulator wafer by MESA+ (Institute for Nanotechnology).

Because the MEMS accelerometer project is in a proof-of-principle stage, the current design is not yet optimized for purposed low resonance frequencies combined with high sensitivity. In future optimization designs, the mass will be made heavier and the geometry will be optimized for low damping and noise.

At first hand, observation and displacement measurements of the MEMS were done using microscope. Several quality checks were done using electron microscope imaging, checking surfaces and connections. Later electronics were finished for accurate displacement sensing and on board actuation of the MEMS.

Damping factors are analyzed by evacuation of the MEMS in a vacuum chamber. Reducing air pressure, mainly reduces air film damping, raising the Q-value of the oscillator. The main aim of evacuation is knowing the mechanical and electronic noise by canceling the noise component of air damping.

3.1 MEMS accelerometer designs

3.1.1 Anti-spring design

The anti-spring MEMS design is shown below in Figure 29. It consists of a mass, attached to the intermediate mass by four circular springs. The intermediate mass can be pushed towards the mass by using V-shaped electro-thermal actuators, compressing the anti-springs.

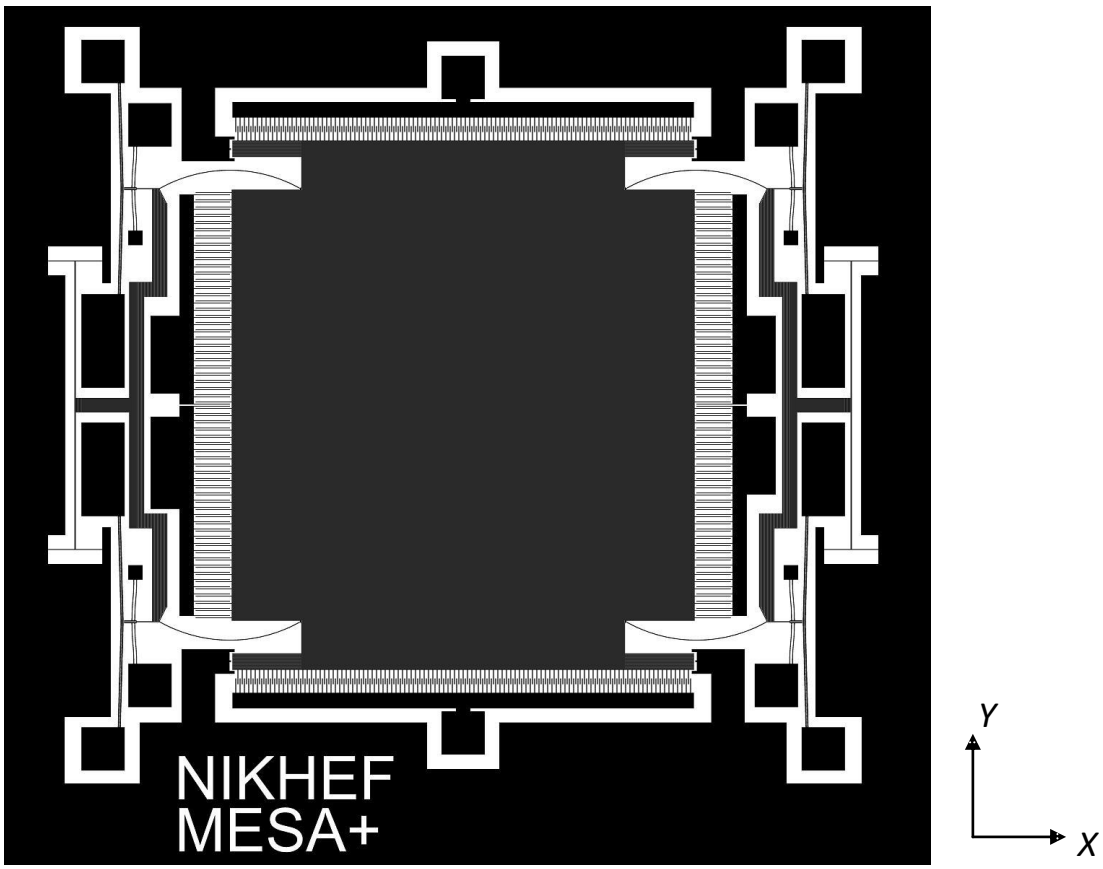

Figure 29: G2 anti-spring MEMS design schematic.

The anti-springs present in the MEMS anti-spring design are situated between proof mass and intermediate mass, as showed in Figure 30. The springs are circular shaped cantilever beams in their relaxed state. Pushing the intermediate mass towards the proof mass will compress the anti-springs, lowering the spring constant k_y in y-direction, see Figure 31. Because compression is applied from opposing sides, the proof mass will remain centered.

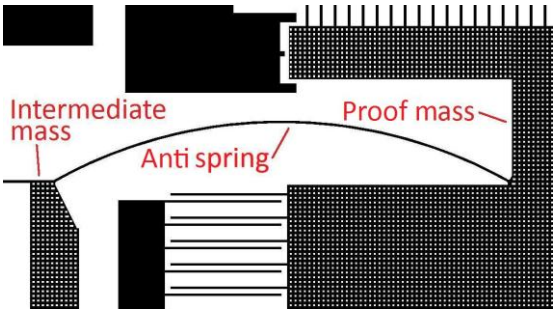

Figure 30: Outtake of the MEMS design schematic, showing a circular anti-spring between proof mass and intermediate mass.

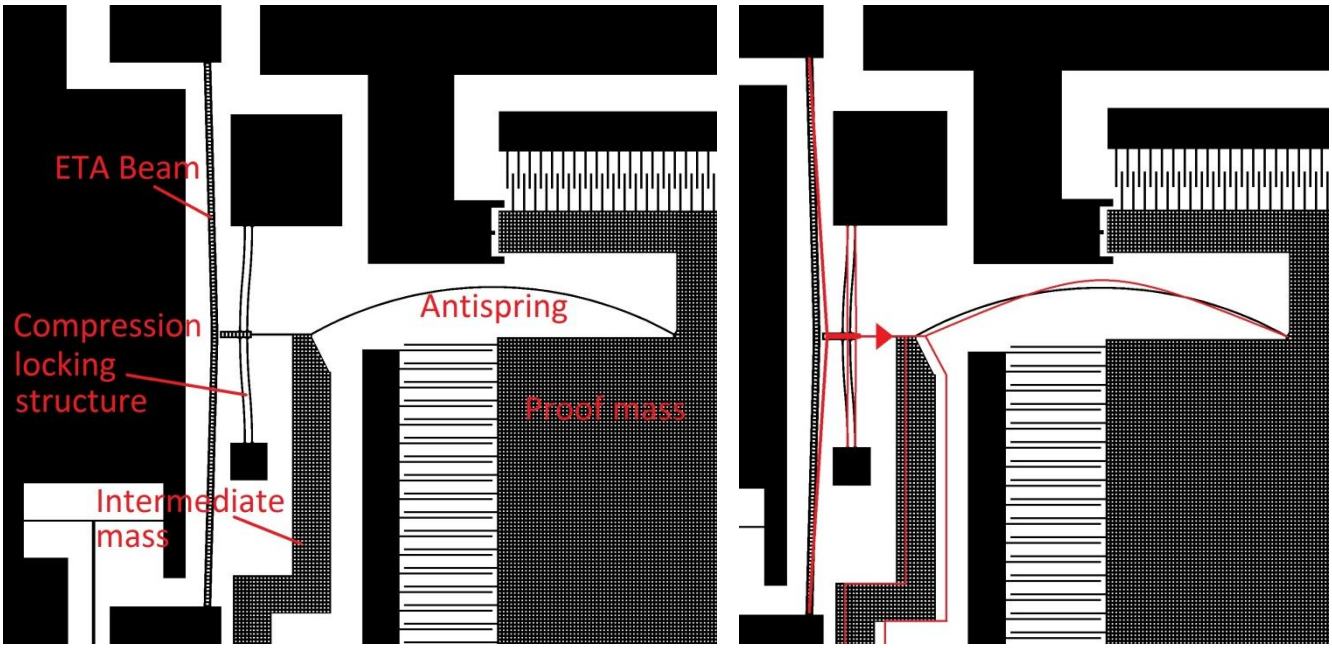

Figure 31: a) Zoom-in of left top corner of the MEMS G2 design schematic. B) Structure displacement in case of compression shown in red, initial structure shown in black.

The three anti-spring designs differ in ways of regulating and locking compression by using different intermediate structures, see Figure 32. The G1 design includes anti-reverse ratchets for compression locking. The G2 and G3 designs include double guiding and single guiding springs respectively. The G3 double guiding springs form a bi-stable beam which locks compression when the beam is pushed over its tipping point. The tipping point is reached at 10 µm compression. Note the 5 µm between ETA beam and compression locking structure. When talking about compression, compression of the anti-spring is meant, not the displacement of the ETA beam (which is 5 µm larger than compression).

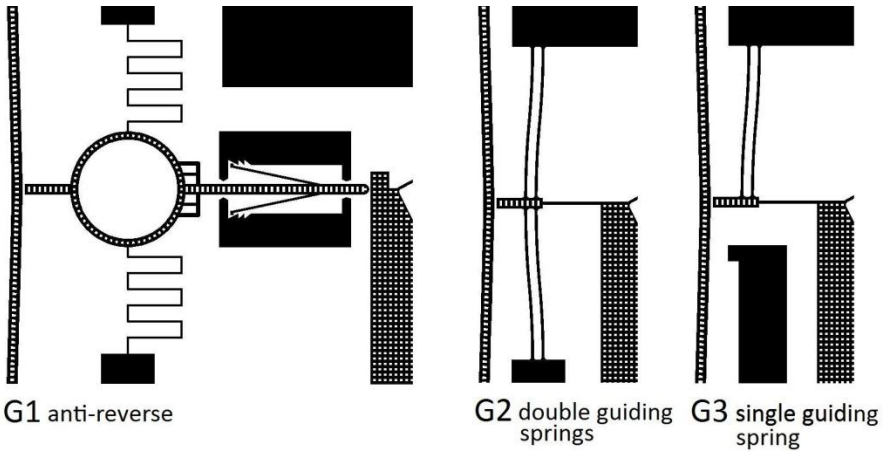

Figure 32: GAS MEMS types, G1-3: Anti-reverse, bi-stable beam and single guiding spring.

The G3 design is made with measurement applications in mind. The springs can be compressed, but also relaxed again, for the whole actuation range of the ETA beams. The locked compression designs (G1 and G2) are more focused on a final production stage.

The MEMS proof mass is designed to move in y-direction over a range of 8 µm upward and 8 µm downward, restrained by so called stops in the anchor structure, see Figure 33. The anchor stops prevents the capacitance fingers of actuator and sensing combs to stick together by Van der Waals bonding of the flat finger surfaces. Capacitance plate distance is 10 µm, thus leaving a margin of 2 µm. Also x-direction and rotation movement are restrained by anchor stop tips at a distance of 10 µm. All anchor stop surfaces have minimal surface area to prevent sticking by Van der Waals bonding.

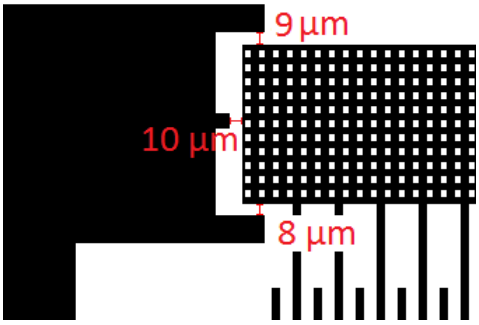

Figure 33: MEMS anchor stops restrains proof mass moving range, preventing the capacitance fingers to stick together. The difference in 9 µm and 8 µm spacing is caused by a design mistake.

The G1 design is pictured by electron microscope in Figure 34a and b.

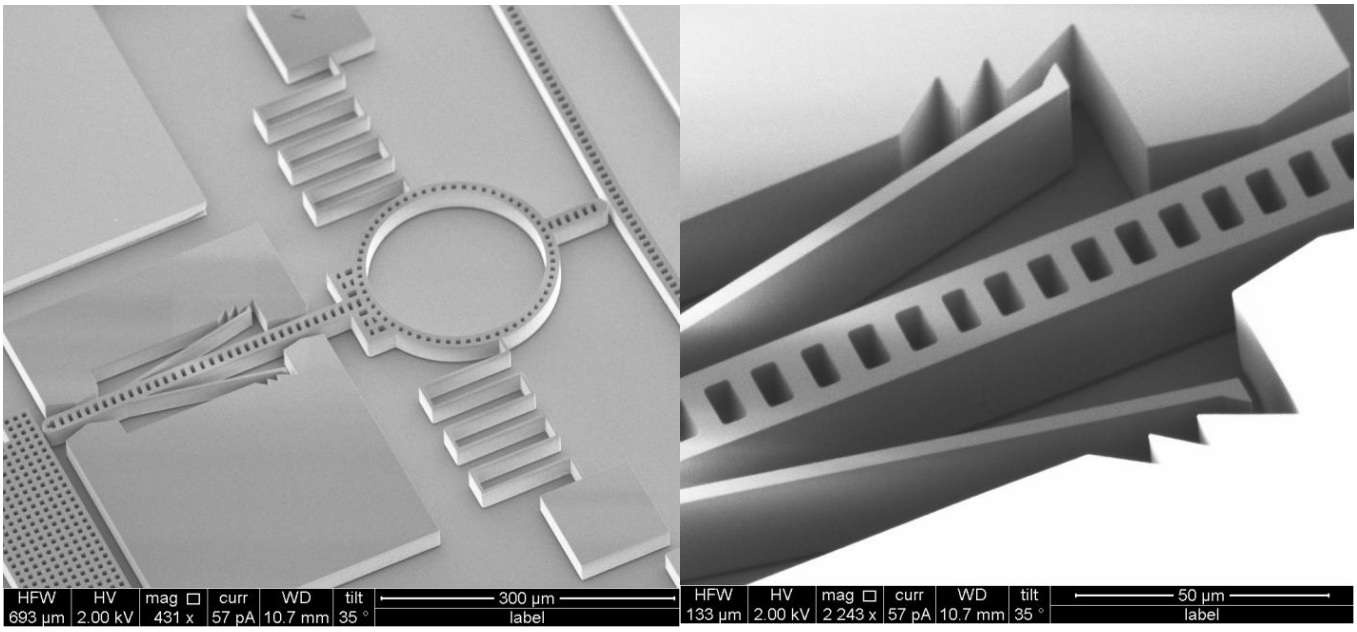

Figure 34: a) G1 MEMS anti-reverse structure, by electron microscope imaging. b) Close-up of the ratchet structure.

Locking the anti-reverse structure in its first notch requires a compression of 15 µm, the second notch requires another 10 µm of compression. The anti-reverse structure can also be enabled manually, using a small needle (for example the bonding needle of the bonding machine) in a ring with a radius of 185 µm, see Figure 34a. More observation pictures of the three anti-spring designs by microscope are shown in Appendix 7.9.

As treated in section 2.4.2, a spring constant k_s is defined for FEM modeling of the counter force of the intermediate structure during compression. The total spring constant k_{tot} is defined as the spring constant of intermediate structure k_s and anti-spring k_x in parallel:

$$k_{tot} = k_s + k_x \,. \tag{37}$$

For predicting the value of k_s, for the different intermediate structures, FEM Msc Marc is used.

For the G1 design FEM results in a constant intermediate structure spring constant of $k_s = 20{,}1$ N/m. This gives $k_{tot} = 20{,}1 + 19{,}3 = 39{,}4$ N/m. The initial and compressed structure state are shown in Figure 35.

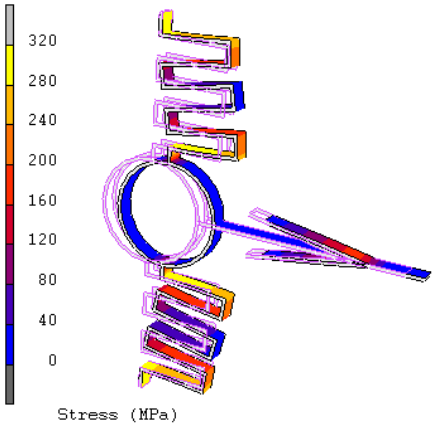

Figure 35: FEM Msc Marc G1 anti-reverse structure used for force versus displacement modeling. Initial and deformed state.

The G2 design FEM model result is shown in Figure 36.

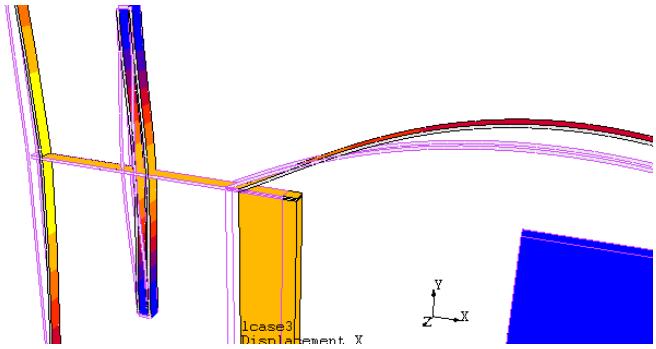

Figure 36: Msc Marc G2 bi-stable structure for force versus displacement modeling. Initial and deformed state.

The spring constant k_s for the G2 bi-stable structure is non-linear versus displacement, therefore the average spring constant $\bar{k}_s$ is used for load modeling. The average spring stiffness is defined as:

$$\bar{k}_s = \int_0^x \frac{dk_s}{dx}\,dx = \frac{F_x}{x} \tag{38}$$

The spring stiffness lowers initially when the bi-stable beam gets pushed towards its tilt point. The spring stiffness is lowest at the tilt point. The average spring stiffness $\bar{k}_s$ for the G2 bi-stable intermediate structure is plotted versus compression in Figure 37.

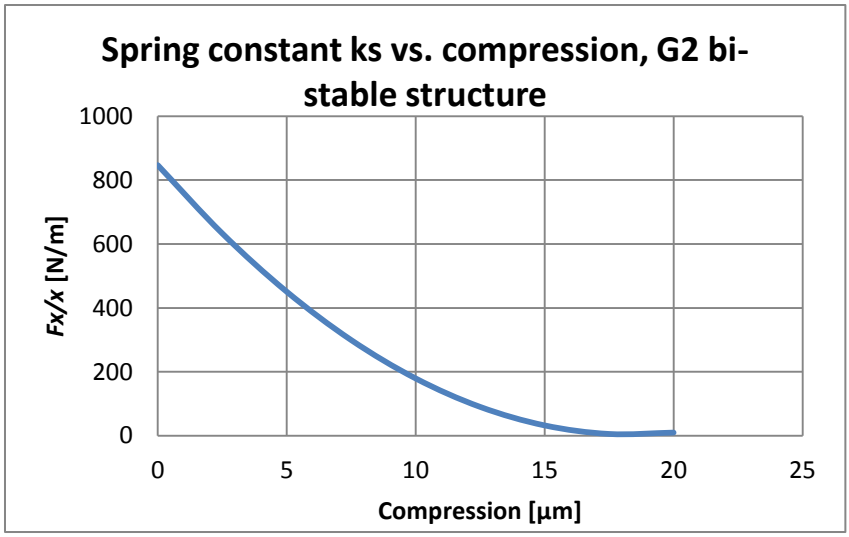

Figure 37: spring constant $\bar{k}_s$ of the G2 bi-stable beam structure versus compression.

Resulting in average $\bar{k}_s = 283\ \mathrm{N/m}$. This gives average $\bar{k}_{tot} = 283 + 19{,}3 = 302\ \mathrm{N/m}$. Comparing total spring constant values of the G1 ($k_{tot} = 39{,}4\ \mathrm{N/m}$) and G2 (average $\bar{k}_{tot} = 302\ \mathrm{N/m}$) predicts that the G2 structure requires substantially more force from the ETA beam to be compressed. Consequently it is expected that the G1 structure is further compressible using the ETA beams.

Analogous FEM modeling of the G3 intermediate structure results in a spring constant of $k_s = 46{,}4\ \mathrm{N/m}$. This gives $k_{tot} = 46{,}4 + 19{,}3 = 65{,}7\ \mathrm{N/m}$.

FEM Abaqus simulation of ETA beam actuation, combined with the external spring force with spring constant k_{tot}, predicts the maximum amount of compression per MEMS design, taking into account ETA beam limitations by maximum temperature. The tip displacement versus current is plotted in Figure 38 for G1, G2 and G3 MEMS structures.

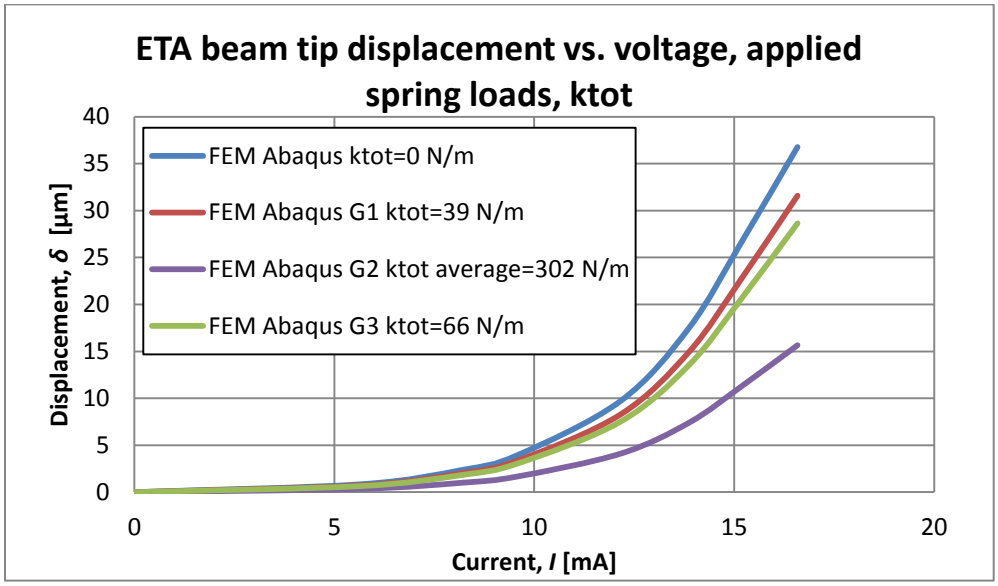

Figure 38: FEM Abaqus modeled ETA beam tip displacement versus current for MEMS design G1-3 intermediate structure + anti-spring loads. Loads are modeled as spring loads with spring constant k_{tot}.

3.1.2 Inverted pendulum design

Besides the anti-spring MEMS design there is also a fourth design, based on the inverted pendulum principal. See Figure 39.

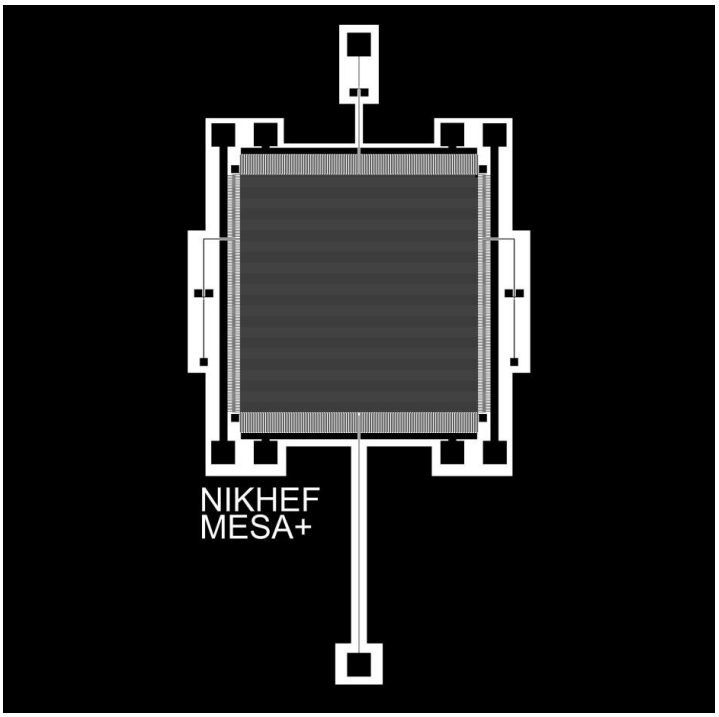

Figure 39: Inverted pendulum design schematic.

This design is supposed to be used vertical, so the mass is placed above the long beam spring. Mass actuation and displacement sensing uses the same comb actuator and sensing design as used on the anti-spring MEMS. Although now sensing fingers reside on the top and bottom of the mass, and actuating fingers on the left and right. This is because the mass now moves in the x-direction as seen in Figure 39.

The IP MEMS is initially locked rigid to the substrate by three connection points, see Figure 41. This prevents the mass from falling and, consequently sticking to the frame or the substrate, because of the long loose beam spring. When placed in upright measurement position the connection points are melted by applying a current, disengaging the proof mass. See Figure 40 for a close-up of a melting point. Because of the narrowing of the beam at the melting point, maximum temperature will be build up at this point, melting the small connection. Melting points C1 and C2 are hourglass shaped with 10 μm bases and a 3 μm bottle neck. The height of the hourglass shape is 21 μm. Melting point C3 differs is an analogous hourglass shape, only having bases of 5 μm.

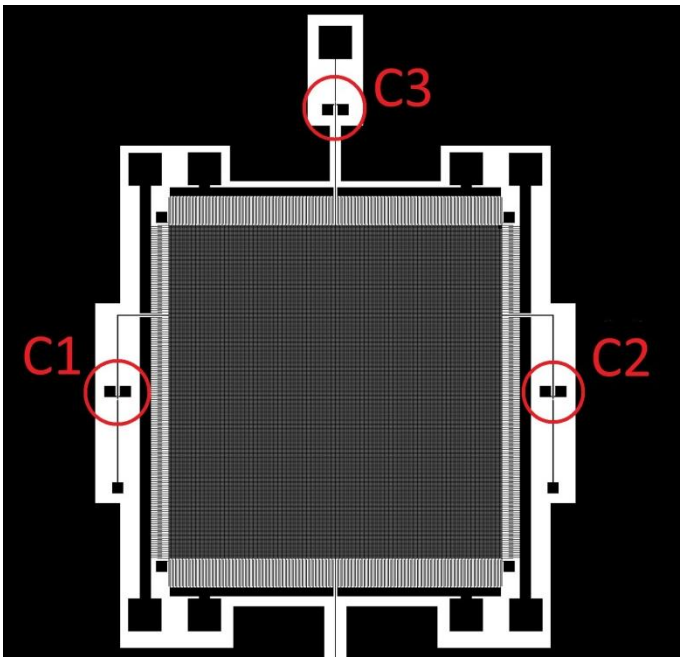

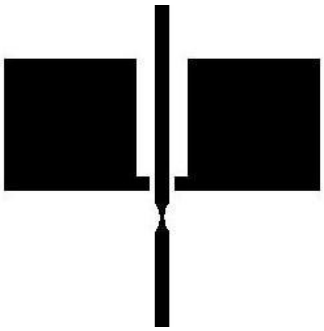

Figure 40: IP MEMS C1/C2 melting point close-up

Figure 41: IP MEMS connection points, numbered C1-3.

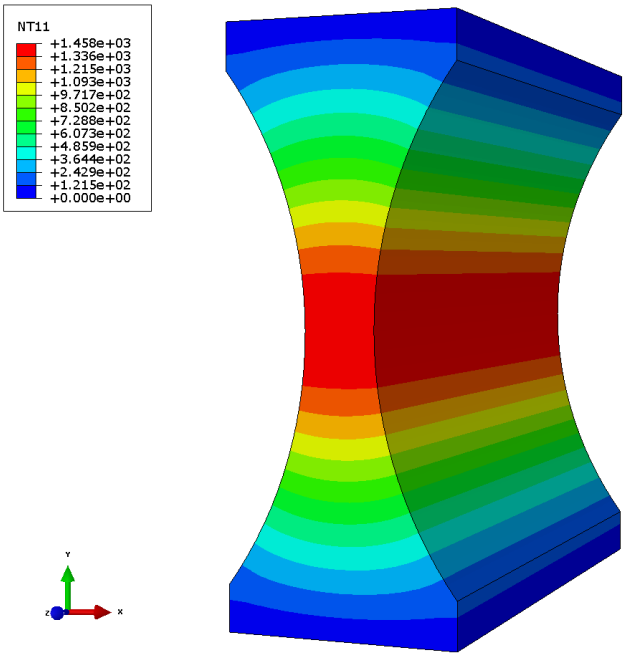

Figure 42: IP MEMS C1/C2 connection point temperature profile in FEM Abaqus. Maximum temperature at the smallest beam width reaches $T = 1700$ K. The connection point is expected to be melted at this temperature.

FEM simulation (Figure 42) predicts melting of the C1 and C2 connection points at a current in the order of 2 mA. For the C3 connection point, a lower current is expected, because the bases of 5 µm will transfer less heat.

3.2 Etching

The used accelerometers are etched out of silicon wafers, in one piece. Etching is performed by MESA+ (Institute for Nanotechnology). The initial wafer consists of a silicon substrate/handle wafer, a 2 µm layer of silicon oxide and a device layer of 25 µm on top, see Figure 44. All structures on the chip are etched of the 25 µm silicon device layer. The 2 µm silicon oxide layer beneath is etched away underneath parts whose are designed to move. All moving parts are perforated by 5x5 µm holes (Figure 43), so the etching fluid can remove all silicon oxide below. All non-perforated, parts contain an intact silicon oxide layer, which makes these parts rigid to the substrate.

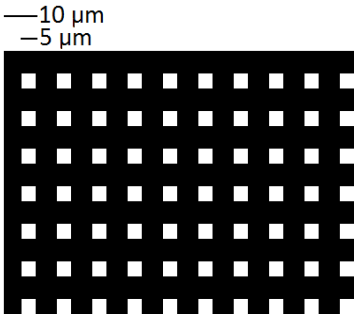

Figure 43: Perforated part of proof mass, etching design schematic.

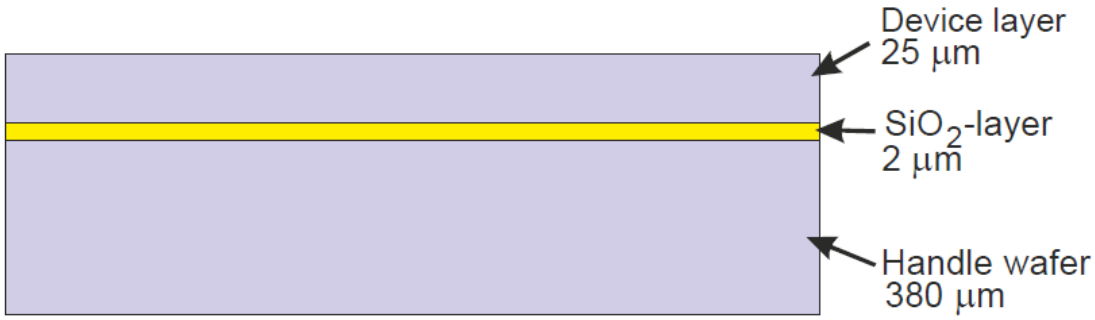

Figure 44: Silicon on insulator wafer, schematic [6].

When parts are thicker than ~5 µm, the silicon oxide layer is unreachable for the etching chemicals, which makes that part rigid to the substrate.

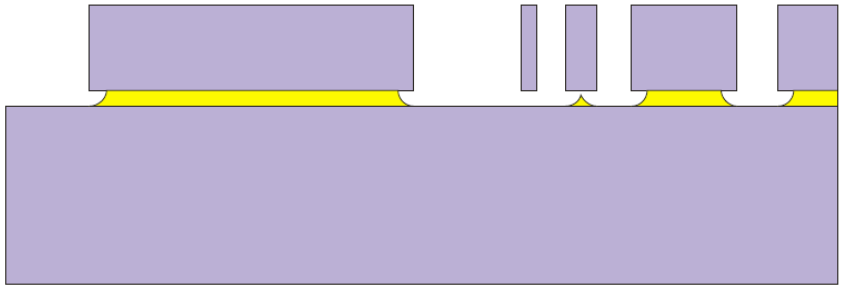

Figure 45: Detaching device layer from substrate by etching the silicon oxide layer, schematic [6].

Beams of 10 µm, without perforation, in the IP MEMS moveable structure resulted in the mass being stuck and the MEMS mass being rigid.

Electron microscope imaging shows micron sized defects in the walls of the structure, see Figure 46a. Furthermore large sideways etching defects are observed in some walls, as shown in Figure 46b .

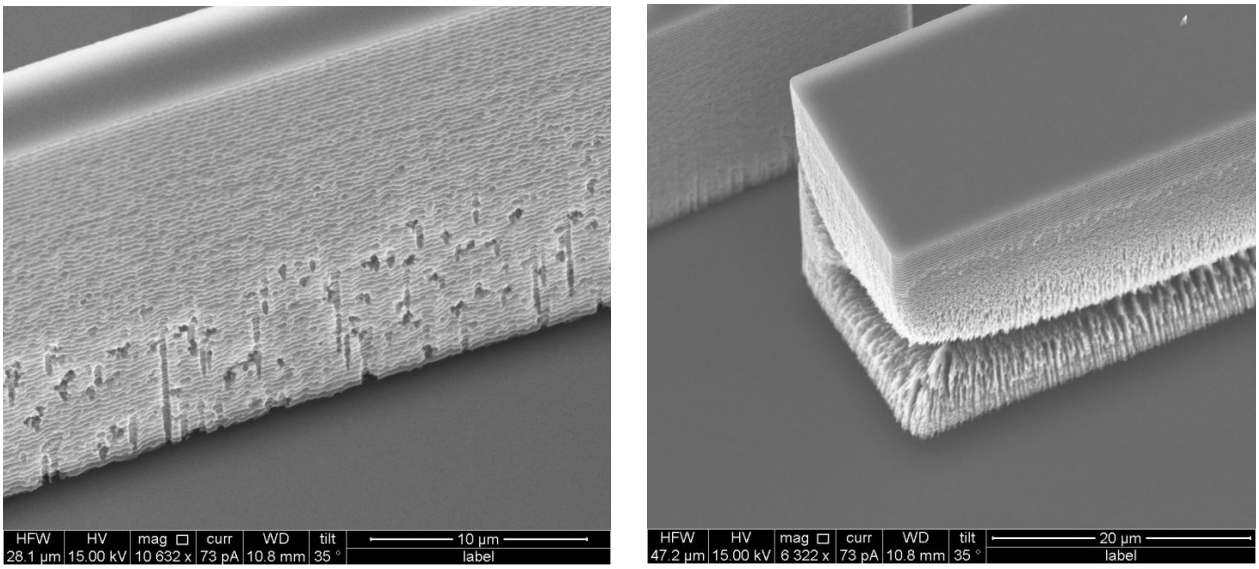

Figure 46: a) Micron sized defects in the walls of the device layer structure, imaged by electron microscope. b) Deep sideway etching defects, imaged by electron microscope.

These defects are predicted to influence structure strength and also reduce the mass of the proof mass. Besides that, such defects in the walls of the capacitance fingers will reduce comb capacitance and consequently lower actuation and sensing levels. Although, it is found that large defects are rare and it is expected overall consequences of small defects are negligible.

For the circular springs, cracks are observed in the top surface of the device layer, caused by bending of the beam, for example compression, see Figure 47. These cracks are expected to be present in the full 25 µm height of device layer, reducing beam strength and the spring constant in y-direction k_y.

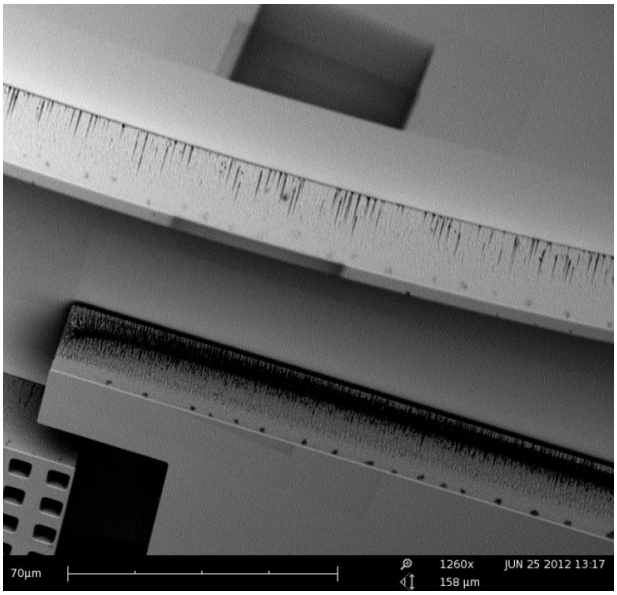

Figure 47: Cracks in the springs surface, caused by spring bending, imaged by electron microscope.

3.3 Bonding

The MEMS chips are placed in a chip carrier and bondings are made from chip carrier connections to probe points on the chip. The used chip carriers are from Kyocera, type C-QFJ (drawing number: PB-F87049), technical data: [7]. These square carriers consist of 44 connections, divided over 11 connections per side. Dimensions of the carrier are shown in Figure 48a (Image proportions don't correspond to the used carrier type).

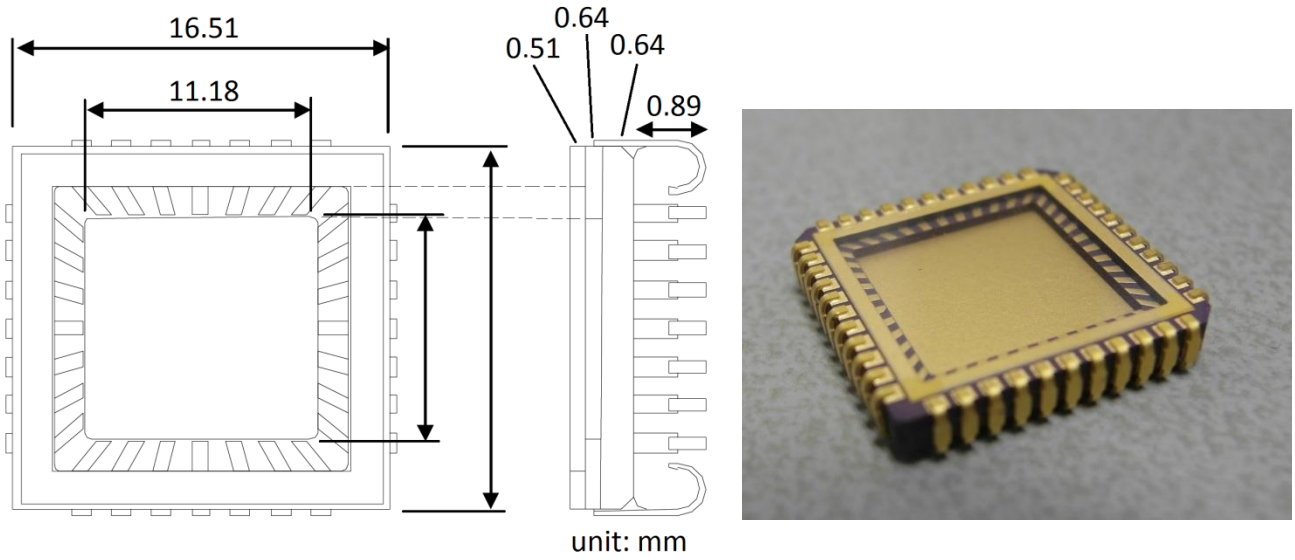

Figure 48: a) Chip carrier dimensions sketch [7]. b) Photo of the used chip carrier.

Bondings are made with 25 µm aluminum wires, using a Mech-EL/MEI 907 wedge bonder [8]. 25 gf static force and subsonic wringing-in of 60 kHz is applied to merge the wire on a silicon pad. The bonded wires have a width of ~70 µm and a height of 5-8 µm. See Figure 49.

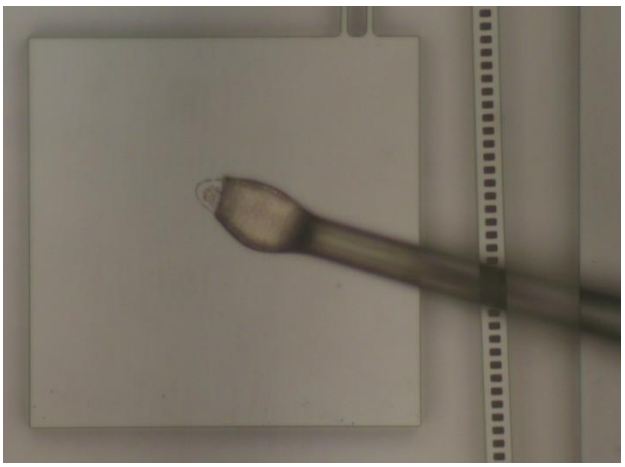

Figure 49: Aluminum wire tip bonded on silicon device layer surface. 200x microscope magnification.

The wire bonding lay-out for the anti-spring and IP design are found in Appendix 7.8, Figure 74 and Figure 75 respectively.

3.4 Microscope

A microscope is used for observing the MEMS chip, equipped with a 2,5x, 5x, 20x and 50x objective. Microscope objective details are shown in Table 1. The microscope is equipped with a 10x ocular which multiplies all objective magnifications by a factor ten. The 2,5x and 5x objectives are used for overview of the MEMS The 20x objective for detailed observation and distance measurements, see Figure 50. Measuring distances using this maximal microscope magnification (200x) is limited by a distinction uncertainty of ±1 µm. The microscope scale division for this magnification is 5 µm, which makes a distance of 5 µm more accurate to observe, having an uncertainty of ±0,5 µm. The working distance of the 20x objective is 2,2 mm, so the objective can come close enough to observe the chip surface.

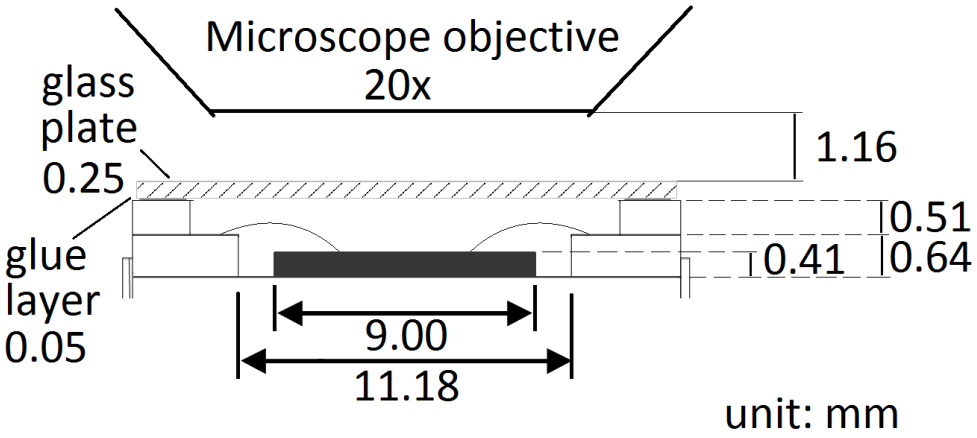

Figure 50: 20x objective situation sketch, working distance objective: 2,2 mm.

The working distance of the 50x objective is too short to focus on the chip surface. The working distance of the 50x objective is 0,6 mm, while 1,04 mm is the absolute minimum as seen in Figure 50. Using the 50x objective would result in a 2,5 times more accurate displacement observation, and thus a measurement resolution by eye of about ±0,4 µm. Using the 50x objective could be made possible by raising the chip in the carrier, keeping in mind the bonding arc height.

Table 1: Microscope objective details. [9]

Name	Zeiss EC Epiplan-Neofluar® HD Objective 20x	Zeiss EC Epiplan-Neofluar® HD Objective 50x
Magnification	20X	50X
Numerical Aperture NA	0.5	0.8
Working Distance (mm)	2.2	0.6
Focal Length FL (mm)	8.23	3.29
Resolving Power (µm)	0.55	0.34
Depth of Focus (µm)	1.1	0.43
Field of View, 25 Diameter Field Eyepiece (mm)	1.25	0.4
Parfocal Length (mm)	45	45

3.5 Electronics chip board

An electronics chip board was used for measuring the MEMS chips, mainly for measuring the sensing comb signal. Photos of the in-vacuum and out-vacuum chip boards are found in Appendix 7.9, Figure 77 and Figure 78. The MEMS chip carrier is soldered on the in-vacuum chip board. Connections spacing is designed identical for the chip board and the chip carrier.

The board is connected to a +15, -15 V dual voltage source. This source limits the maximum output voltage to 15 V. The inside vacuum board can be placed in the vacuum chamber. The main board and in-vacuum board will then be connected by two 37-pins flat cables and a feed-through in the vacuum chamber wall. The electronics board actuating and sensing circuit is shown simplified in Figure 51.

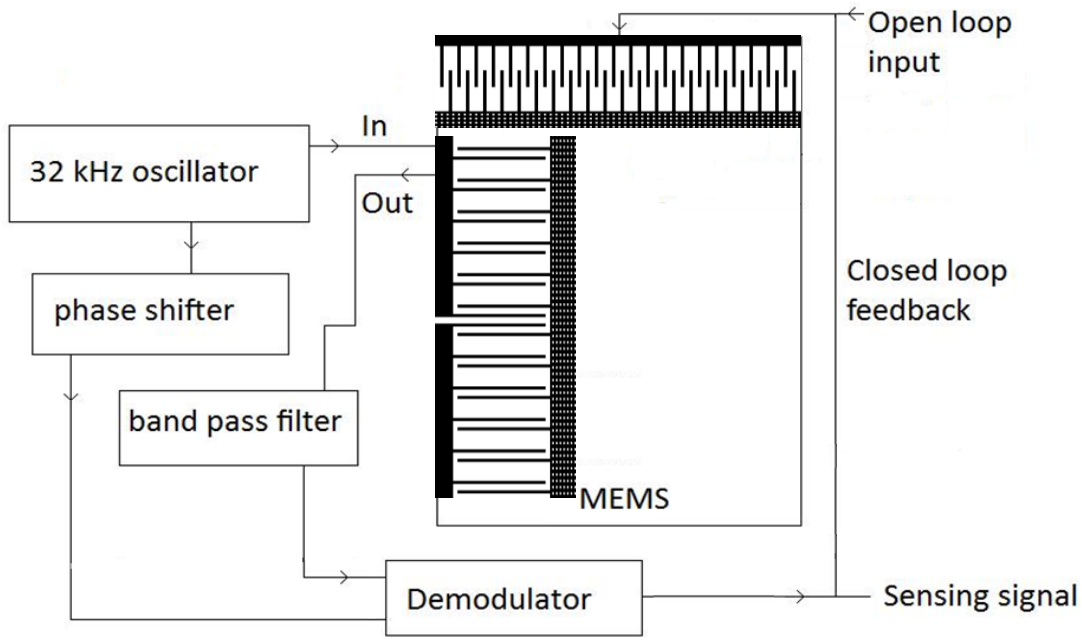

Figure 51: Electronic actuating and sensing circuit, simplified schematic.

A 32 kHz is applied to the sensing combs. When the mass moves, a displacement signal is summed up to the 32 kHz signal, in the order of $1 \cdot 10^2$ Hz. The mass won't move because of the 32 kHz signal, because of the high frequency of the signal, applying almost no force on the comb. Furthermore the sensing combs compensate each other, because of the mirrored top and bottom part design. The 32 kHz signal gets phase shifted to be in phase with the summed up signal. Then the summed up signal gets filtered from the high frequency signal by a demodulator. The low frequency motion signal is the sensing output of the demodulator. It is also possible to feedback the output signal to compensate proof mass movement using the actuator combs. The final operating principle of the MEMS accelerometer is measuring the acceleration force by keeping the mass steady, compensating displacement with an actuator signal, which is the acceleration output signal.

3.6 MEMS evacuation

Air damping is dependent on pressure. Lowering pressure raises the mean free path of the air molecules, lowering air damping.

$$l = \frac{k_B T}{\sqrt{2}\pi d^2 p}, \tag{39}$$

where:
$l =$ Mean free path [m]
$k_B =$ Boltzmann constant [JK^{-1}]
$T =$ Temperature [K]
$d =$ Diameter of the gas particles [m]
$p =$ Pressure [Pa] .

Calculating the mean free path vs. pressure, using $T = 293$ K, $d = 3 \cdot 10^{-10}$m, results in Figure 52 below.

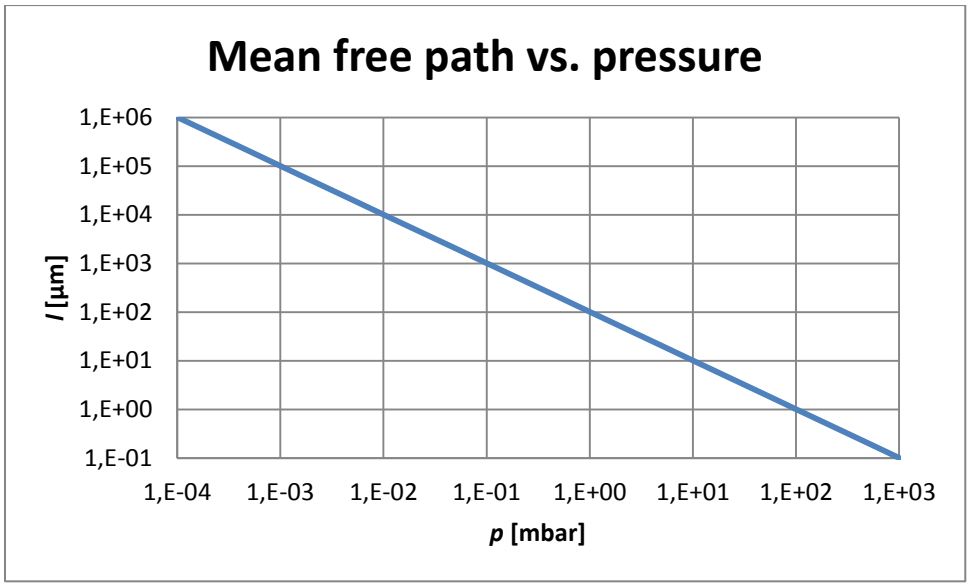

Figure 52: Mean free path of air molecules ($d = 3 \cdot 10^{-10}$m) versus pressure.

This graph shows that at a pressure of $p = 5 \cdot 10^{1}$ mbar the free mean path is reduced to $l = 2$ µm, corresponding to the distance between device layer and substrate, which is the smallest distance between surfaces present in the MEMS. This means that air film damping is suspected to drop from this pressure and lower. Because air film damping is calculated as the dominant damping component (see section 2.6), also the Q-value is suspected to drop from this pressure and lower. At a pressure of $p = 5 \cdot 10^{-2}$ mbar the mean free path reaches $l = 2$ mm, corresponding to the largest dimensions of the MEMS (approximately the mass length). At this pressure the air film damping is suspected to be negligible.

The used vacuum chamber is shown below in Figure 53.

Figure 53: Vacuum chamber set-up. Evacuation by scroll pump and second stage turbomolecular pump.

3.6.1 Evacuation speed

It is necessary to consider evacuation speed during MEMS evacuation. Because the chip carrier is covered with a protective glass, only small gaps are open for air flow. Evacuation of the vacuum chamber creates a pressure difference under (inside chip carrier) and above the glass. The amount of pressure difference is dependent on evacuation speed. A too high pressure difference could break the glass. In case of evacuation, pressure under the glass will be higher than above, causing the glass to expand outwards the chip carrier. This expansion widens the air flow gap, which creates more allowance of the evacuation speed. In case of venting the glass will cave inwards the chip carrier. Furthermore the air flow gap narrows, reducing the maximal allowed venting speed.

The general equation for air gap flow is given by:

$$\rho \frac{dv}{dt} = -\nabla p + \mu_{air} \nabla^2 v \,. \tag{40}$$

Because $\rho \frac{dv}{dt} = 0$ and the flow is only in the x-direction:

$$\frac{dp}{dx} = \mu_{air} \frac{d^2 v}{dy^2} \tag{41}$$

Resulting in a global evacuation speed limit of 5 mbar/s and a venting speed limit of 50 mbar/s.

4 Measurement results

Measurements were done with proof-of-principle goals in mind. At First a G3 type MEMS is tested (without electronics board) on correct operation of all components, e.g. mass movement, comb actuation and compression by ETA beams. A picture of the G3a MEMS is found in Appendix 7.9, Figure 79. The G3 design, including single guiding springs, was prepared for actuation and compression measurements by microscope observation. Mechanical and bonding connections were checked by measuring electrical resistance. A function generator is used for direct actuation of the proof mass. Only a single actuating comb was used for static displacement measurements and oscillation measurements. Furthermore DC and AC measurements with one comb are repeated for different amounts of spring compression. Melting of an ETA beam restricted compression possibilities to two of four beams.

Completion of the electronics chip board enabled new measurement possibilities. All MEMS design types were bonded on chip carriers, which were soldered on small in-vacuum chip boards. The G2 design was used for evacuation testing and in-vacuum measurements, namely measuring relaxation time versus pressure. A second G3 design is used for resonance frequency measurements under four spring compression.

Side measurements done include G1 anti-reverse compression and G2 bi-stable beam compression. The IP MEMS chip was tested on disengaging the proof mass by performing connection point melting.

A summary of all MEMS chips prepared and measured is shown in Table 2. All prepared MEMS after G2a show small or large defects, probably because of contamination of the MEMS in storage, or by unwanted remains of the silicon oxide layer during etching.

Table 2: MEMS used and measured, chronological order.

MEMS name	MEMS type	Medium	State	Comments
G3a	G3	bread board	one ETA beam melted	first measurements
G2a	G2	chip board	all working	vacuum measurements
G1	G1	chip board	proof mass stuck (stick slip)	no compression possible
IP	IP	chip board	proof mass against stops	Only melting connection point tests
G2b	G2	chip board	incorrect bonding	not used yet
G3b	G3	chip board	proof mass stuck (stick slip)	offset in sensing output, only working upside down

4.1 Capacitive actuating and sensing

Actuation combs are tested on proof mass displacement capability. A voltage is applied over one comb row, measuring displacement in the y-direction. Also an AC voltage is applied over one comb row, measuring proof mass oscillation amplitude in resonance. Combination of DC and AC measurements result in the Q-value of the MEMS accelerometer measured, which is the ratio of static amplitude and amplitude in resonance as seen in section 2.1.1, Eq. (6). The sensing combs output signal is calibrated for static force. Calibration of output signal versus proof mass displacement is not achieved, because of microscope observation uncertainty.

4.1.1 Capacitive actuating

The comb actuation fingers are tested on delivering pulling force on the proof mass by applying a voltage over one actuator comb. Displacement of the proof mass is observed by 200x microscope magnification. Measuring distances are uncertain by ±1 µm in case of this magnification, down to ±0,5 µm uncertainty for measuring distances of 5 µm, as treated in section 3.4. Figure 54 shows the calculated displacement Δy versus applied voltage U_A (using section 2.5.1, Eqs. (28) and (29)) for different values of capacitance geometry factor C_C, together with measured displacement by microscope.

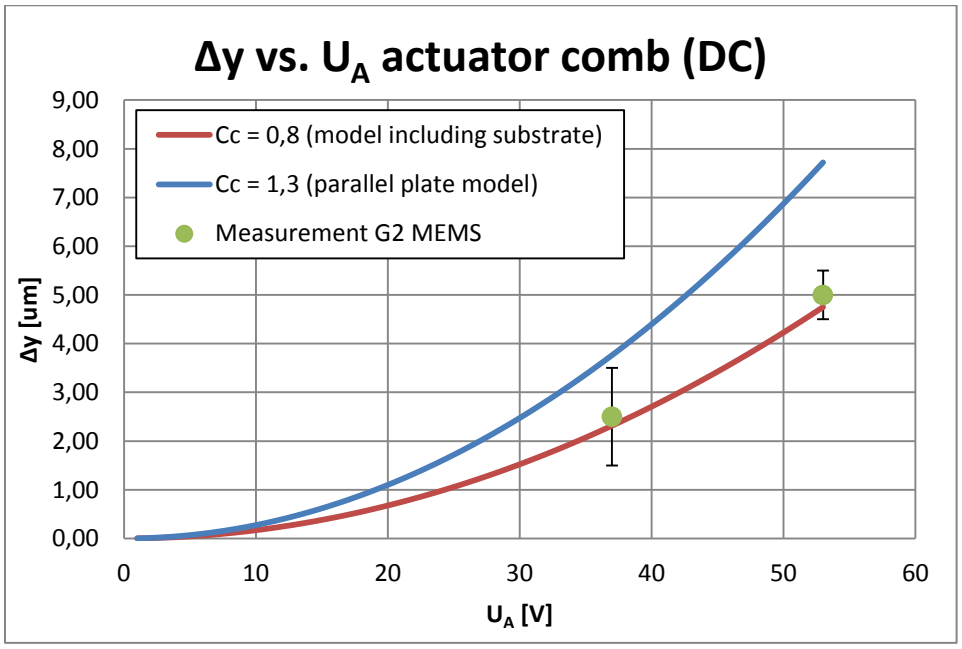

Figure 54: modeled displacement of proof mass displacement *Δy* for different voltage U_A applied over one actuator comb row. Measured value of microscope measurement of the G2a MEMS.

The relation between Δy and U_A is quadratic, according to Eq. (28). Measurements correspond to the model including substrate for the capacitance factor, which confirms the predicted $C_c = 0{,}8$ by FEM geometry simulations, treated in 2.5.3.

Actuation input voltage is calibrated versus static force by measuring the actuation comb voltage needed to compensate the proof mass weight. This is done by tilting the MEMS accelerometer by +90 or -90 degrees over the x-axis, exposing the proof mass to 1 g acceleration, corresponding to a force of $F = mg = 0{,}511 \cdot 10^{-6} \cdot 9{,}81 = 5{,}00$ µN. The voltage needed to bring the proof mass back

up in center position requires a voltage of $U_A = 50\pm1$ V. This results in $c_A = \frac{F}{U_A^2} = (2{,}0 \pm 0{,}1) \cdot 10^{-9}\ \mathrm{N/V^2}$. This relation between force F and U_A, corresponds with modeling for a capacitance geometry factor $C_c = 0{,}8$ as shown in section 2.5.1, Figure 23. According to the modeled curve for $C_c = 0{,}8$ in Figure 54 the proof mass displacement for 1 g load ($U_A = 50\pm1$ V) is $\Delta y = 4{,}2 \pm 0{,}2\ \mu\mathrm{m}$

In order to bring the proof mass in oscillation at frequency f, an AC voltage of frequency $f/2$ is applied to one comb side, resulting in a force:

$$F = c_A U_A^2 = c_A \left(U_{A0} \sin 2\pi \frac{f}{2} t\right)^2 = c_A {U_{A0}}^2 \frac{1}{2}(1 + \sin 2\pi f t) \tag{42}$$

Using one comb only results in an offset of the proof mass oscillation, which is ignored.

At constant AC amplitude, the resonance peak was determined by changing frequency and finding the maximum amplitude. A transformer was used to generate voltages of up to $2U_{A0} = 60$ V peak-peak, giving a resonance peak-peak displacement of $4{,}5 \pm 1\ \mu\mathrm{m}$ through the microscope. Thus the resonance amplitude is $\Delta y = 2{,}3 \pm 1\ \mu\mathrm{m}$, at $U_A = 30 \pm 1$ V. This result can be combined with the DC amplitude obtained in the previous paragraph, resulting in the Q value:

$$Q_{real} = \frac{\frac{A}{F}(\omega_{real})}{\frac{A}{F}(\omega = 0)} = \frac{2{,}3}{30^2} \Big/ \frac{4{,}2}{50^2} = 1{,}5 \pm 0{,}7$$

The damping factor corresponding to this Q-value is $D = (5{,}4 \pm 2) \cdot 10^{-4}\ \mathrm{N/m/s}$, using Eq. (6) from section 2.1.1.

Obtaining Q-value by measuring relaxation time is treated in section 4.4.

4.1.2 Capacitive sensing

Sensing output voltage is calibrated versus acceleration by tilting the MEMS accelerometer by +90 or -90 degrees over the x-axis, exposing the proof mass to 1 g acceleration. A voltage $U_S = 1{,}25 \pm 0{,}02\ V$ is measured for 1 g acceleration, resulting in $\frac{U_S}{a} = \frac{1{,}25\ V}{1\ g} = 0{,}13 V/(m/s^2)$, assuming a linear sensing output versus displacement, as modeled in section 2.5.2, Figure 26. This assumption can be made because of the sensing comb mirrored structure geometry, which cancels non-linear effects.

Calibration of sensing output voltage versus displacement is not achieved, because of the large microscope displacement measurement uncertainty of ±1µm.

4.2 Electro-thermal beams

ETA beams tip displacement is measured for an voltage applied over the beam, with corresponding current and beam resistance. Beam temperature can be calculated from beam resistance measurements. The relaxation time of the ETA beam is measured by applying a block voltage. The relaxation time is a measure for beam heating and cool down time.

4.2.1 Tip displacement measurements

ETA beam voltage and current are measured for tip displacement, using the G3a MEMS. Beam resistance per ETA beam at relaxed state (ambient temperature) was measured with a multimeter, connecting probes to the ETA- and ETA+ chip carrier connections. The measured resistance is shown in Table 3.

Table 3: Measured resistance per Electro-thermal beam (MEMS G3).

Resistance ±0,001 [kΩ]	Left	Right
Top	0,948	1,005
Bottom	0,952	0,977

Applying a current through the Electro-thermal actuators results in a temperature profile in the beam, as modeled in 2.4.1 (electro-thermal model). Direct measurement of the beam temperature is not possible. Although resistance is a measure for the beam temperature, see section 2.4.1, Eq. (19). In Figure 56 measured voltage versus applied current through the beam is shown. The resistance is calculated from this measurement, shown in Figure 56.

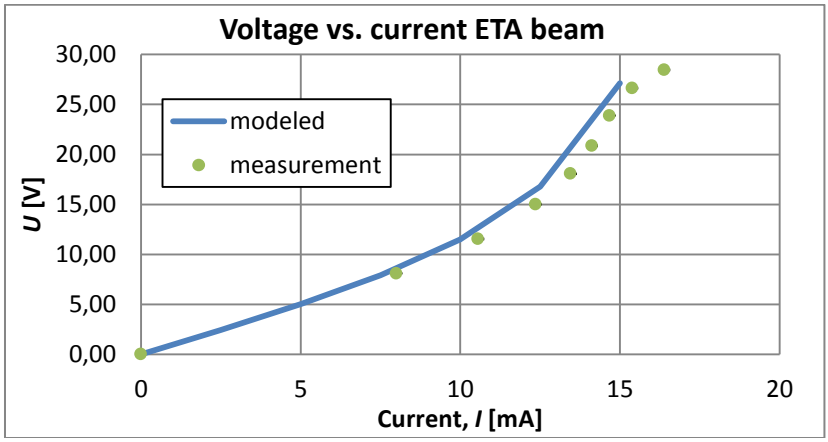

Figure 55: Voltage over beam versus current through beam, modeled and measured for G3a MEMS.

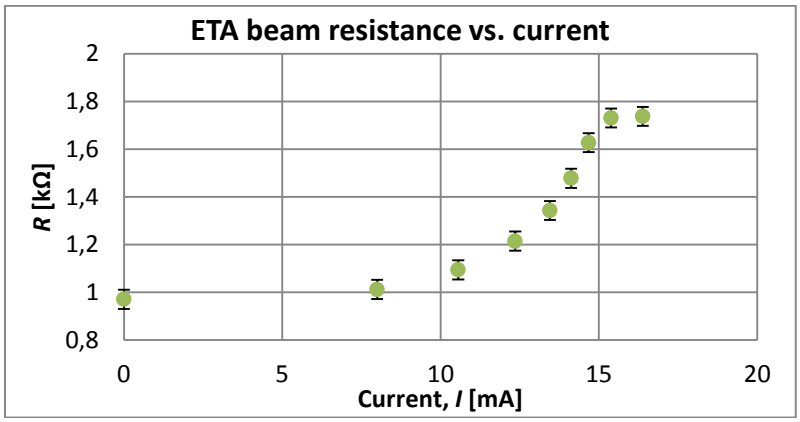

Figure 56: Measured ETA beam resistance versus applied current through the beam, for G3a MEMS.

By using Eq. (19) from section 2.4.1, the average beam temperature is calculated using the measured beam resistance, shown in Figure 57 below:

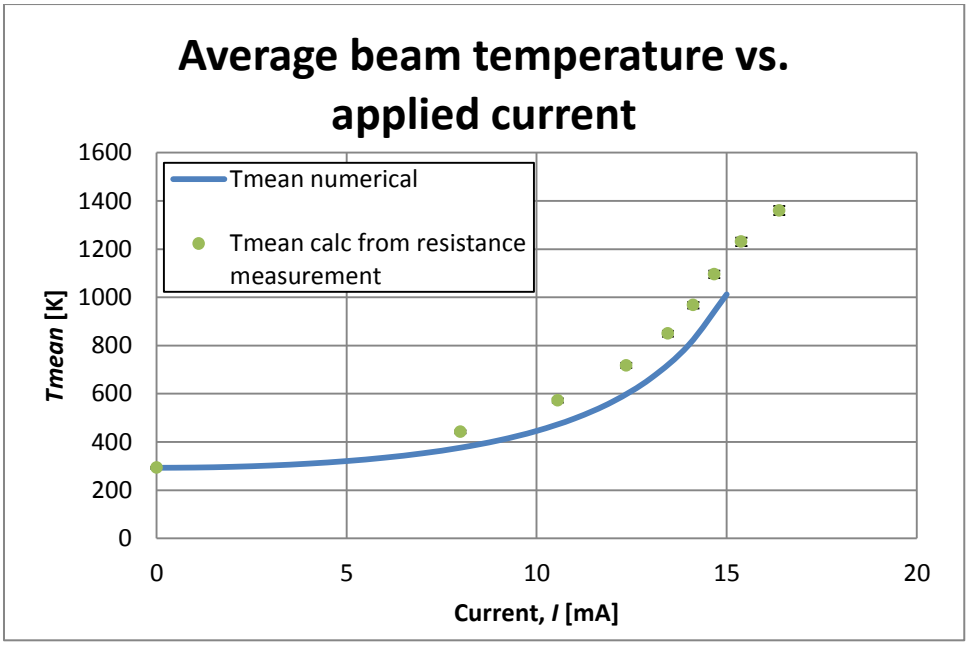

Figure 57: Average ETA beam temperature versus current applied, for numerical model and calculation from beam resistance measurements (G3a MEMS).

The increased temperature causes expansion of the beam. Because the beam ends are fixed between two rigid walls, this expansion causes displacement of the beams center tip towards the mass. Measurements of displacement versus current are done by observation through microscope, shown in Figure 58. The displacement could be roughly determined in steps of 2,5 μm. The accuracy of this observation is estimated to be 0,2 μm.

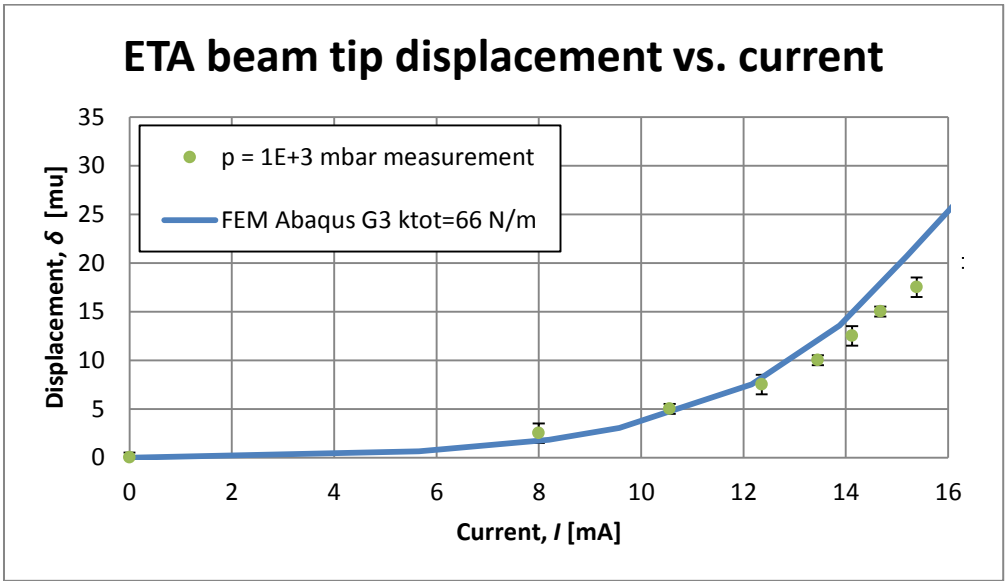

Figure 58: modeled and measured beam tip displacement versus current applied through the beam. Model also shows the tip displacement in case of evacuation to a pressure of $1 \cdot 10^{-2}$ mbar. Measurement for G3a MEMS.

A maximum tip displacement of 17,5 μm (meaning a spring compression of 12,5 μm) is measured for the G3a MEMS. FEM Abaqus modeling for the G3 intermediate structure spring load roughly corresponds to the measurement.

4.2.2 Relaxation time

When a step response current is applied through the beam, a relaxation time τ is needed to reach maximum temperature and stable tip displacement. Observation by microscope shows an instant time needed to reach this stable final equilibrium. Exact determination of τ is possible measuring voltage over the beam ($R(T)$ ETA $= 950\ \Omega$) and a resistor in series ($R_1 = 99{,}7\ \Omega$). The measuring circuit looks as follows.

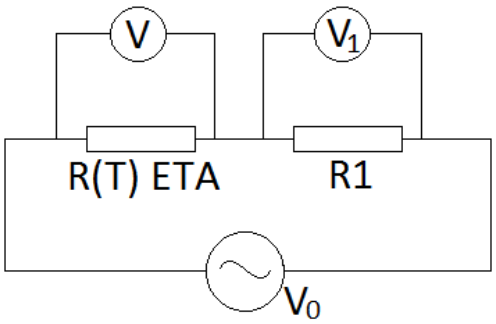

Figure 59: Circuit for ETA beam relaxation time measurement.

The ETA beam resistance is exponentially dependent on temperature multiplied by a linear scaling factor α. This linear factor is determined by measurement.

$$R(T) = R(293)\left(1 + \alpha\left(1 - e^{t/\tau}\right)\right), \tag{43}$$

where:
$R(T) =$ ETA beam resistance $[\Omega]$
$R(293) =$ ETA beam resistance for room temperature $[\Omega]$
$\alpha =$ Linear factor $[-]$
$\tau =$ Relaxation time $[s]$.

As seen in Figure 59, the measured voltages over the ETA beam and R_1 are given by:

$$U(T) = U_0\left(\frac{R(T)}{R(T) + R_1}\right) \tag{44}$$

$$U_1 = U_0\left(\frac{R_1}{R_1 + R(T)}\right) \tag{45}$$

Measurement results are $R(293) = 950\ \Omega$, $U_1(0) = 1{,}42$ V and $U_1(\infty) = 1{,}25$ V and thus $R(\infty) = 1093$. Fitting of Eq. (43) to the measurement of U_1 gives α =0,15 s, resulting in the relaxation behavior shown in Figure 60.

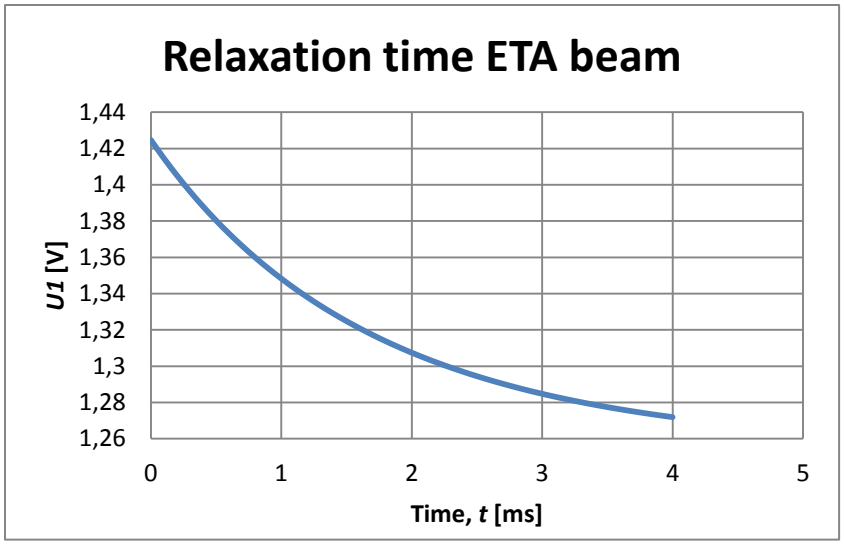

Figure 60: Relaxation ETA beam, modeled by fitting to measurement points of $U_1(0)$ and $U_1(\infty)$.

From this graph, the beam temperature heating and cool down times are estimated to be in the order of 5 ms.

4.3 Resonance frequency and the effect of spring compression

4.3.1 G3a MEMS, two spring compression measurements

Resonance frequency is measured through microscope for the G3a MEMS, with and without compression applied on the springs. Only 2 out of 4 springs are compressed, because of a melted electro-thermal beam of the G3a MEMS. The resonance frequency is determined at the point of maximum amplitude observed through microscope. The accuracy of this measurement method is determined to be ± 2 Hz.

The resonance frequency can also be calculated from DC measurements of the spring stiffness. DC measurements are done measuring the voltage applied over one actuator comb needed to displace the mass by 5 µm, versus compression. The measured voltage needed, gives the force needed by Eq. (28) of 2.5.1. This force gives the spring constant and thus the resonance frequency f_0 (without damping). f is calculated from f_0 using Eq. (5) of 2.1.1. The voltage U_A needed over one comb row for 5 µm displacement, versus compression is shown in Figure 61. Resonance frequency AC measurements and calculated out of DC measurements are shown in Figure 62.

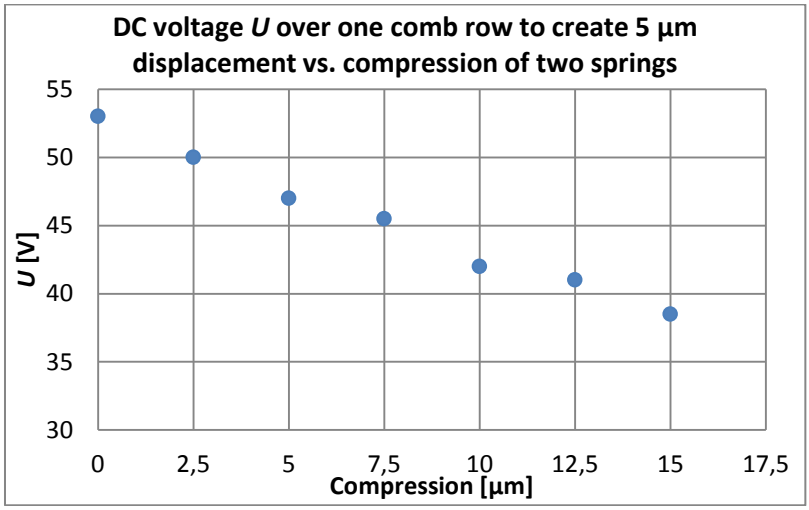

Figure 61: Measured voltage U_A needed over one comb row to create 5 µm displacement of the proof mass in y-direction, versus compression of two out of four springs. G3a MEMS.

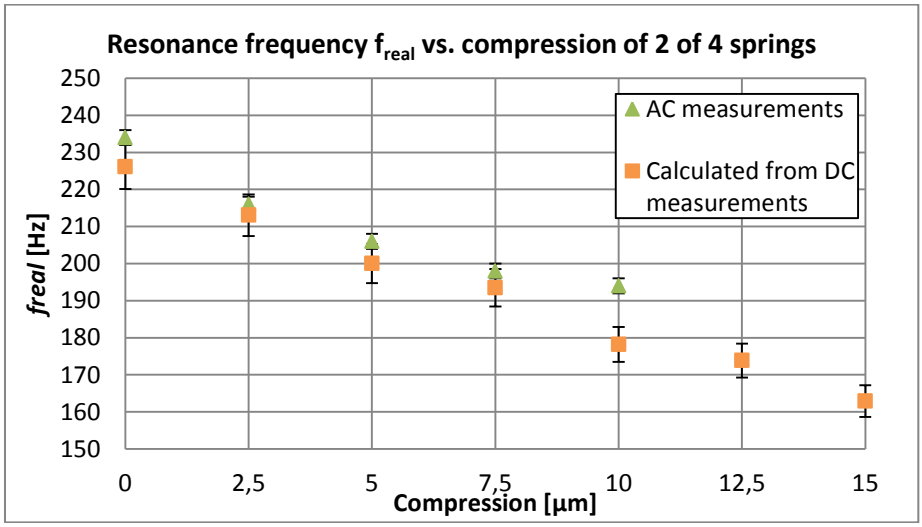

Figure 62: Resonance frequency versus compression of 2 out of 4 springs. AC measurements frequency is observed directly. DC measurements are used to calculate resonance frequency. G3a MEMS.

At zero compression the resonance frequency is measured $f_{real} = 234 \pm 2$ Hz. The DC measurement combined with calculation results in a lower resonance frequency of $f_{real} = 226 \pm 6$ Hz. The AC measurement curve shows decreasing inclination, suggesting flattening of the resonance frequency reduction versus compression. This is not expected. However the DC calculation suggests linear drop of the resonance frequency, even for compression higher than 10 µm. This is expected as seen in section 2.2, Figure 10. The DC measuring point of 15 µm, is very close to ETA beam melting and this spring compression is only measured once.

From the two spring compression measurements, results are extrapolated to the situation of four spring compression. Distinguish vertical spring constant k_0 for the uncompressed springs and vertical spring constant k_1 for the compressed springs. Now the total spring constant of the system is the sum of all four spring constants:

$$2k_0 + 2k_1 = m\omega_0^2 \,, \tag{46}$$

where k_1 and f_0 are dependent on compression u:

$$k_1(u) = k_0 - 2\pi^2 m f_0(u)^2 \,, \tag{47}$$

The resonance frequency without damping f_0 is calculated from f_{real} using:

$$f_0 = \sqrt{f_{real}^2 + \frac{1}{8}\left(\frac{D}{\pi m}\right)^2} \,, \tag{48}$$

by using Eq. (5), from section 2.1.1.
Results of extrapolation for resonance frequency f_0 and spring constant are shown in Figure 63 and Figure 64, combined with modeling results of f_0 and spring constant. The inclination of measured and modeled curves of f_0 versus compression have similar behavior, meaning the resonance frequency reduction by spring compression behaves as expected from modeling. The overall resonance frequency level differs between model and measurements, by approximately 70 Hz. This difference can be explained by beam modeling parameters varying from reality. For k_y, similar inclination correspondence and overall level difference is shown.

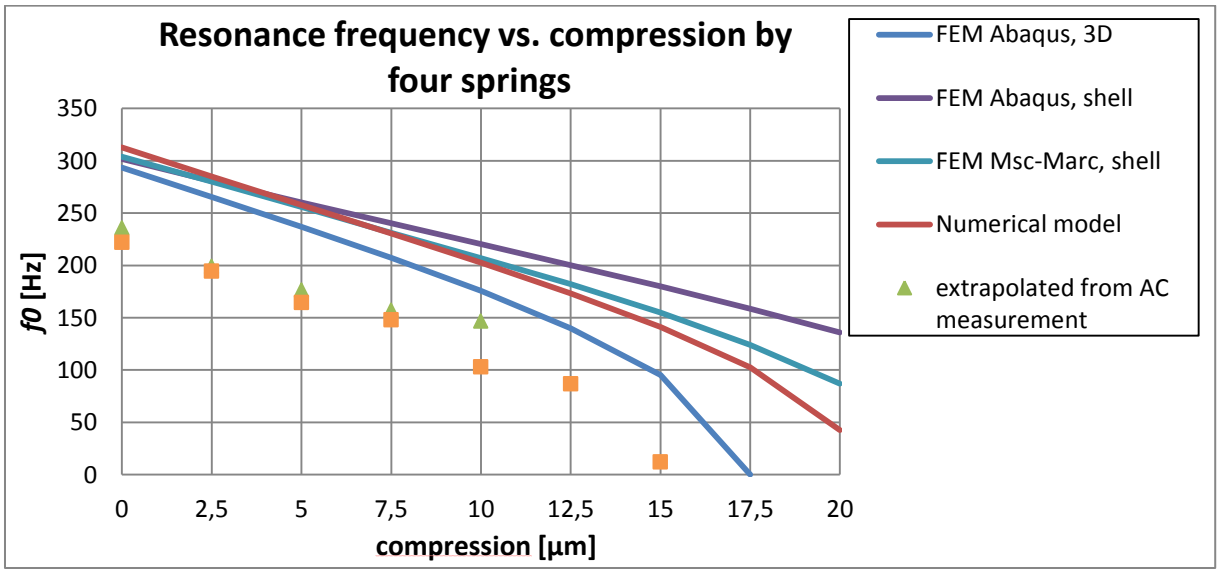

Figure 63: Extrapolated resonance frequency versus compression by four springs. Combined with modeled resonance frequency versus compression.

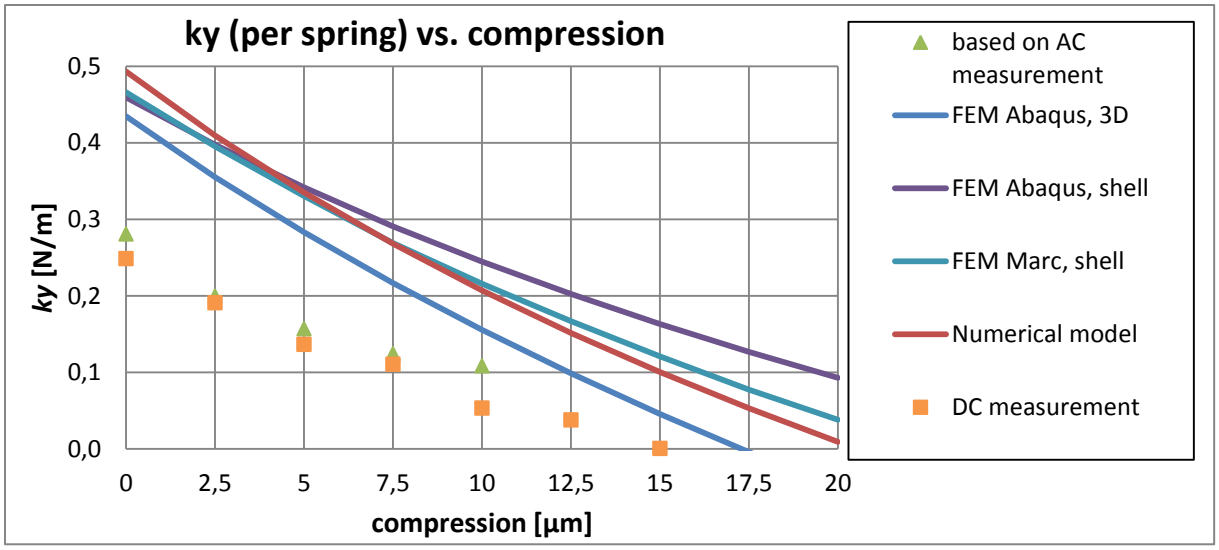

Figure 64: Extrapolated spring constant per spring versus compression by four springs. Combined with modeled spring constant versus compression.

4.3.2 G3b MEMS, four spring compression measurements

A second G3 type MEMS is prepared, for the G3a MEMS has one melted ETA beam. Four spring compression is measured using the G3b MEMS and results are shown in Figure 65 below.

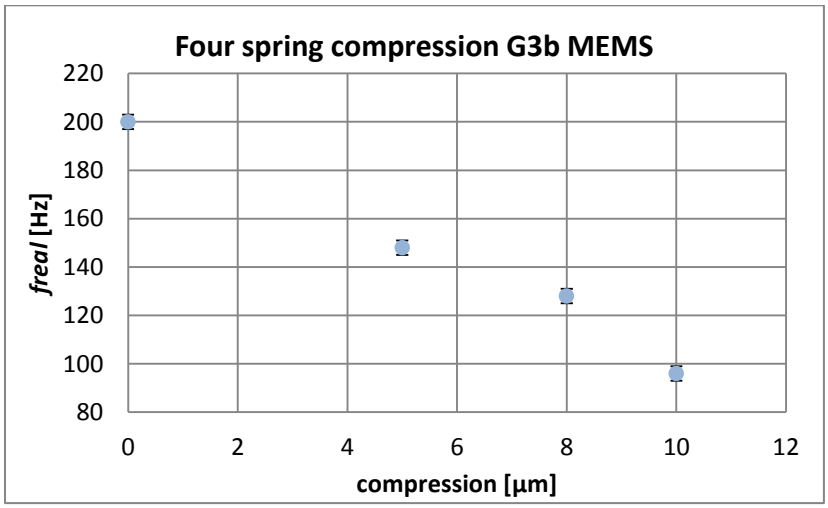

Figure 65: Four spring compression measurement. G3b MEMS.

The resonance frequency of this MEMS is measured to be $f_{real} = 200 \pm 2$ Hz. Maximum spring compression is limited to 10 µm, to avoid risking the ETA beams to melt.

In Figure 66 four spring compression measurement results are combined with extrapolation out of 2 spring compression measurements. Furthermore modeling results are shown.

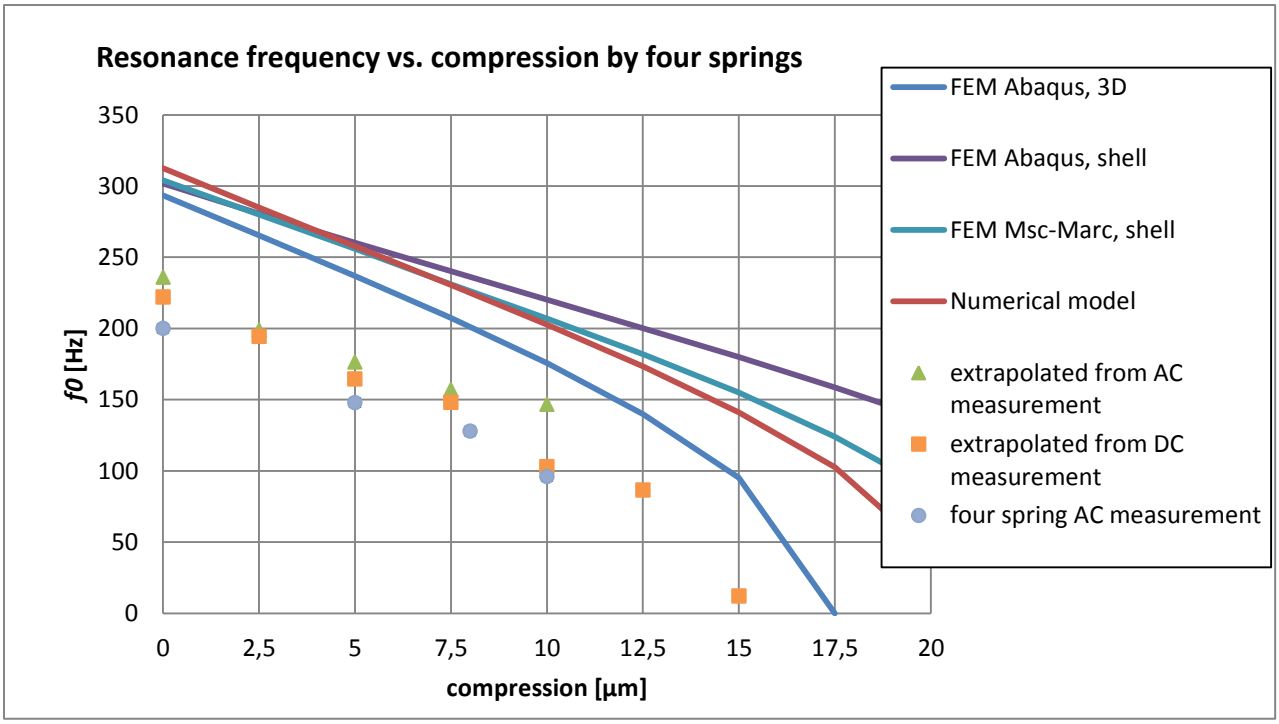

Figure 66: Figure 64 combined with Figure 65 four spring compression measurements.

The curves of extrapolated four spring compression and actual four spring compression measurements show correspondence in inclination. Applying 10 µm compression to all four springs, shows a factor 2,2 resonance frequency reduction for DC extrapolation and a factor 2,1 reduction for four spring measurement. DC extrapolation predicts that the resonance frequency can be reduced by a factor 17 for 15 µm compression. This implements that the resonance frequency can be reduced to a value in the order of 10^1 Hz for the G3b MEMS.

The difference in uncompressed resonance frequency for the two G3 MEMS can be explained by difference in device layer structures by etching errors and material defects.

4.4 Evacuation measurements

All MEMS evacuation measurements were done using the G2a MEMS. The relaxation time of the MEMS damped oscillator is measured versus pressure, shown in Figure 67.

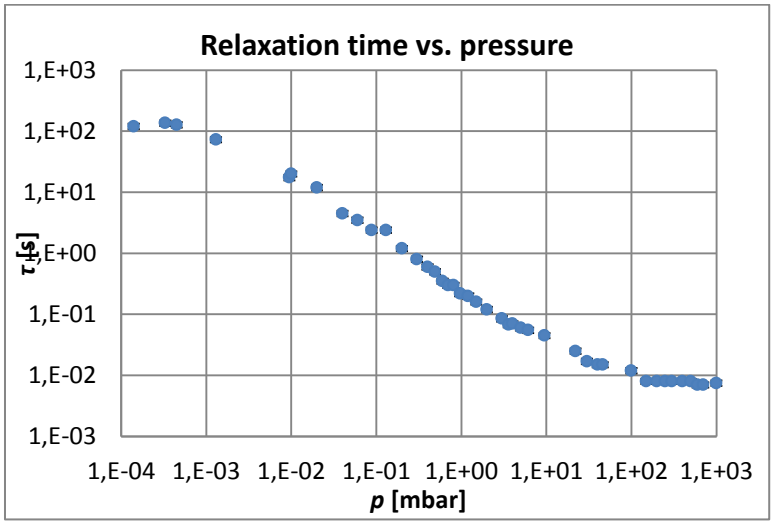

Figure 67: Measured relaxation time versus pressure.

The MEMS is evacuated to a pressure down to $p = 10^{-4}$ mbar.

The Q-value is calculated from the relaxation time using the following formula:

$$Q = \frac{\omega_0 \tau}{2}, \tag{49}$$

where:
$\omega_0 =$ Resonance frequency [Hz]
$\tau =$ Relaxation time [s].

Resulting in the Q-value versus pressure, shown in Figure 68.

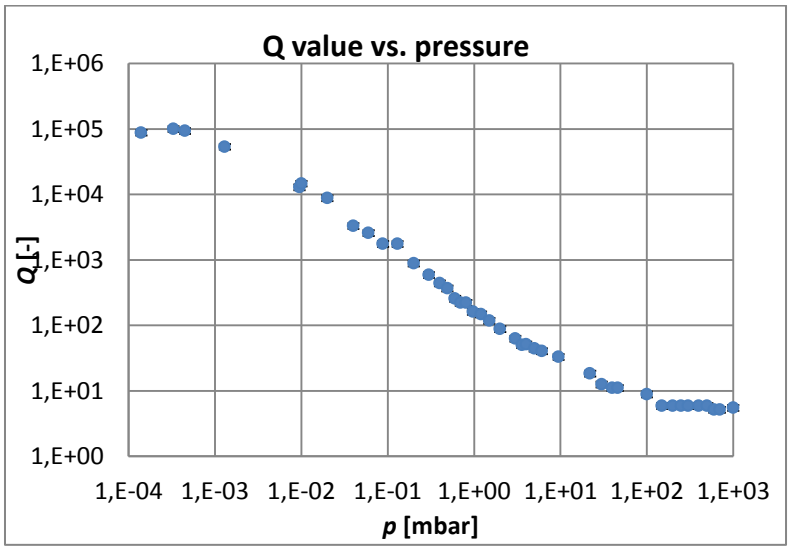

Figure 68: Q-value versus pressure, calculated out of relaxation time measurements.

At a pressure of around $p = 50\ \mathrm{mbar}$, the resonance quality factor starts rising, as predicted in section 3.6: at that pressure the air molecules mean free path approaches the mass-substrate gap size of 2 $\mu\mathrm{m}$. The air damping is expected to disappear when the mean free is exceeding the mass size (5 mm), at $p = 2 \cdot 10^{-2}\ \mathrm{mbar}$. However the air damping has disappeared around $p = 1 \cdot 10^{-3}\ \mathrm{mbar}$. This could be explained by the fact that the chip carrier is harder to evacuate than the rest of the vacuum chamber, because of the small gap between chip carrier top and glass plate.

The calculated Q-value from relaxation time measurement at atmospheric pressure is $Q = 5{,}5 \pm 0{,}5$, giving a corresponding damping factor $D = (1{,}4 \pm 0{,}2) \cdot 10^{-4}\ \mathrm{N/m/s}$, which corresponds to the modeled damping factor of $D = 1{,}15 \cdot 10^{-4}\ \mathrm{N/m/s}$, as treated in 2.6. The damping factor calculated in 4.1.1, with a value $D = (5{,}4 \pm 2) \cdot 10^{-4}\ \mathrm{N/m/s}$, is 4 times larger than expected. This can partly be ascribed to the large uncertainty of the measurement method used for this result, as shown in 4.1.1.

Figure 68 shows that in case of removed air damping the quality factor rises to a value of $Q = (1{,}0 \pm 0{,}1) \cdot 10^{5}$.

4.5 Further observations

4.5.1 G1 and G2 compression measurements

G2 MEMS spring compression is done for the G2a MEMS. The range of the ETA beams for the G2 design is found to be too small to push the bi-stable structure over its tipping point at 12 µm compression.

For the G1a MEMS the ETA beams were not able to move the spring structure. According to 3.1.1, Figure 38, at least a tip displacement of 20 µm is predicted for the G1 design. Comparing G1 to G2 shows that the G1 intermediate structure is much easier to compress. Because G2 compression is performed, it is concluded that the G1a intermediate structure is stuck to the substrate, possibly by etching errors or contamination of the MEMS, in the form of structure fragments between device layer and substrate.

4.5.2 IP measurements

The IP MEMS proof mass is designed to by initially rigid to the substrate by three connection points, as treated in 3.1.2. Then when the IP is set in vertical measurement position, connections can be melted by joule heating.

The connection beams on the side of the proof mass are accidentally designed to be 10 µm, which would mean these beams are too wide to be etched loose from the substrate. On the contrary of expectations, these beams were found to be loose in practice on the MEMS prepared for measurements, the proof mass being tilted against its stops. Apparently 10 µm wide structures are etchable or the remaining silicon oxide connection is shocked loose. The proof mass was found to be stuck, probably sticked to the substrate by gravity.

Remaining measurements possible is melting the connection points. A current is applied through the connection point above the proof mass. Joule heating causes longitudinal beam strain, curving the connection beam, as shown in Figure 69.

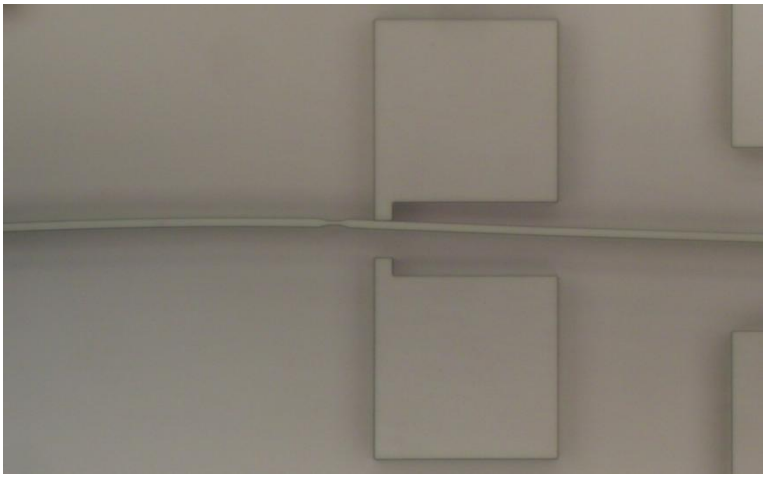

Figure 69: IP MEMS connection beam curvature.

5 Conclusions and suggestions

5.1 Conclusions

The lowest resonance frequency, by applying 10 µm four spring compression, is measured $f_0 = 96 \pm 2$ Hz, for a MEMS accelerometer with an uncompressed resonance frequency of $f_0 = 200 \pm 2$ Hz. It is predicted that for further compression to 15 µm, the resonance frequency will further reduce to a value in the order of 10^1 Hz.

Compressions of more than 10 µm is restricted by the range of the ETA beams, which are likely to melt when actuated further. Compression of $10{,}0 \pm 0{,}5$ µm of the G3 single guiding spring intermediate structure is measured for a current $I = 13{,}45 \pm 0{,}1$ mA applied through the beam, corresponding with modeling. The G1 anti-reverse structure is modeled to be compressed over the same distance by roughly a factor 2 lower force and the G2 bi-stable structure needs a factor 4,5 more force. Because of the stiff G2 intermediate structure, the ETA beams aren't able to push the bi-stable beam over its tipping point at 12 µm compression.

A calibration constant $c_A = \frac{F}{U_A^2} = (2{,}0 \pm 0{,}1)\ \mathrm{N/V^2}$ is calculated from measurements for the actuator combs. The ratio of voltage needed for a certain displacement, in static and resonance situation, results in a quality factor $Q = 1{,}5 \pm 0{,}7$ calculated from measurements. This implies a damping factor $D = (5{,}4 \pm 2) \cdot 10^{-4}\ \mathrm{N/m/s}$ for the oscillator. This result has large uncertainty and is considered unreliable. Measurement of the relaxation time results in a more precise $Q = 5{,}5 \pm 0{,}5$ and a corresponding $D = (1{,}4 \pm 0{,}2) \cdot 10^{-4}\ \mathrm{N/m/s}$, which is in agreement with damping modeling. Removing air damping effects by evacuation of the MEMS to a pressure of $p = 1 \cdot 10^{-3}$ mbar, results in a much higher quality factor of $Q = (1{,}0 \pm 0{,}1) \cdot 10^5$.

5.2 Suggestions and outlook

For a future improved MEMS design, it is most necessary to increase ETA beam actuation range. This means increase of the maximum force that can be applied to compress the intermediate structure. For increase of the ETA beam range, the optimal geometry has to be modeled, considering heat transfer and resulting beam stress and strain. More ETA beam range would mean larger compression possibilities, preferably up to 20 μm for G1 and G3 designs. The G2 bi-stable beam structure is a factor 2 stiffer and is preferably compressed up to the tipping point at 12 μm.

Using the current MEMS design, the ETA beams could be actuated up to the melting limit for G1 and G2 structure compression, verifying the displacement modeling done for these structures.

The distance measurement resolution through microscope could be improved by raising the MEMS chip in its carrier, reducing the distance between glass top and device layer to a maximum value of 0,6 mm (which is the working distance of the 50x objective). Also a distance gauge could be etched on the comb anchors, with for example micron deviation, improving the uncertainty by a factor 5. This micron deviation gauge will for example make it possible to calibrate the sensing combs for displacement versus voltage.

Practical improvements of the MEMS design include etching a distance gauge on the comb anchors, improving distance measurement resolution through microscope. of the MEMS type name on the structure for better distinction, especially for the bonding executer. Furthermore storage of the MEMS chips has to be improved, lessening defects by contamination.

Future measurements should include feedback of the sensing signal for displacement compensating actuation. The feedback system could then be measured on an acceleration table. Also noise has to be characterized, for improving the signal to noise ratio of the accelerometer. Finally an improved MEMS design has to be developed, primarily aiming on larger ETA beam range and less device layer defects, blocking proof mass displacement.

6 References

[1] EGO - European Gravitational Observatory, *The Virgo detector*, http://www.ego-gw.it/virgodescription/pag_4.html

[2] Aspera – Applied solutions, *Virgo*, http://www.aspera-eu.org/images/stories/Media/MEDIAPICTURES/HR/virgo.jpg

[3] Maloney, J.M., DeVoe, D.L., Schreiber, D.S., *Analysis and design of electrothermal actuators fabricated from single crystal silicon*, University of Maryland, College Park, (2000)

[4] Enikov, E.T., Kedar, S.S., Lazarov, K.V., *Analytical and experimental analysis of folded beam and V-shaped thermal microactuators*, University of Arizona, (200X)

[5] Hermann, A., Design and characterization of a high-sensitivity bulk-micromachined in-plane accelerometer, University of Twente, Department of Electrical Engineering, (2005)

[6] Lammerink, *Micro-Electro-Mechanical-Systems - Design Laboratory – Process-Document* v2.0, University of Twente, TST - Transducers science and technology group, (2011-2012)

[7] Kyocera C-QFJ chip carrier technical data sheet. http://global.kyocera.com/prdct/semicon/semi/std_pkg/pdf/kyocera-pkg-cqfj-e.pdf

[8] Mech-EL Industries, *Mech-EL/MEI 907*, http://mech-el.com/907.htm

[9] EO Edmund optics, *Zeiss EC Epiplan Neofluar Brightfield/Darkfield Objectives,* http://www.edmundoptics.com/microscopy/infinity-corrected-objectives/zeiss-ec-epiplan-neofluar-brightfield-darkfield-objectives/2814

[10] University of Camebridge DoITPoMS, *Bending and Torsion of Beams*, http://www.doitpoms.ac.uk/tlplib/beam_bending/printall.php

[11] Efunda, *Thermal Conductivity: Silicon*, http://www.efunda.com/materials/elements/TC_Table.cfm?Element_ID=Si

[12] Incropera, Frank P., de Witt, David P. (1990). *Introduction to heat transfer*, (2nd edition). School of Mechanical Engineering, Purdue University. Canada: John Wiley & Sons.

[13] Electronics Cooling, *The Thermal Conductivity of Air at Reduced Pressures and Length Scales*, http://www.electronics-cooling.com/2002/11/the-thermal-conductivity-of-air-at-reduced-pressures-and-length-scales/

7 Appendices

7.1 Modeling parameters

Table 4: modeling parameters

General	Proof mass	m	0,511	mg
	Gap device layer - substrate	g	2	µm
	Height device layer	h	25	
	Ambient temperature	$T\infty$	293	K
Silicon	Thermal conductivity ($T = T_\infty$)	k_{Si}	149	W/mK
	Young's modulus	E	150	GPa
	Mass density ($T = T_\infty$)	ρ_{Si}	2330	kg/m^3
	CTE (average 300 -1500K)	α	3,92E-06	K^{-1}
Air	Thermal conductivity ($T = T_\infty$)	k_{air}	0,023	W/mK
	Dynamic viscosity ($p = p_0$)	μ_{air}	1,85E-05	kg/ms
	permittivity	ε_0	8,8e-12	F/m
Spring	Length	L_{spring}	1000	µm
	Radius of curvature	R	1000	
	thickness	t_{spring}	5	
V-beam	Length	L_V	1462	
	Actual width	w_v	18	
	Effective width (from FEM)	w_v*	14	
Actuation comb	distance between actuation fingers	d_A	10	
	Actuation comb finger overlap	L_A	*40*	
	Actuation comb capacitance correction factor (from FEM simulation)	C_c	0,8	[-]
Sensing comb	Small distance between sensing fingers	d_s	10	µm
	Large distance between sensing fingers	d_{sbig}	30	
	Sensing comb finger overlap	L_S	*240*	

7.2 Forced harmonic motion equation derivation

Consider a proof mass *m* attached to a frame by a spring with spring constant k. The proof mass can be accelerated relative to the frame by applying a force *F* on the proof mass, or by a displacement x_0 of the frame, see Figure 3. The relative displacement is given by $y = x_1 - x_0$, where x_1 is the displacement of the proof mass.

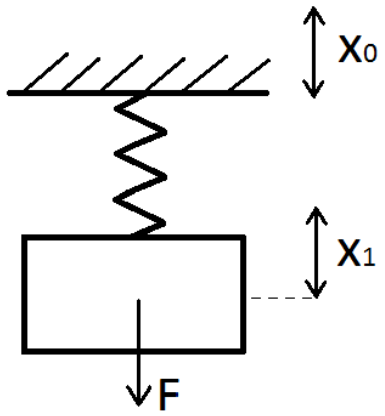

Figure 3: Sketch of a mass-spring system.

According to Newton's second law of motion:

$$ma = \Sigma \mathrm{F} \tag{50}$$

The sum of forces is build up out of the spring force by Hooke's law ($F_{spring} = kx$), the damping force ($F_{damping} = Dv$) and the external applied force F, giving:

$$m\frac{d^2x_1}{dt^2} = -k(x_1 - x_0) - D\frac{d(x_1 - x_0)}{dt} + F\,.$$

Rearranging gives the well-known equation of damped harmonic motion:

$$m\frac{d^2x_1}{dt^2} + D\frac{d(x_1 - x_0)}{dt} + k(x_1 - x_0) = F\,, \tag{51}$$

where:
$x_0 = \text{displacement of frame [m]}$
$x_1 = \text{displacement of mass [m]}$
$D = \text{damping factor [N/(m/s)]}$
$k = \text{spring constant [N/m]}$

By solving this second order differential equation for harmonic motion $x = \hat{x}e^{i\omega t}$ and harmonic force $F = F_0 e^{i(\omega t - i\varphi)} = \hat{F}e^{i\omega t}$, the following solution follows:

$$-m\omega^2\hat{x}_1 e^{i\omega t} + i\omega D e^{i\omega t}(\hat{x}_1 - \hat{x}_0) + k(\hat{x}_1 - \hat{x}_0)e^{i\omega t} = \hat{F}e^{i\omega t}\,, \tag{52}$$

where the harmonic displacement x_1 is given by:

$$x_1 = |x_1|e^{i(\omega t - i\varphi)} = |x_1|e^{-i\varphi} + e^{i\omega t} = \hat{x}_1 e^{i\omega t} ,$$

where:
$\hat{x}_1 =$ complex amplitude of mass oscillation [m] ,
$\hat{x}_0 =$ complex amplitude of anchor oscillation [m]
$\hat{F}_0 =$ complex force amplitude [N] ,

analogous for x_0. Where φ is the angle by which the displacement lags behind the applied excitation or force.

In Eq. (52), canceling the common factor $e^{i\omega t}$, dividing by m, and substituting $\frac{k}{m} = \omega_0^2$, according to Eq. (2), gives:

$$-\omega^2 \hat{x}_1 + i\omega \frac{D}{m}(\hat{x}_1 - \hat{x}_0) + \omega_0^2(\hat{x}_1 - \hat{x}_0) = \frac{\hat{F}_0}{m} \tag{53}$$

Bringing $\hat{x}_1$ and $\hat{x}_0$ outside gives:

$$\hat{x}_1 \left(-\omega^2 + i\omega \frac{D}{m} + \omega_0^2\right) = \hat{x}_0 \left(i\omega \frac{D}{m} + \omega_0^2\right) + \frac{\hat{F}_0}{m}, \tag{54}$$

When the proof mass is accelerated by frame displacement, and $\hat{F}_0 = 0$, gives:

$$\frac{\hat{x}_1}{\hat{x}_0} = \frac{i\omega \frac{D}{m} + \omega_0^2}{(\omega_0^2 - \omega^2) + i\left(\frac{D}{m}\omega\right)}, \tag{55}$$

and when the proof mass is accelerated by a force applied:

$$\frac{\hat{x}_1}{\hat{F}} = \frac{\frac{1}{m}}{(\omega_0^2 - \omega^2) + i\left(\frac{D}{m}\omega\right)}. \tag{56}$$

The ratio of $\hat{y}$ and $\hat{x}_0$ is given by:

$$\frac{\hat{y}}{\hat{x}_0} = \frac{\hat{x}_1 - \hat{x}_0}{\hat{x}_0} = \frac{i\omega \frac{D}{m} + \omega_0^2 - (\omega_0^2 - \omega^2) - i\left(\frac{D}{m}\omega\right)}{(\omega_0^2 - \omega^2) + i\left(\frac{D}{m}\omega\right)} = \frac{\omega^2}{(\omega_0^2 - \omega^2) + i\left(\frac{D}{m}\omega\right)} . \tag{57}$$

And for the ratio of $\hat{y}$ and $\hat{F}$ (in which case $\hat{x}_0 = 0$):

$$\frac{\hat{y}}{\hat{F}} = \frac{\hat{x}_1}{\hat{F}} = \frac{\frac{1}{m}}{(\omega_0^2 - \omega^2) + i\left(\frac{D}{m}\omega\right)} . \tag{58}$$

Absolute values are, including substitution of $D = 2\gamma m$:

$$\left|\frac{\hat{y}}{\hat{x}_0}\right| = \frac{\omega^2}{\omega_0^2}\frac{1}{\sqrt{\left(1-\frac{\omega^2}{\omega_0^2}\right)^2+\left(2\gamma\frac{\omega}{\omega_0}\right)^2}}\,, \tag{59}$$

and:

$$\left|\frac{\hat{y}}{\hat{F}}\right| = \frac{1}{k}\frac{1}{\sqrt{\left(1-\frac{\omega^2}{\omega_0^2}\right)^2+\left(2\gamma\frac{\omega}{\omega_0}\right)^2}}\,. \tag{60}$$

The phase angle φ is derived from Eq. (52) as follows:

$$-m\omega^2\hat{x}_1 + i\omega D\hat{x}_1 + k\hat{x}_1 - i\omega D\hat{x}_0 - k\hat{x}_0 = \hat{F}_0 = F_0\cos\varphi + iF_0\sin\varphi, \tag{61}$$

Where the real and imaginary part are:

$$-m\omega^2\hat{x}_1 + k(\hat{x}_1 - \hat{x}_0) = F_0\cos\varphi \quad \text{and} \quad \omega D(\hat{x}_1 - \hat{x}_0) = F_0\sin\varphi\,, \tag{62}$$

Giving (by dividing Eqs.(62)):

$$\varphi = \tan^{-1}\frac{\frac{D}{m}\omega(\hat{x}_1 - \hat{x}_0)}{\omega_0^2(\hat{x}_1 - \hat{x}_0) - \omega^2\hat{x}_1}, \tag{63}$$

7.3 Anti-spring principle derivation

The principle of an anti-spring is shown in Figure 5 below.

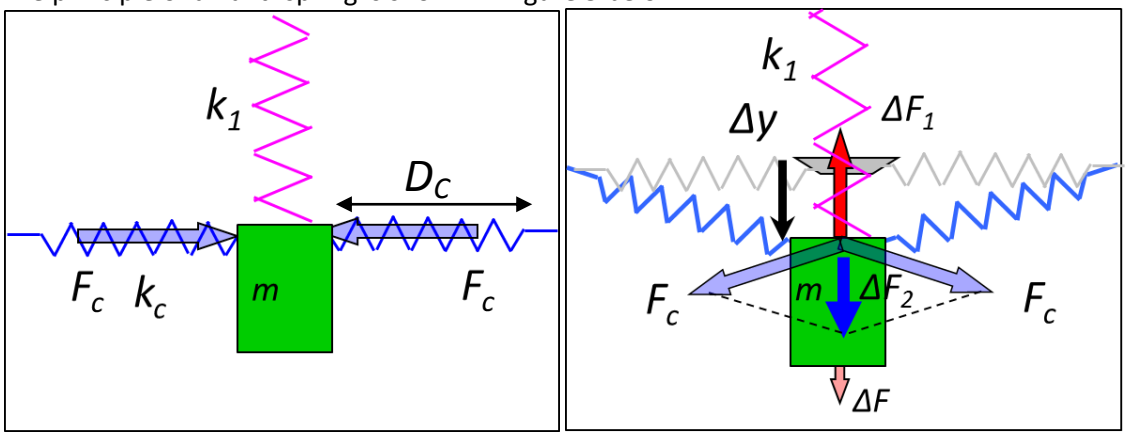

Figure 5: a) Initial state: mass-spring system with spring constant k_1, located between two compression springs with spring constant k_c and compression force F_c each. b) Displaced stage: For a displacement Δy off the proof mass, the upward vertical spring force ΔF_1 is compensated by a downward counteract force ΔF_2, formed by the vertical components of the compression forces F_c. The resulting force ΔF is left, thus the spring constant k_1 in vertical direction is lowered.

In Figure 5a equilibrium of forces is given by:

$$\begin{aligned} \Sigma F = \vec{F}_z + \vec{F}_{spring} + \vec{F}_{c1} + \vec{F}_{c2} = \\ (mg - k_1 y)\sin\left(\frac{1}{2}\pi\right) + (F_{c1} - F_{c2})\sin(0) = \\ mg - k_1 y = 0\,, \end{aligned} \tag{64}$$

where:
$F_z =$ gravitational force [N]
$F_{spring} =$ spring foce [N]
$F_C =$ compression force [N]
$m =$ mass [kg]
$k =$ spring constant [N/m] ,

and $F_{c1} = F_{c2} = F_c$. In Figure 5b the mass is displaced over a distance Δy. The vertical component of the compression forces F_c is given by:

$$\Delta F_2 = 2F_c \sin\theta\,, \tag{65}$$

where:
$\Delta F_2 =$ vertical component of the compression forces [N] ,

which for small values of Δy is:

$$\Delta F_2 = 2\theta F_c \quad \text{and} \quad \theta \approx \frac{\Delta y}{D_c}. \tag{66}$$

The sum of forces is given by:

$$F_{tot} = \Delta F_1 + \Delta F_2 = -k_1 \Delta y + 2\frac{F_c}{D_c}\Delta y = -\left(k_1 - 2\frac{F_c}{D_c}\right)\Delta y\,, \tag{67}$$

resulting in:

$$k_{tot} = k_1 - 2\frac{F_c}{D_c}. \tag{68}$$

7.4 Bending beam modeling

Bending of a beam, results in a curved beam with radius R. The longitudinal beam axis which stays the same length during bending deformation is called the neutral axis L_0 of the beam. All axis $+y$ have positive strain during deformation and all axis $-y$ have negative strain, see Figure 70.

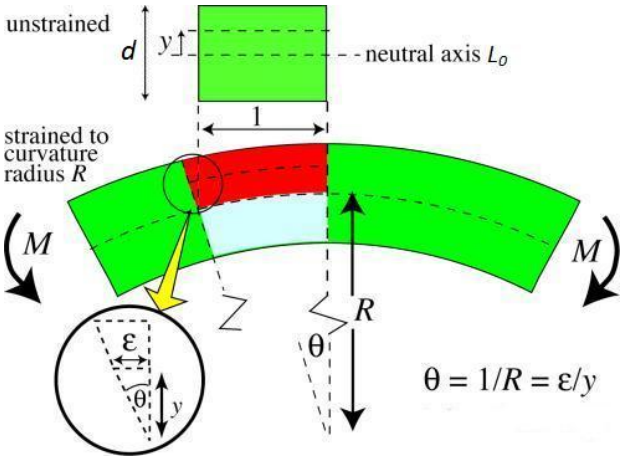

Figure 70: Beam bending modeling sketch. [10]

The axis length at a longitudinal distance y from the neutral axis is a linear relation given by:

$$L(y) = L_0 + \alpha y\,, \tag{69}$$

where:
$L_0 =$ neutral axis [m]
$L(y) =$ beam length at a distance y, perpendicular to the neutral axis [m]
$\alpha =$ linear factor $[-]$.

By definition for the arc length of the circle with radius R:

$$L_0 = R\varphi\,, \tag{70}$$

where:
$R =$ radius of beam curvature [m]
$\varphi =$ beam curvature angle [rad] .

By definition for the arc length of the circle with radius $R + y$:

$$L(y) = (R + y)\varphi = (R + y)\frac{L_0}{R} = L_0\left(1 + \frac{y}{R}\right). \tag{71}$$

The beam strain at a distance y from the neutral axis is defined as $\varepsilon = \frac{\Delta L}{L}$, and can be rewritten, using Eq. (71), into:

$$\varepsilon(y) = \frac{\Delta L}{L} = \frac{L(y) - L_0}{L_0} = \frac{y}{R}\,. \tag{72}$$

The stress is related to the strain by Hooke's law:

$$\sigma(y) = E\varepsilon(y) = \frac{Ey}{R}, \tag{73}$$

where:
$\sigma(y) =$ beam stress at a distance y, perpendicular to the neutral axis [m]
$E =$ Young's modulus [Pa] .

The stress in the beam can be described as force vectors, gaining in value for a larger distance y from the neutral axis, see Figure 70b:

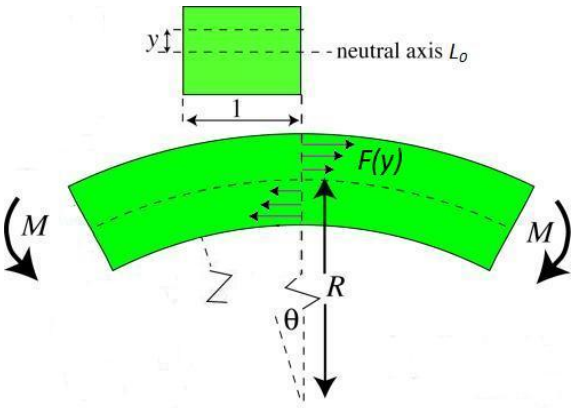

Figure 70b: Bending beam situation sketch, force $F(y)$ causing beam stress.

The vector component dF is defined as the stress working on an area dA:

$$dF = \sigma dA = b\sigma dy\,, \tag{74}$$

where:
$dF =$ force component [N]
$dA = area\ [m^2]$
$b =$ beam width [m]
$dy =$ beam height [m] .

Applying Eq. (74) in the definition of moment results in:

$$M = \int_{-y/2}^{+y/2} dF \cdot y = 2\int_{-y/2}^{+y/2} b\sigma \cdot y dy = \frac{2bE}{R}\int_0^{d/2} y^2 dy = \frac{Ebd^3}{12R}, \tag{75}$$

where:
$d =$ beam height [m] .

The definition of the second moment of area gives, in case of the beam:

$$I_{beam} = \int_{Area} y^2 dA = \int_{-\frac{d}{2}}^{\frac{d}{2}} y^2 b dy = \frac{bd^3}{12}, \tag{76}$$

where:
$I_{beam} = second\ moment\ of\ area\ of\ the\ beam\ [m^4]$.

This gives for the moment on the beam:

$$M = \frac{EI_{beam}}{R}. \tag{77}$$

7.5 Derivation of analytical model for temperature profile of an ETA beam

The differential equation given by Maloney [2] can be solved analytically:

$$k_s \frac{d^2T(x)}{dx^2} + J^2\rho - Sk_a \frac{T(x) - T_\infty}{gh} = 0\,, \tag{78}$$

Dividing by k_s and substitution of $m^2 = \frac{Sk_a}{k_s gh}$ gives:

$$T(x) = T_\infty + \frac{J^2\rho}{k_s m^2} + c_1 e^{mx} + c_2 e^{-mx} \tag{79}$$

The constants c_1 and c_2 can be found by inserting the boundary conditions of both beam ends (at $x = 0$ and $x = L$). The beam ends have ambient temperature, so a heat flow will occur to the beam ends.:

$$T(0) = T_\infty \quad \rightarrow \quad -\frac{J^2\rho}{k_s m^2} = c_1 + c_2 \tag{80}$$

$$T(L) = T_\infty \quad \rightarrow \quad -\frac{J^2\rho}{k_s m^2} = c_1 e^{mL} + c_2 e^{-mL} \tag{81}$$

Subtracting Eq. (80) minus Eq. (81) gives:

$$c_1 = \frac{J^2\rho}{k_s m^2} \frac{1 - e^{-mL}}{e^{-mL} - e^{mL}}$$

$$c_2 = \frac{J^2\rho}{k_s m^2} \frac{1 - e^{mL}}{e^{mL} - e^{-mL}}\,,$$

which results in:

$$T(x) = T_\infty + \frac{J^2\rho}{k_s m^2}\left(1 + \frac{1 - e^{-mL}}{e^{-mL} - e^{mL}} e^{mx} + \frac{1 - e^{mL}}{e^{mL} - e^{-mL}} e^{-mx}\right), \tag{82}$$

where (as mentioned earlier):

$$m^2 = \frac{Sk_a}{k_s gh}$$

7.6 Derivation of the thermo-mechanical model

Joule heating of a lightly V-shaped beam between two rigid walls, builds up virtual strain in the beam and consequently a the beams apex is pushed outwards. Because of symmetry one beam half can be modeled, replacing the other half by a moment M_0 (See Figure 17). Considered must be bending strain, stretching strain and thermal strain. The strain by bending of a beam is derived as follows:

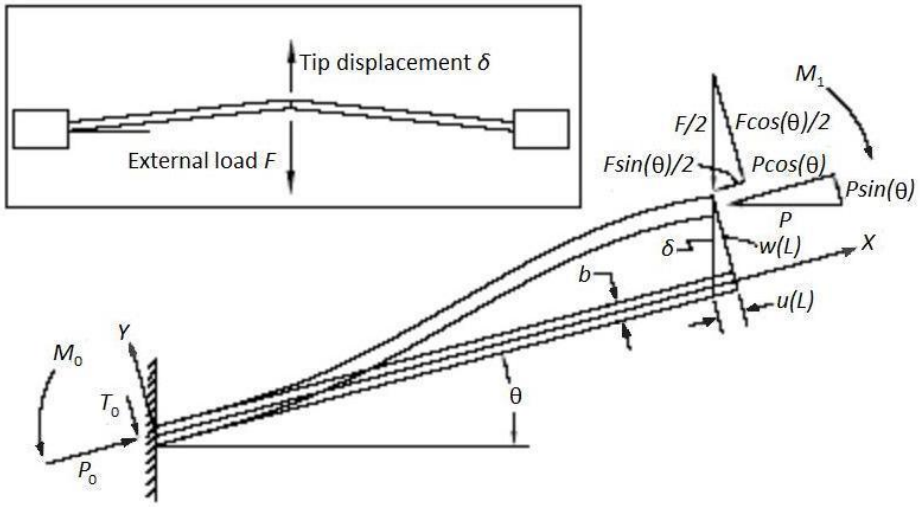

Figure 17: ETA beam, shape deformation and loads. [3]

- **Bending strain**

$$dl = Rd\theta$$

$$\frac{1}{R} = \frac{d\theta}{dl} \tag{83}$$

Because $dl \approx dx$:

$$\frac{1}{R} = \frac{d\theta}{dx} = \theta'$$

And because $\theta \approx \tan\theta$:

$$\theta = w'$$

Results in:

$$\frac{1}{R} = w'' \tag{84}$$

By using the definition of strain, the bending strain is found:

$$\varepsilon = \frac{d\theta(R_0 + y) - d\theta R_0}{d\theta R_0} = \frac{y}{R_0} = yw'' \tag{85}$$

- **Stretching strain**

Stretching of a beam in its longitudinal direction, is described by a length, dx, of the initial beam increasing into a length, dl, of the stretched beam. During the deformation, point x shifts to point $u(x)$ and point $x + dx$ to $u(x + dx)$. In the y-direction an analogous shift takes place, into $w(x)$ and $w(x + dx)$. The following holds for a stretched length dl of the beam:

$$dl = \sqrt{[dx + u(x + dx) - u(x)]^2 + [w(x + dx) - w(x)]^2}\,, \tag{86}$$

where:
$dl = length\ difference\ of\ the\ beam\ in\ longitudinal\ direction\ [m]$
$x = point\ on\ X - axis\ (along\ the\ initial\ beam)[m]$
$u(x) = longitudal\ displacement\ of\ the\ beam\ [m]$
$w(x) = transverse\ displacement\ of\ the\ beam\ [m]$.

The strain in the longitudinal direction of the beam is described as:

$$\varepsilon_x^0 = \frac{dl - dx}{dx} = \frac{dl}{dx} - 1$$

$$= \sqrt{\left[\frac{dx + u(x + dx) - u(x)}{dx}\right]^2 + \left[\frac{w(x + dx) - w(x)}{dx}\right]^2} - 1 = \sqrt{(1 + u')^2 + w'^2} - 1\,, \tag{87}$$

where:
$\varepsilon_x^0 = Longitudinal\ strain\ [-]$.

A first order Taylor series ($\sqrt{1 + x} \approx 1 + \frac{1}{2}x$) can be applied for approximation because: $u', w' \ll 1$, resulting in:

$$\varepsilon_x^0 = 1 + \frac{1}{2}\left[2u' + u'^2 + w'^2\right] - 1 = u' + \frac{1}{2}\left[u'^2 + w'^2\right] \tag{88}$$

Combining stretching and bending results in the total strain due to deformation:

$$\varepsilon_x = \varepsilon_x^0 - \varepsilon = u' + \frac{1}{2}\left[u'^2 + w'^2\right] - yw''\,, \tag{89}$$

where:
$e_x = Total\ strain\ [-]$.

- **Thermal strain**

The virtual thermal strain of the beam is given by:

$$\varepsilon_T = \alpha \Delta T\,, \tag{90}$$

where:
$\Delta T = \text{temperature rise [K]}$

$\varepsilon_T = \text{thermal strain } [-]$

The beam fixed point exerts a counter force P_0, countering the stress force created by the total virtual strain.

$$P_0 = \varepsilon EA\,, \tag{91}$$

Gives the total strain equation:

$$\varepsilon_x^0 - \alpha\Delta T = -\frac{P_0}{EA} \tag{92}$$

Furthermore the total moment equation is found by summing all beam moments, see Figure 17. The sum of moment consists of a force P_0 with its transversal arm, T_0 with its longitudinal arm, M_0 the moment on the beam fixed end and EIw'' the moment by beam bending:

$$EIw'' + P_0 w = -T_0 x - M_0\,, \tag{93}$$

where:
$P_0 = \text{Longitudinal force on beam fixed end [N]}$
$T_0 = \text{Tranversal force on beam fixed end [N]}$
$M_0 = \text{Moment on beam fixed end [Nm]}$

The set of differential equations, Eqs. (24) and(93), is solved for $w(x)$, resulting in:

$$w(x) = \left(\tan\theta - \frac{F}{2k^2 EI\cos\theta}\right)\left(\frac{\sin kx}{k} + \frac{(\cos kL - 1)(\cos kx - 1)}{k\sin kL} - x\right), \tag{94}$$

where $k = \sqrt{\frac{P_0}{EI}}$ is found by solving a transcendental equation $c(k, F, \bar{T})$:

$$\begin{aligned} c(k,F,\bar{T}) = \frac{k^2 IL}{A} - \alpha\bar{T}L + \frac{1}{2}\left(\tan\theta - \frac{F}{2k^2 EI\cos\theta}\right)^2\left(L + \frac{kL - 3\sin kL}{k(\cos kL + 1)}\right) \\ + \tan\theta\left(\frac{2}{k}\tan\left(\frac{kL}{2}\right) - L\right)\left(\tan\theta - \frac{F}{2k^2 EI\cos\theta}\right) = 0 \end{aligned} \tag{95}$$

This equation contains the externally applied force F, countering the beams actuation direction, and the average beam temperature by joule heating $\bar{T}$. The average beam temperature is given by:

$$\bar{T} = \frac{1}{L}\int_0^L (T(x) - T_\infty)\,dx \tag{96}$$

Solving k gives the tip displacement of the beam:

$$\delta = \frac{w(L)}{\cos\theta} = \left(\frac{2k^2 EI\sin\theta - F}{2k^2 EI(\cos\theta)^2}\right)\left(\frac{2\tan\frac{kL}{2} - kL}{k}\right) \tag{97}$$

This displacement is the total transversal beam tip displacement, corrected

7.7 Temperature and pressure dependencies, ETA beam related

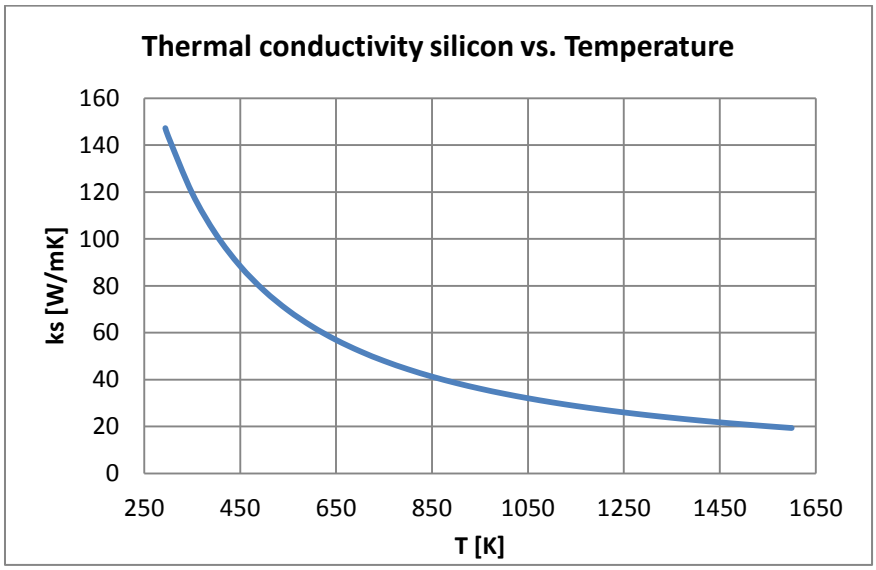

Figure 71: Temperature dependency thermal conductivity silicon. [11]

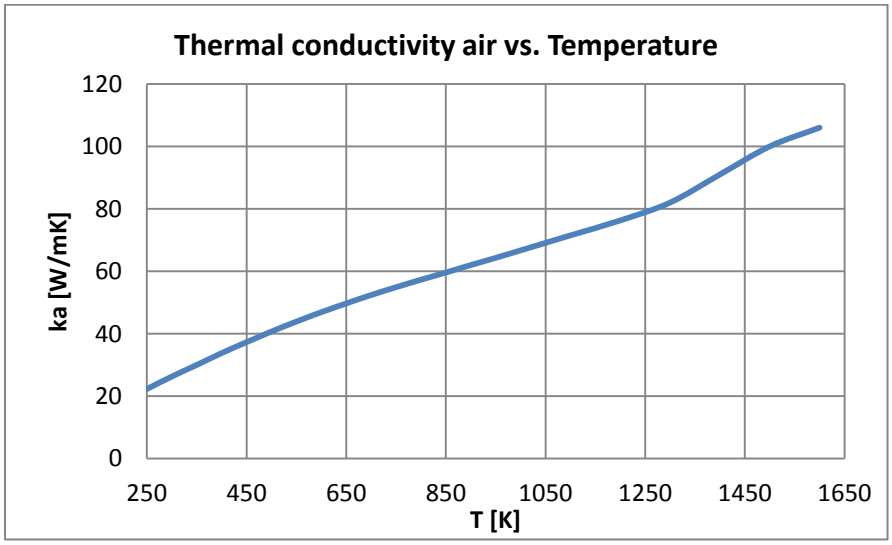

Figure 72: Temperature dependency thermal conductivity air. [12]

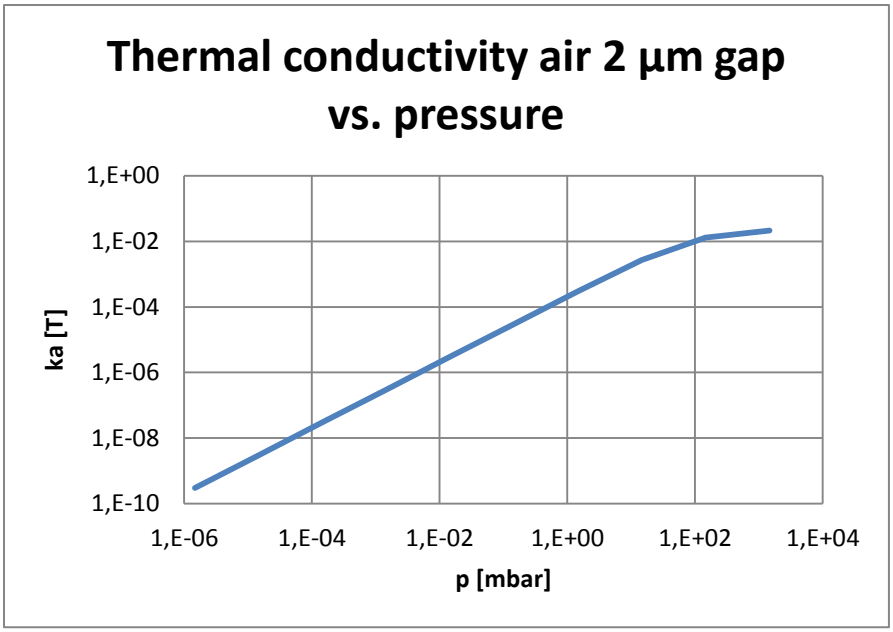

Figure 73: Pressure dependency thermal conductivity air. [13]

7.8 Wire bonding lay-outs

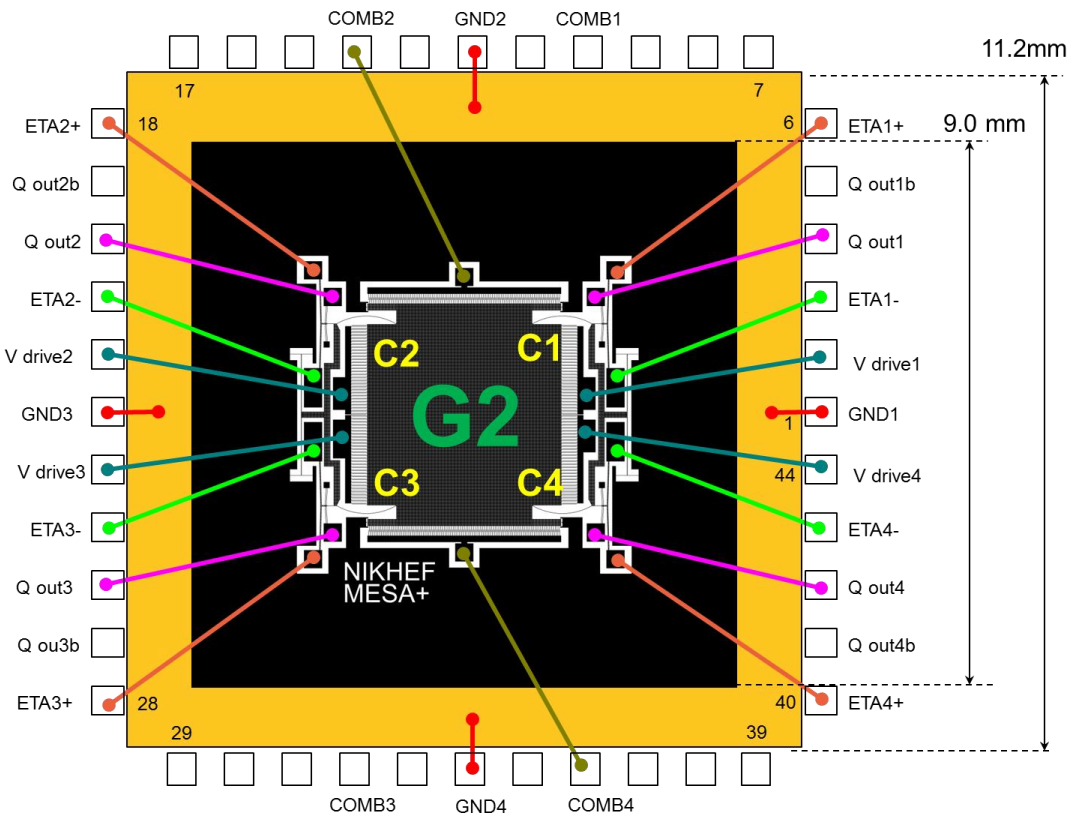

Figure 74: wire bonding lay-out for the G2 MEMS design.

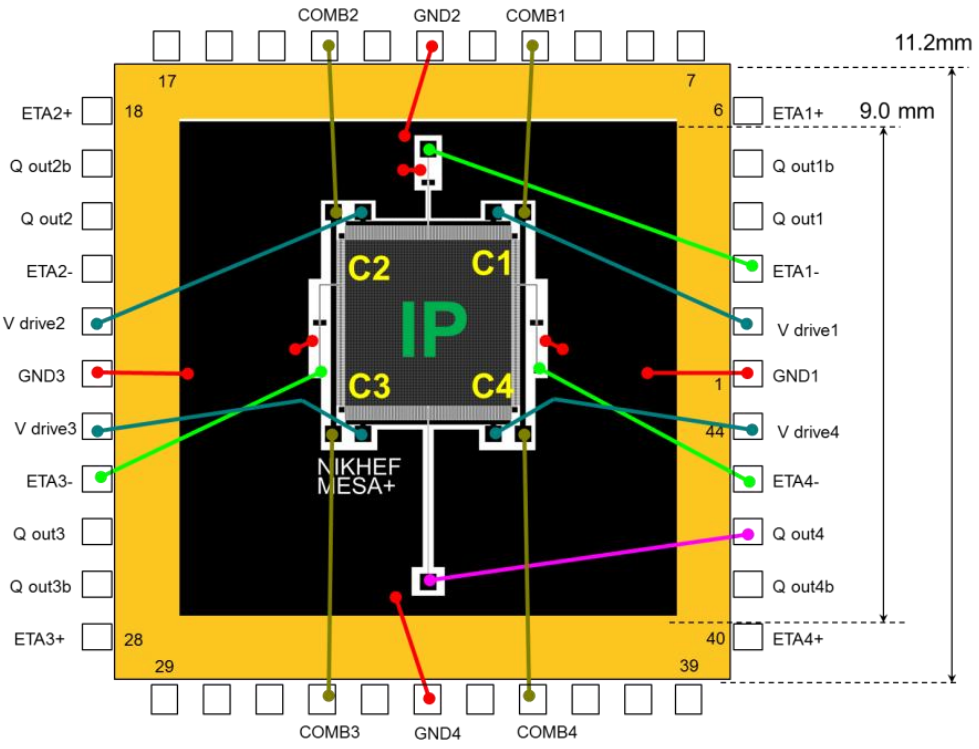

Figure 75: wire bonding lay-out for the IP MEMS design.

7.9 Additional pictures

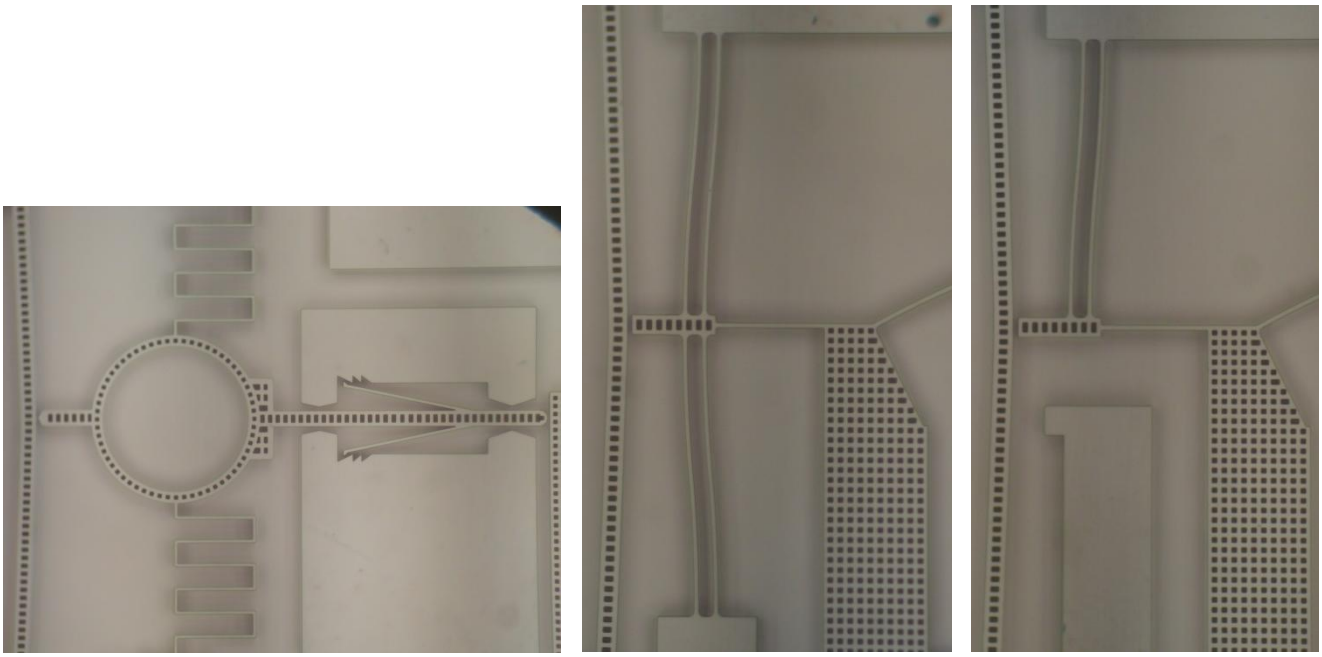

Figure 76: From left to right, G1 anti-reverse, G2 bi-stable, G3 single guiding. 200x magnification microscope.

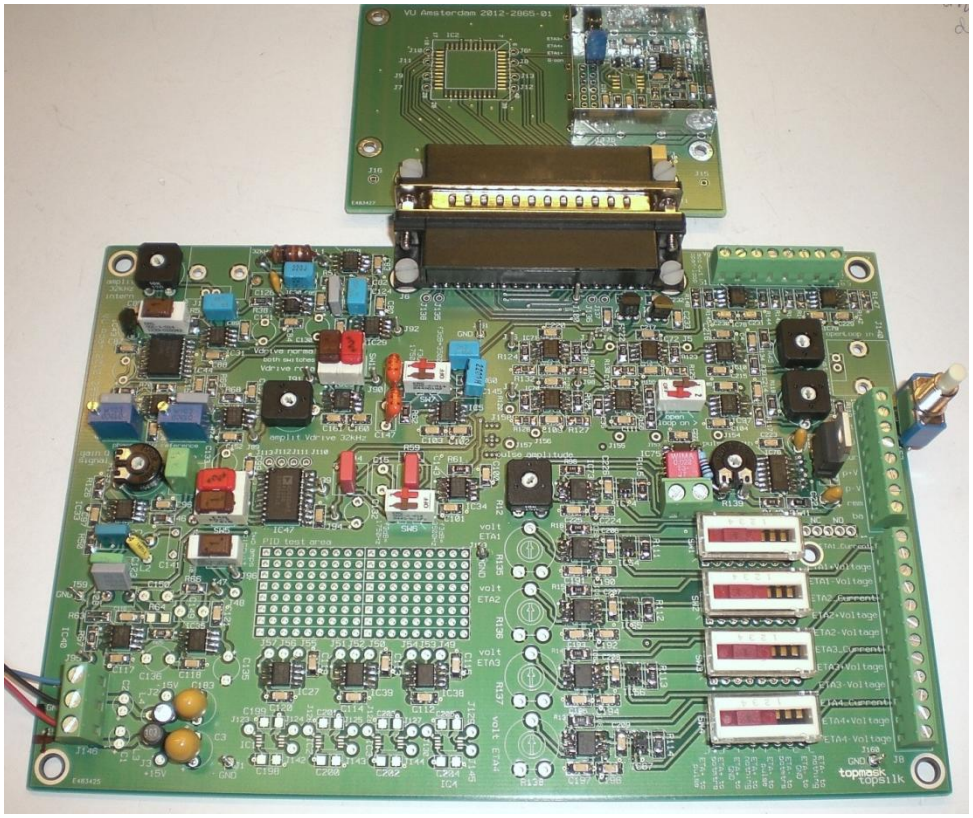

Figure 77: Electronics chip board. Top: in-vacuum board. Bottom: main out-vacuum board.

Figure 78: In-vacuum electronics chip board with soldered chip carrier.

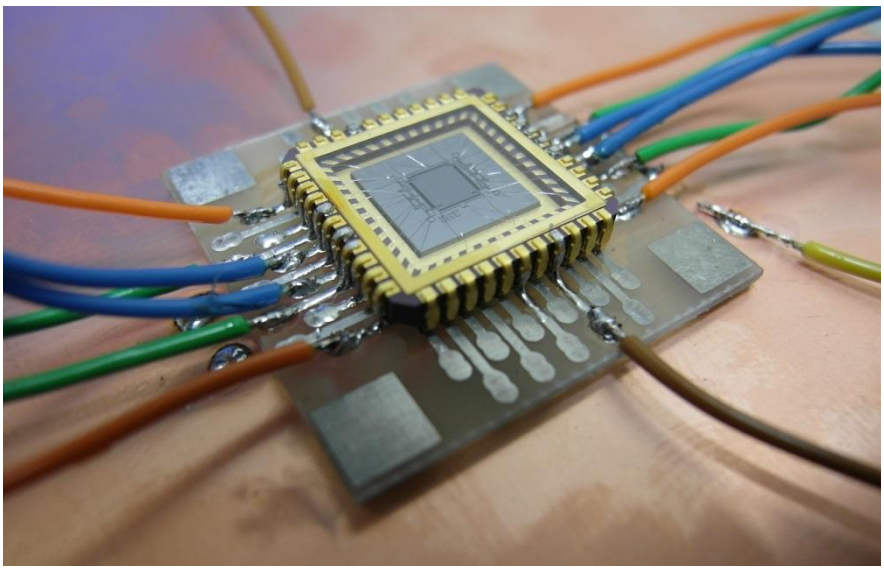

Figure 79: wire soldering on bread board as measurement method before the electronic chip board was finished.

7.10 Acknowledgements

With thanks to:

- Richard Rosing: FEM modeling support and book resources
- Allesandro Bertolini: vacuum set-up and electronics
- Joop Rövekamp: MEMS bonding
- Han Voet: electronics (VU University)
- Paul Timmer: soldering support
- Wim Gotink: electronics
- Berend Munneke: vacuum set-up
- Rogier Elsinga: design and build of vacuum chamber (VU University)

With special thanks to:

- Eric Hennes: internship supervisor